THE UNIVERSITY *of* EDINBURGH

Numerical modelling of sediment transport, bed morphology, and porous obstructions in shallow channels

Maggie J. Creed

Doctor of Philosophy

UNIVERSITY OF EDINBURGH

2016

Acknowledgements

First and foremost I would like to acknowledge the amazing support I received from my primary supervisor, Prof. Alistair Borthwick. His enthusiasm and in-depth knowledge of the subject and his willingness to share them with all of his students is an inspiration. I am truly grateful for the space that he gave me to mark out my own journey, but also for the constant support and ever-valuable advice that he offered along the way. I would also like to thank Gill and Alistair for treating me like family during my time in Edinburgh.

I am very grateful for the collaboration with my co-supervisor, Dr. Scott Draper. My time working at the University of Western Australia under Dr. Draper's guidance truly enriched my PhD experience. I am thankful to the Royal Society of Edinburgh Lessell's Travel Scholarship for having provided the financial support enabling this collaboration.

I would like to thank Prof. Paul Taylor (University of Oxford), Dr. Takafumi Nishino (Cranfield University), Dr. Ton van den Bremer (University of Edinburgh), and Prof. Nicholas Dodd, for discussions which helped to refine the analysis in several aspects of my thesis. I am grateful to the academics and students at BME, Budapest, including Prof János Józsa and Dr. Tamás Krámer, for having accommodated me during my exchange visit, and to Prof. Jinren Ni and his research team at Peking University for their kind welcome to Beijing.

There are many people who contributed to this fulfilling PhD experience, at University College Cork, UWA, Tsinghua University and the University of Edinburgh, including my office peers Joe, Kaswar, Monika, Nacho, Mahdi, Reza, Paul, Anna, Alex, David F. and Helen. In particular I would like to thank Sergio for the many interesting and enlightening conversations during these past years, both professional and personal.

I am truly grateful to the magnificent support of my Sat Nam Rasayan and Kundalini Yoga families, especially Hariraj, Har Kirat and Sharon, for their uplifting presence throughout this journey. Thank you to my wonderful friends and housemates here in Edinburgh - Anna, Nuria, Christos, Laura, Vicente, Yue Yao and David.

Lastly, I would like to extend my deepest gratitude to my parents and my amazing, inspiring siblings. I do not have enough words to express my appreciation to them, without whom this journey would not have been possible. Even in the moments when I doubted myself, the unfailing love, support and constant encouragement of my beautiful family kept me up.

Abstract

Many environmental free surface flows involve water and sediment transport. The net changes to the surface level of an erodible bed by sediment entrainment and deposition processes have a feedback effect on the local flow hydrodynamics. Bed morphological change is of great socio-economic and environmental importance in that it affects navigation, flood risk management, water quality, species diversity, and overall river sustainability.

This thesis describes a mathematical model of the depth-averaged shallow water-sediment equations based on mass and momentum conservation laws. A 2D numerical model is then presented of the fully coupled, variable-density governing equations, which are solved using a Godunov-type HLLC scheme. Dependent variables are specially selected in the numerical model to handle the presence of the variable-density mixture in the mathematical formulation. The model includes suspended sediment, bedload transport, and bed morphological change.

The numerical model is verified against benchmark analytical and semi-analytical solutions for complicated, clear water flows, bedload transport and suspended sediment transport. The well-balanced property of the governing equations is verified for a variable-density dam break flow over a bed step. Simulations of an idealised dam-break flow over an erodible bed, in excellent agreement with previously published results, validate the ability of the model to capture complex water-sediment interactions under rapidly-varying flow conditions and a mobile bed, and validate the eigenstructure of the system of variable-density governing equations. The model is then further validated against laboratory based data for complex 2D partial dam breaks over fixed and mobile beds, respectively. The simulations of 2D dam break flows over mobile beds highlight the sensitivity of the results to the choice of closure relationships for sediment transport. To investigate this further, a parameter study is carried out using a variety of commonly used empirical formulae for suspended sediment transport.

The numerical model is also used to inform a theoretical model that predicts the flow through and around a porous obstruction in a shallow channel. This problem is relevant to several practical applications, including flow through aquatic vegetation and the performance of arrays of tidal turbines in a finite-width tidal channel. The theoretical model is used to reinterpret the core flow velocities in laboratory-based data for an array of emergent cylinders in a shallow channel. Comparison with experimental data indicates the maximum obstacle resistance for which the theoretical model is valid. In a final application, the theoretical model examines the optimum arrangement of tidal turbines to generate power in a tidal channel, confirming that natural bed resistance increases the power extraction potential for a partial tidal fence.

Lay Summary

Theoretical and numerical models provide an important insight into the physics of earth surface flows, sediment transport and the interaction between these processes. Changes to riverbeds, floodplains and coastlines are of significant environmental and socio-economic importance in the current context of climate change, rising sea levels and extreme flood events.

This thesis presents a numerical model for predicting flow hydrodynamics, sediment transport and bed morphological changes. It is shown that the model has a wider range of applicability than previous models, and can be used effectively to simulate sediment transport under diverse environmental conditions.

A theoretical model is proposed to describe the flow through and around aquatic vegetation, arrays of tidal stream turbines and offshore structures, in shallow-water channels. The model is also applied to determine the optimum arrangement of tidal turbines placed in the centre of a wide tidal strait for maximum power extraction.

Declaration

I declare that this thesis was composed by myself, that the work contained herein is my own except where explicitly stated otherwise in the text, and that this work has not been submitted for any other degree or professional qualification except as specified.

Maggie J. Creed

Contents

Figures

Tables

Nomenclature

Common to all chapters

A	Grass constant (s^2m^{-1})
$\mathbf{A}$	Jacobian of the 1D system
$\mathbf{C}$	Jacobian matrix of 2D system of governing equations
C_c	contraction coefficient of flow through culvert
C_f	dimensionless bed friction coefficient
C_{cfl}	Courant-Friedrichs-Lewy number
D	deposition flux coefficient of suspended sediment
D_*	dimensionless grain diameter
E	entrainment flux coefficient
E_M	entrainment constant
$\mathbf{L}$	vector of left eigenvalues of $\mathbf{A}$
M	mass of water-sediment mixture (kg)
M_S	mass of suspended sediment (kg)
Q	flow discharge through an opening gate (ms^{-1})
$\mathbf{R}$	vector of right eigenvalues of $\mathbf{A}$
R_n	Rouse number
S_L, S_*, S_R	left, middle and right Riemann problem wave speeds
T	characteristic time constant (s)
$a = \sqrt{gh}$	local dynamic wave velocity (ms^{-1})
c	volumetric concentration of suspended sediment
c_a	near bed concentration of sediment
c_{eq}	bedload transport capacity concentration at equilibrium
d	median grain diameter (m)
$\mathbf{f}$	flux vector, x direction

g	acceleration due to gravity (9.81 ms^{-2})
$\mathbf{g}$	flux vector, y direction
h	depth of water-sediment mixture (m)
h_*	water depth in middle region of Riemann problem (m)
h_g	water depth flowing through an opening dam gate (m)
i	x-direction vector component
j	y-direction vector component
k	time level
m	power parameter for bedload transport equation
m_d	exponent in deposition flux formula
n	Manning coefficient ($sm^{1/3}$)
n_x	unit vector in x direction
n_y	unit vector in y direction
p_x	momentum of water-sediment mixture, x direction component ($kgms^{-1}$)
p_y	momentum of water-sediment mixture, y direction component ($kgms^{-1}$)
q	depth-averaged flow discharge (m^2s^{-1})
$\mathbf{q}$	vector of conserved variables
$\mathbf{q}_L, \mathbf{q}_R$	vector of conserved variables; left and right Riemann states
$\mathbf{q}_{*L}, \mathbf{q}_{*R}$	vector of conserved variables; Riemann states to left and right of S_*
q_b	cell-centred bedload transport rate (m^2s^{-1})
q_{b_x}	bedload transport rate, x direction component (m^2s^{-1})
q_{b_y}	bedload transport rate, y direction component (m^2s^{-1})
$\mathbf{r}$	ratio of consecutive gradients of variables
$\mathbf{s}$	vector of source terms
$s = \rho_s/\rho$	relative density
t	time (s)
u	fluid velocity, x direction component (ms^{-1})
u_*	x direction velocity component in the middle region of Riemann problem (ms^{-1})

u_f	local shear velocity (ms^{-1})
u_{b_x}	bedload velocity, x direction component (ms^{-1})
u_{b_y}	bedload velocity, y direction component (ms^{-1})
v	fluid velocity, y direction component (ms^{-1})
w_s	settling velocity of suspended sediment particles (ms^{-1})
x	distance in x direction (m)
y	distance in y direction (m)
z_b	bed elevation above given datum (m)
α_d	ratio of depth-averaged concentration of suspended sediment to near-bed concentration
α_e	coefficient for calculating entrainment rate
β	TVD slope limiter constant
β_x	bedslope in the x direction
β_y	bedslope in the y direction
δ_b	thickness of bedload layer (m)
η	free surface elevation above given datum(m)
κ	von Kármán constant
λ_i	eigenvalues of Jacobian, $\mathbf{C}$
ν	kinematic viscosity (m^2s^{-1})
ϕ_e	modification coefficient for MPM bedload transport formula under fast transient flows
ρ	water-sediment mixture density (kgm^{-3})
ρ_0	bed density (kgm^{-3})
ρ_s	sediment grain density (kgm^{-3})
ρ_w	clear water density (kgm^{-3})
τ_b	average bed shear stress (Nm^{-3})
τ_c	critical bed shear stress (Nm^{-3})
τ_{b_x}	bed shear stress, x direction component (Nm^{-3})
τ_{b_y}	bed shear stress, y direction component (Nm^{-3})
θ	dimensionless Shields parameter
θ_c	critical Shields parameter for horizontal bed
θ_x	x direction component of Shields parameter

θ_y	y direction component Shields parameter
θ_{cx}	modified critical Shields parameter for slope in x direction
θ_{cy}	modified critical Shields parameter for slope in y direction
ε	bed porosity
φ	angle of repose of the sediment
Δt	time step (s)
Δx	cell length in x direction (m)
Δy	cell length in y direction (m)
Ω	control volume
$\Phi(\mathbf{r})$	TVD slope limiter

Chapter 6

A_f	area of turbine fence
A_R	aspect ratio
A_t	swept are of turbine
B	blockage ratio
C_p	coefficient parametrising shear stress due to porous obstacle
F_c, F_b	seabed friction force components in the core and bypass flow
L, L_u, L_d	total, upstream and downstream scales (m)
N_c	number of cylinders per unit plan area of obstacle
S	stability number
T	thrust due to porous obstacle
U	characteristic channel velocity (ms^{-1})
W	width of open channel (m)
a_c	frontal area of cylinders per unit volume
c_D	local drag of cylinder
d_c	diameter of cylinder (or turbine)
k_p	resistance coefficient of porous obstacle
l	planar length of porous obstacle (m)
p_{x_i}	pressure at location x_i along channel (Pa)
s_t	spacing between adjacent turbines
u_c, u_b	core and bypass flow velocities (ms^{-1})
w, w_c, w_b	planar width of porous obstacle, core flow and bypass flow (m)

α_2, α_4, β_4	porous obstacle, obstacle wake and bypass velocity coefficients
τ_p	additional shear stress due to porous obstacle
ϕ	solid volume fraction

Chapter 1

Introduction and Literature Review

1.1 Water and Sediment - Setting the Scene

Accurate prediction of sediment-carrying shallow water flows is of great importance in river basin flood risk management, the planned dredging of navigation channels, bank erosion, bridge pier scour and the resilience of bridge support structures, the transport of contaminants, water quality, agriculture and fisheries, siltation of reservoirs, the raising and lowering of riverbed elevations, and long-term changes to river geometries. Climate change and anthropogenic impacts, partly due to increasing population and the construction of hydraulic structures, are having noticeable effects on fluvial hydraulics (see e.g. Miao *et al.*, 2010, 2011), and hence on flood and drought risk. In a detailed analysis, with the insurance industry in mind, Berz (2001) observed that flood events were responsible for one-third of all natural disasters worldwide and over half of the associated fatalities. In a more recent study, Zurich Insurance (2015) found a similar result in Nepal; between 2001-2008, one-third of natural disaster related deaths were caused by flood events.

Flood waves carry large amounts of sediment, with sizes ranging from fine clay and sand particles to larger debris such as cars and street furniture. The presence of mobile sediment particles can have a significant effect on the flow hydraulics (Raudkivi, 1998), particularly when the concentration of sediment is high, as is

the case with flood flows (Cao *et al.*, 2004). Scour of bridge piers and abutments is one of the most common causes of bridge failure during flood flows (Julien, 2010). Furthermore, much of the long-term damage to property and land after a flood event has subsided is due to the contaminated sediment left behind. Sediment transported in rivers can affect significantly the river species and biodiversity. For example, in the United Kingdom, the presence of increased quantities of fine suspended sediment in salmon and trout-spawning rivers inhibits the development of fish eggs because fine sediment reduces the availability of oxygen at gravel beds (Heywood and Walling, 2007). In contrast, in areas of China where man-made dams have reduced sediment loads downstream, a substantial decline in species has been observed (Yi *et al.*, 2010).

Extreme climate events are experienced across the globe; severe precipitation during monsoon season in India and Nepal, earthquake-induced landslides in China, large-scale flooding caused by hurricanes on the east coast of the USA, and long periods of drought along the west coast of North and South America, and in the Mediterranean. These events often occur in countries where populations are large and communities are socially and economically vulnerable. Without the finances to rebuild a community, a flood event can have devastating and long-lasting impacts on communities. The 2013 flood in Uttarakhand, which killed over 5000 people, was viewed as India's worst natural disaster in over a decade. Although construction of physical flood protection systems has helped reduce of the risk of damage, at least in the short term, it is becoming increasingly evident that physical barriers to water and sediment may not be the most viable and sustainable option (see, e.g. Silva *et al.*, 2004; van Ogtrop *et al.*, 2005; Wesselink *et al.*, 2015). In some cases, for example, dams and dykes built for flood control or hydropower generation have had devastating consequences on river biology and upstream communities (Wang and Hu, 2009; Julien, 2010). We therefore need to improve our understanding of the interaction between the water flow and sediment transport so that we can develop more accurate flood prediction maps which incorporate the effects of river bed aggradation and degradation. These maps can then be used to inform early warning systems, and to underpin effective post-flood community rebuilding projects. In the long term, this contributes to minimising

the risk of flood damage to humans, the environment, and the economy (Zurich Insurance, 2015). In a different context, it is possible that sediment transport contributes to the world carbon balance, with large river basins acting as carbon sinks or sources, or transitioning between the two (Ni *et al.*, 2012; Yue *et al.*, 2012).

A number of recent studies have highlighted the important role that sediment transport plays in river water quality and contaminant transport including Owens (2008) and Viers *et al.* (2009). From the 1970s, it was found that one of the major sources of high levels of phosphorous in the Great Lakes in the USA, where the algae concentrations were so high that the entire lakes were green and fish life was under severe threat, was from phosphorous attached to suspended sediment particles entering the lakes (Logan, 1987). Minerals and heavy metals accumulate in soils because of the large surface area of the soil particles. Materials transported by soil erosion can contain significant amounts of these contaminants which are then carried downstream and eventually result in high concentrations of heavy metals in river floodplains and in the sea (Viers *et al.*, 2009). In the past two decades we have witnessed the devastating effects caused by contaminated tailings dam break flows, such as the Ajka alumina reservoir breach in Hungary in 2004, when one million cubic metres of ŕed mud ́(iron oxide) spilled from the chemical factory reservoir and flooded the surrounding land and nearby towns, causing 15 deaths (Mayes *et al.*, 2011). In 2011, damage to a tailings dam at the Xichuan Minjiang Electrolytic Manganese Plant, China, resulted in manganese contamination of Fujiang River, a source of drinking water for over 200,000 people (http://www.wise-uranium.org/). Recently, on 5th November 2015, the Fundão tailings dam, Brazil, collapsed, releasing 60 000 m^3 of iron ore tailings, killing 19 people, and destroying the village of Bento Rodrigues, before reaching the Atlantic Ocean, approximately 600 km downstream, resulting in billions of US$ in damage (Marta-Almeida *et al.*, 2016).

Human activities can cause erosion rates to be 100 times greater than the natural rate (Julien, 2010). Construction of dams can lead to reservoir siltation because the natural flow of sediment is interrupted. It has been estimated that 66 % of the storage capacity of Chinese reservoirs is lost due to sedimentation

(Wang and Hu, 2009). Sediment is retained behind the dam, which deprives the downstream river of sediment required to maintain morphological equilibrium and support downstream ecosystems (Kondolf *et al.*, 2014). Sedimentation can also lead to severe erosion downstream (Wang *et al.*, 2005b), and it can provoke an increased risk of flooding upstream of the dam (Julien, 2010).

Asian rivers carry more than half of the world's sediment discharge to the sea, with the Yellow River, China, and the Ganges, India, being the largest contributors, and the Amazon, South America, being another large contributor (Syvitski *et al.*, 2005). The Yellow River in China is a prime example for river sedimentation and morphological evolution, demonstrating the importance of understanding sediment transport processes when developing flood risk management and water resource management strategies. Sedimentation in the lower Yellow River, China occurs at 5 - 10 cm/yr. The river bed is now more than 10 m greater than the surrounding flood plains in some areas, causing a severe risk of flooding and breaching of levees (Wang *et al.*, 2005a). Within 4 years of the impoundment of the Sanmenxia reservoir, located on the middle Yellow River, in 1960, the original storage capacity of the reservoir was reduced by 41.5% due to sediment deposition in the reservoir (Wang *et al.*, 2005a). Expensive dam reconstruction was required in the following decade to reverse this process and avoid future sediment build-up in the reservoir. This alleviated the increased risk of flooding of the land upstream of Sanmenxia, which had been exacerbated due to sediment build up and loss of water storage capacity in the upstream Yellow River and its surrounding tributaries. According to Wang *et al.* (2005a) sediment siltation of reservoirs is probably one of the most serious problems faced in order to manage sustainably the surface water resources of the Yellow River basin. Another major river in China, the Yangtze River, has experienced extensive changes in the past 50 years as a result of various water management projects (Yang *et al.*, 2006). In 2003, the Three Gorges Project (TGP) dam began as one of the largest power stations in the world. Yang *et al.* (2006) estimated that the sediment discharge into the East China Sea will be greatly reduced in the first 50 years after the construction of the TGP. Though they estimate that after 50 years the sediment discharge rate will stabilise as a result of the new equilibrium

achieved, in the next decades a reduced sediment discharge could provoke coastal erosion in the Changjiang (Yangtze) delta region, China's most affluent region. The construction of other large dams on the Yangtze river and its tributaries, such as Danjiangkou Reservoir on the Changjiang tributary, or dams built on the Jialingjiang tributary, has caused a decrease of more than 40% in the sediment discharge over the last 50 years at Datong, a city located 600 km from the river mouth (Yang *et al.*, 2006). In 2005 it was estimated that between 1% and 3% of the world's sediment flux, approximately 100 billion tons, is trapped behind man-made dams (Syvitski *et al.*, 2005). It is likely that this percentage is rising, owing to the increased construction of dams. For example, since the impoundment of the TGP dam in 2003, it has been estimated that over 118 Mt/yr of sediment is being trapped upstream of the dam (Xu and Milliman, 2009). In other words, a reduction of 90% in sediment discharge has been observed compared to pre-2003 levels. This problem of trapping sediment in man-made constructions has greatly reduced the amount of sediment transported from the rivers to the sea (Milliman and Meade, 1983) and, consequently, has a significant impact on coastal morphology, ocean ecosystems and the formation and maintenance of deltas. With more dams being constructed each year, particularly in Asia, this impact is likely to be exacerbated. The impact that dams have on sediment transport and river and coastal morphology is not confined to any one continent, however. There are over 80,000 dams in the USA, where extensive research has been carried out to assess the environmental and socio-economic impacts of dams, including the effects of their installation and demolition, the latter of which can de-stabilise the equilibrium achieved downstream of the dam, particularly for dams which have been in use for over 50 years. A comprehensive historical summary is given by Graf (2005). Later, Graf (2006) presented results outlining the profound contribution of regulating river structures on American rivers to modification of river habitats, often resulting in a less complex ecosystem and habitat loss, particularly for avian and riparian wildlife. Siltation is not a recent phenomenon. Historians and archeologists can trace siltation due to artificial river management back to the ancient civilisations of Mesopotamia and Egypt, and have found evidence that siltation was a major contributor to long-term changes in agriculture in those

regions (Jacobsen and Adams, 1958).

Due to the importance of sediment transport processes in shaping both inhabited and rural land, and the impact that sediment transport can have on the planning and development of civil engineering works, engineers and scientists have long been fascinated by this subject. The next section presents a brief historical account of the development of scientific understanding of sediment processes and numerical models used to simulate such processes.

1.2 Water and Sediment - Historical Context

Since humans have existed, man has been fascinated by water. Water has always been, and continues to be, a source of life - for food, for transport, for irrigation - and death - natural disasters, flood events, maritime accidents. Human fascination with water has been documented anecdotally for as long as people have been recording stories. Some of the earliest engineering projects can be traced back to fluvial hydraulics works over 6000 years ago, to the development of irrigation systems in Mesopotamia about 4000 - 5000 BC (Jacobsen and Adams, 1958), and the dredging works designed by Emperor Yu in China, to control the Great Flood in about 1920 BC (Wu *et al.*, 2016). From a different angle, another Great Flood - the Great Flood of Noah - was a fundamentally important event according to several of the world's major religions. Although scientific evidence for this flood, particularly its narrative in Genesis, is widely debated (Dundes, 1988), the Great Flood of Noah is another notable example of how flood events have shaped modern civilisations and society.

Modern scientific studies into fluvial hydraulics are thought to have commenced in the 15th century with Leonardo da Vinci (1452-1519), who carried out laboratory-based experiments and field observations of open channel flows (see McCurdy *et al.*, 1941). He was followed by many engineering historical figures who took interest in fluvial flows, among them Torricelli (1608-1647), Galileo (1564-1642), and Chézy (1718-1798). Du Buat (1734-1809) wrote the first textbooks on channel hydraulics, which included descriptions of sediment transport. Since the earliest modern scientific studies, hydraulics has become a central area

of scientific interest.

Today, many fluid mechanics studies rely heavily on numerical models. Boole (1860) was among the first to recognise how discrete methods could be useful in solving systems of partial differential equations. Later, Richardson (1910) used a finite difference approach to solve fluid flow problems on a domain divided into grid cells. Computational fluid mechanics began to take centre stage with the arrival of the computer in the 1950s. Pioneers include Charney *et al.* (1950), who modelled atmospheric flows, Godunov (1959), and Abbott (1979), who modelled water hydraulics using finite differences and the method of characteristics to discretise the governing equations. In the late 20th Century many major developments were made in the understanding of river flow and coastal hydraulics with the help of computational fluid dynamics (see e.g. Abbott and Basco, 1989; Fennema and Chaudhry, 1990; Toro, 1992; Mingham and Causon, 1998). Meanwhile, an increasing interest began to emerge in exploiting computational tools to improve the understanding of the interaction between water flow and sediment transport (see e.g. de Vriend, 1987; Capart and Young, 1998; Cao, 1999). One of the motivations behind the move towards using numerical methods to understand shallow-water and sediment processes was the recognition in the 1970s and 1980s that sediment transport was closely related to many major environmental problems, including the phosphorous pollution of the Great Lakes, USA, in the early 1970s (Logan, 1987), and the adverse affect of fine suspended sediment on gravel-spawing fish (Lisle, 1989).

1.3 Understanding Water-Sediment Flows

1.3.1 Mechanics of Water-Sediment Flows

One of the major challenges for studying environmental flows, particularly flows involving water-sediment mixtures, is the range of scales involved, in both time and space. Typically fluvial studies concern scales ranging from m to km. Sediment particles extend the problem to the micro, and even pico, scale. Sediment particles can vary in size from fine clay particles with diameters, $d < 1\mu m$, to coarse sand and gravel (mm), to large boulders (m) (see e.g. Soulsby, 1997, for

classification). Engineers are often concerned with erosion and deposition processes which occur in seconds, hours and days, on a relatively local scale. Geomorphologists study bathymetry and land changes which can occur in the short term, or can take place over hundreds or thousands of years and can be hundreds of km in extent. Recent dramatic environmental events illustrate the multi-disciplinary nature of sediment processes. For example, in 2010 a precipitation-induced landslide flood event in the Indus Valley, Pakistan, caused more sediment erosion in 30 minutes than had been observed cumulatively for the previous 1000 years (Sinclair *et al.*, 2016), illustrating the pressing need for engineers, geomorphologists, physicists, and social scientists to understand highly coupled water-sediment flows in the context of extreme climate events.

It is widely known that river morphological events depend primarily on the flow rate, sediment size, bed slope and sediment load (Raudkivi, 1998). Sediment transport can be classified into sheet flow, bedload, suspended sediment, and wash load, depending on the grain size and the flow rate. Sheet flow occurs when a thin layer of very high sediment concentration forms just above the bed, implying a high transport rate near the bed. This is often the dominant form of transport under storm conditions in coastal regions (Asano, 1995). Bedload involves the rolling, sliding and saltation (jumping) of particles along the surface of the bed. Bedload transport is predominant for slow flows or coarse sands and gravels. When the bed shear stress, induced by the flow, is close to the threshold shear stress, sediment particles are forced to roll along the bed until they find a new stable equilibrium. Saltation occurs when the drag and lift forces cause the grains to jump into the flow with a ballistic trajectory (McDowell and O'Connor, 1977). If the bed shear stress increases further, suspended sediment transport is induced as relatively fine material is just lifted into the flow by vertical turbulent fluxes, which exceed the grain fall velocities, and sediment is carried along by the water motion at a large fraction of the flow velocity (Bagnold, 1956). The particles are carried into suspension when the flow velocity is high, and settle out as the flow velocity reduces. Wash load flow is often comprised of very fine silt and clay particles carried high up into the flow, transported at the mean water flow velocity. As the present work considers non-cohesive sediment only, wash

load will not be investigated. In numerical models, one method for classifying the type of sediment transport can be made using the Rouse number, which is a ratio of the settling velocity of the sediment particle to the total friction velocity (Soulsby, 1997), as described later in Chapter 2.

1.3.2 Theoretical and Numerical Modelling of Sediment Transport

Several approaches exist to model sediment transport numerically, including;

- Kinetic theory, where sediment is described as a large number of small particles in constant motion, interacting with each other (Ni *et al.*, 2000);
- Lagrangian particle tracking, which can provide an insight into the behaviour of saltating particles near the bed (Niño and García, 1998);
- Smooth particle hydrodynamics (SPH), a rapidly emerging technique originally applied in astrophysics capable of a very high degree of accuracy, albeit at high computational effort (Fourtakas *et al.*, 2013);
- Discrete element methods (DEM), which have been widely used to model granular flows but only rarely to describe bedload transport (Frey and Church, 2011);
- Continuum approaches based on conservation laws.

In the continuum approach, such as the use of the finite volume method, the individual particles are ignored and the water-sediment mixture is considered as a continuous mass. The behaviour of the material is approximated over certain time and length scales by a set of governing differential equations. This assumption yields accurate results since the length scales of the computational domain are much greater than the individual particle diameter. Continuum methods are computationally very efficient, and can be very accurate after appropriate validation. For these reasons, the present work adopts a continuum, finite volume method approach.

When modelling sediment transport under fast-transient flood flows, for example dam-break flows, it is necessary to use a numerical solver which can account for flow discontinuities, such as hydraulic jumps. A generalisation of the dam-break problem can be described by the Riemann problem. (Toro, 2001). Godunov-type solvers are used to obtain a numerical solution of the Riemann problem, based on the method first presented by Godunov (1959). Since the pioneering work of Godunov (1959), many approximate Riemann solvers have been presented in the literature, including the schemes of Roe (1981), Osher and Solomon (1982), and the HLL solver (Harten-Lax-vanLeer, Harten *et al.*, 1983) and the HLLC scheme (Harten-Lax-vanLeer-Contact, Toro *et al.*, 1994a) solvers. To solve the Riemann problem, the shallow-water equations are written in their hyperbolic form, where the surface gradient terms in the momentum equation are split between the pressure flux gradient and source terms. This can provoke unphysical oscillations in the presence of a discontinuous bed, or at a wet-dry interface. Avoiding these oscillations requires a balancing technique. Various numerical and mathematical balancing techniques exist in the literature (see e.g. Bermúdez and Vázquez, 1994; Zhou *et al.*, 2002; Benkhaldoun *et al.*, 2007; Murillo and García-Navarro, 2013). Rogers *et al.* (2003) mathematically balanced the flux gradients and source terms, avoiding the need to implement a numerical balancing scheme. Later, Liang and Borthwick (2009) used a similar approach to derive the well-balanced shallow-water equations, where the equations are written in stage-discharge form, facilitating the solution of the Riemann problem for flow over complex topography and wet-dry fronts. Fraccarollo *et al.* (2003) note that the first-order accurate Riemann solvers (for example, Roe, HLL, HLLC solvers) are not adequate to resolve the complex wave-structure of a dam-break over a mobile bed. Fraccarollo *et al.* (2003) implemented a HLL-MUSCL scheme to ensure second-order accuracy. Xia *et al.* (2010) used a Roe-MUSCL solver to achieve second-order accuracy for their shallow water-sediment model, where the MUSCL-Hancock method is used to extrapolate the flux terms at the cell interfaces.

The physical processes involved in sediment transport are less well understood than the hydraulics of clear water flow, and many existing numerical models use

simplified assumptions to describe these processes. Several models have been developed to simulate steady flow over a mobile bed, separating the flow and sediment transport and solving them in a decoupled manner (see e.g. Hudson and Sweby, 2003; Castro Díaz *et al.*, 2008). These models neglect the feedback effect that the sediment transport has on the flow dynamics (Cao and Carling, 2002a). Hudson and Sweby (2003) suggested that the decoupled, steady flow approach can only be used for small values of Froude number and small changes to the bed. When dealing with dam break and flood flows, several models in the literature are limited to flows over fixed beds (Rogers *et al.*, 2001; Brufau *et al.*, 2002; Liang *et al.*, 2004). These models do not account for the strong feedback effect that sediment transport and rapidly-changing bed morphology have on the development of the flow.

A simplified method for modelling sediment transport is to use the concept of sediment transport capacity, where the sediment transport rate is a function of the local flow conditions only. This approach, which assumes that the concentration of sediment adapts rapidly to the local flow regime, reaching a constant, maximum (capacity) value, has been shown to be approximately valid for bedload transport (Cao *et al.*, 2011). However, in cases where high concentrations of suspended sediment are entrained into suspension, such as dam break flows, the assumption of the transport capacity can lead to violation of the conservation of mass of suspended sediment, which can result in substantial errors in certain cases, and is not universal (Cao *et al.*, 2012).

Over the past twenty years, great progress has been made in developing coupled shallow water-sediment numerical models for scenarios where either suspended sediment transport or bedload transport is dominant (see for example Cao *et al.*, 2004; Castro Díaz *et al.*, 2008; Leighton *et al.*, 2010; Juez *et al.*, 2015; Zhou, 2014). A coupled model solves the equations of conservation of mass and momentum of the water flow at the same time as the equations of conservation of mass of suspended sediment and/or bed morphology. Many models presented in the literature to date use modified versions of the governing variable-density equations, where the variable-density term of the water-sediment mixture is manipulated out of the conserved-variable terms and redistributed into the source

terms, increasing the complexity of the source terms (Cao *et al.*, 2004). Murillo *et al.* (2012) proposed an augmented Roe solver for the variable-density shallow water equations over a fixed bed where this manipulation was avoided. The model is well-balanced and yields accurate results, even in the presence of a bed discontinuity. Recently, this model was extended by Juez *et al.* (2015) to include suspended sediment transport but without bedload, where the hydrodynamic and suspended sediment equations are solved using finite volumes, and the bathymetry is updated using a finite difference scheme.

Several finite-volume solvers have been developed for bedload transport only, coupling the conventional constant density shallow-water equations with an Exner-type bed morphological equation - the latter which includes the gradient of the bedload discharge, and is sometimes incorporated into the Jacobian matrix of the complete system. This method is valid when the bedload discharge is expressed using a Grass-type formula, i.e. where the bedload discharge is expressed as a power of the flow velocity, often set to 3, multiplied by a coefficient. This coefficient is usually treated as a constant which must be calibrated for each specific case, a limitation of the method. Murillo and García-Navarro (2010) proposed a novel form of the Grass coefficient allowing it to be defined as a variable in a fully coupled model, thus extending the range of bedload formulae that could be used. However, determination of the eigenvalues for such a system is complex, and requires a large computational effort. Following Murillo and García-Navarro (2010), Juez *et al.* (2014) presented a weakly-coupled model for bedload transport which reduced the computation time.

Another continuum approach to solve the fully coupled water-sediment equations is use of a stratified two-layer model, consisting of a bottom layer of water-sediment mixture, and a clear-water layer above. The earliest two-layer models for dam break flows over mobile beds were presented by Capart and Young (1998) and Fraccarollo and Capart (2002), although one of the disadvantages was the assumed constant density of the water-sediment mixture lower layer. More recently, Li *et al.* (2013a) developed a double layer-averaged model for sediment-laden dam break flows over mobile beds, where the density of the lower layer can vary in space and time, reducing the error incurred by predefining a constant sediment

concentration in the lower layer. Maldonado-Villanueva (2015) advanced this idea further, introducing a model which does not rely heavily on empirical expressions for erosion and deposition of sediment, as used in the model of Li *et al.* (2013a).

It is common for models which account for both suspended sediment and bedload transport to group the two processes into the same sediment flux equation (e.g. Capart and Young, 1998; Cao *et al.*, 2004). This is often done by modelling the sediment load as *total load*, and is justified because of the difficulty that exists in determining the transition between bedload transport and suspended sediment transport under rapidly-varying flow conditions. However, it would be advantageous to develop a numerical model that can be used easily either when one of the two processes dominates at a particular point in time or space, or where there is large variability in sediment sizes.

In light of these previous developments, this thesis presents a new mathematical model of the fully coupled, unmanipulated, shallow water-sediment equations. Herein, the shallow water-sediment equations are derived from first principles using conservation of mass and conservation of momentum for the combined water-sediment mixture, similar to the approach used by Abbott (1979) for clear-water shallow flows. Unlike many of the above-cited models, the conserved variables are not manipulated to separate out the density terms of the water, sediment and water-sediment mixture. Instead the density terms remain as part of the conserved variables on the left hand side of the governing equations (see Chapter 2), thus preserving the conservative form of the governing equations. The model considers both suspended sediment transport and bedload transport, and is an extension of the 1D model of Leighton *et al.* (2010) and the 2D models of Apostolidou (2011) and Jiang *et al.* (2011). The corresponding numerical model is solved on a uniform, Cartesian grid using a second-order Godunov-type finite volume HLLC Riemann solver, coupled with a MUSCL-Hancock time-integration scheme, to ensures second-order accuracy in time. The solution to the Riemann problem is derived following Toro *et al.* (1994b) and a generalised version of the HLLC intermediate wave speed estimate (Toro, 2001) is presented to account for the variable-density property.

1.3.3 Shallow Flow through a Porous Obstacle

Shallow flow through a porous obstacle is commonly encountered in environmental fluid mechanics; examples include: flow in aquatic vegetation such as reeds and coastal or river bed vegetation (Zong and Nepf, 2011; Chen *et al.*, 2012); flow through a group of offshore pile foundations (Ball *et al.*, 1996); flow through a tidal stream turbine or array of turbines (Garrett and Cummins, 2007, 2013); and urban flood flows, where the porous obstacle could represent a group of buildings (Soares-Frazão *et al.*, 2008). In all of these scenarios it is important to estimate how changes in the porosity of the obstacle, and therefore changes in the obstacle's net resistance, will alter the velocity of the core flow passing through it. This is because the core flow velocity influences directly the hydrodynamic forces experienced by the constituent structures within the obstacle, as well as the flow structure in the wake of the obstacle, which can in turn affect the local environment, sediment transport, water quality and marine life.

In general, a shallow water flow must divert around an obstacle as its porosity reduces and the resistance to the flow increases. However, in any realistic scenario the functional relationship between porosity and the core flow velocity will be influenced by additional factors that inhibit or encourage flow diversion. Two common factors include natural bed resistance in the channel (which essentially defines the relative resistance of the obstacle) and lateral flow confinement, or channel blockage (which provides a geometric restriction on flow diversion when the channel is narrow relative to the obstacle width). A simple but practically relevant problem which incorporates these two factors is that of a uniformly porous obstruction in a shallow channel.

Chen and Jirka (1995), Chen *et al.* (2012), Zong and Nepf (2011), Takemura and Tanaka (2007), and Ball *et al.* (1996), among others, have conducted laboratory experiments of shallow flow around different arrangements of emergent rigid cylinders representing a porous obstacle in a channel, whilst Nicolle and Eames (2011) carried out 2D numerical simulations of flow through a circular arrangement of rigid cylinders. In these works the flow field and the shallow wake were explored for different cylinder spacing (i.e. different obstacle porosity or resistance) but the effects of both channel bed friction and channel blockage were

not systematically explored. In contrast to the foregoing experimental work on cylinder arrays, most theoretical work concerning arrays of tidal stream turbines has focused on the effect of channel blockage ratio on core flow velocity and, in turn, the power dissipated by a porous obstacle representing a single turbine or a row/array of turbines (e.g. Garrett and Cummins, 2007; Houlsby *et al.*, 2008; Nishino and Willden, 2012; Draper and Nishino, 2014). These studies of tidal stream turbine arrays have demonstrated that for a given obstacle resistance the core flow velocity and power extraction increases with blockage ratio; i.e. blockage is advantageous from the perspective of tidal power generation. However the majority of these studies are restricted to the assumption of a frictionless channel; the one exception being Garrett and Cummins (2013), who investigate the power that can be removed by a tidal turbine farm modelled as a circular patch in a frictional flow, but under the opposite restriction that the width of the channel was much larger than the width of the turbine farm, and so channel blockage was negligible. Motivated by this earlier body of work, it would be advantageous to explore the solution for the depth-averaged core flow velocity passing through a porous obstacle, accounting for the combined influence of porosity (or obstacle resistance), channel blockage and natural friction.

1.4 Aims and Objectives

The main aim of this thesis is to develop a robust shock-capturing numerical model to solve the fully coupled depth-averaged shallow water-sediment equations in 2D, including bedload and suspended sediment transport and bed morphological change. The shock-capturing scheme allows the solver to be extended to model free surface flows which exhibit discontinuities, such as dam-break induced flows. The mathematical model preserves the fully conservative, well-balanced, hyperbolic form of the governing equations. The numerical model is used to investigate the region of validity of the shallow water equations for fast, unsteady flows over a mobile bed, and for flow through a porous obstacle in a shallow channel.

The objectives of the present work are summarised as follows:

1. To develop a numerical model of the shallow water-sediment equations, and extend the solution of the HLLC Riemann solver wave speeds to include the variable-density term of the water-sediment mixture,

2. To use the numerical model to simulate 2D partial dam breach flow over mobile beds, and investigate the fully-coupled water-sediment interactions.

3. To propose an approximate theoretical model describing flow through a porous obstacle in a shallow channel, validated against previously published experimental data (Ball *et al.*, 1996; Zong and Nepf, 2011; Chen *et al.*, 2012) of flow through a vegetative patch in a laboratory flume. Results are used to study the effect of channel blockage ratio on flow velocities, and the importance of background channel friction for power extraction of tidal stream turbines

1.5 Synopsis

The remainder of the thesis is structured as follows.

Chapter 2 details the mathematical background of this work, including the derivation of the variable-density shallow water-sediment governing equations. A convenient form of the governing equations is presented to facilitate the numerical solution of the conserved variables. Model closure relationships are also presented, particularly those required for sediment transport. In **Chapter 3**, the extension of the HLLC Riemann solver to variable-density shallow water flows is covered. Special attention is given to the solution of the intermediate wave speed of the Riemann problem. The second-order accurate, MUSCL-Hancock time integration scheme, and the finite difference scheme for the bed morphological equation are also described. **Chapter 4** presents verification tests of the numerical model for clear water flows, and suspended sediment transport or bedload transport in steady flows. In **Chapter 5**, the numerical model is validated extensively against laboratory based data for complicated 2D dam breach flows over fixed and mobile beds. For the mobile bed cases, two experimental tests are investigated; one involving a coarse-grained bed, where bedload transport dominates; and the other involving fine sand grains, where suspended sediment is the dominant sediment

transport process. **Chapter 6** features a theoretical model used to describe flow through a porous obstacle in a shallow channel. Theoretical model predictions are compared with laboratory-based data of flow through an array of emergent rigid cylinders in a shallow channel. The theoretical model is then applied to explore the affect of natural bed roughness on the power efficiency of an array of tidal turbines in a finite-width channel. Lastly, final conclusions of this work, and subsequent recommendations for future work are discussed in **Chapter 7**.

1.6 Published Work

A significant part of the work presented this thesis has been published recently in two peer-reviewed journal papers:

- The work from Chapters 2-5 is presented in; M.J. Creed, A.G.L. Borthwick, P. Taylor, I.G. Apostolidou. A finite-volume shock-capturing solver of the fully coupled shallow water-sediment equations. *International Journal of Numerical Methods in Fluids*, 2017 (Creed *et al.*, 2017b).

- The substantial part of Chapter 6 has been compiled in; M.J. Creed, S. Draper, T. Nishino, A.G.L. Borthwick. Efficiency of a tidal fence in a shallow tidal channel. *Proceedings of the Royal Society of London A: Mathematical, Physical and Engineering Sciences*, 2017 (Creed *et al.*, 2017a).

Chapter 2

Mathematical Model

2.1 Introduction

This chapter presents the governing 2D shallow-water sediment equations (SWSE). The SWSE are first derived from principles of conservation of mass and momentum. The governing equations are then rewritten in their well-balanced, stage-discharge form. A convenient form of the SWSE is then presented, with the aim of facilitating the numerical solution. Finally, closure relationships are defined for interactions between the flow, the mobile bed and sediment particles.

2.2 Governing Equations

The depth-averaged shallow water-sediment equations, an extension of the shallow water equations, describe the flow of water-sediment mixtures in situations where horizontal length scales are much greater than the vertical water depth. The fluid is incompressible, inviscid and irrotational. Vertical particle acceleration is assumed to be negligible and the pressure is hydrostatic. Complete vertical mixing of the velocity and fluid density is also assumed when sediment is present in suspension. Hence, in shallow water-sediment models, the horizontal velocity component and the concentration of the suspended sediment are homogeneous over the depth. In the present study, sediment is non-reactive and diffusion of sediment is neglected.

The shallow water equations can be derived by integrating continuity and

Navier-Stokes equations over the vertical depth (see for example, Falconer, 1993), or by considering the conservation of mass and momentum over the depth of a control volume of infinitesimal plan area (see Abbott, 1979). In this chapter, the latter method is used to derive the shallow water-sediment equations, following Yan (2010).

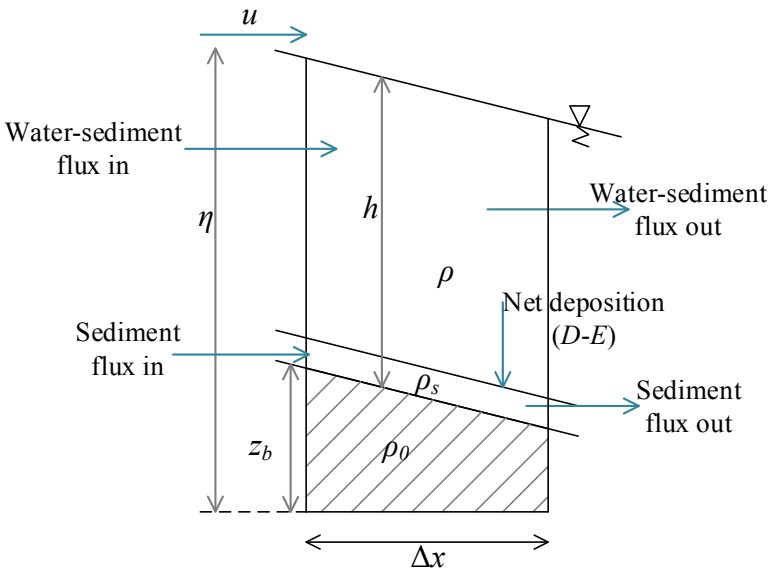

Figure 2.1: 1D control volume of bed and water sediment mixture, including mass fluxes.

Consider an infinitesimally thin element, Figure 2.1, with length Δx , and water depth h. The liquid-sediment mixture passes through the element with depth-integrated horizontal velocity components, u and v. Following Yan (2010), equations for the conservation of mass and momentum of the water-sediment mixture, the conservation of mass of suspended sediment, and the conservation of bed material are obtained by integrating over a control volume in a small time interval Δt.

2.2.1 Mass Conservation of Water-Sediment Mixture

For simplicity, the continuity equation is derived in the x direction only, considering the total mass of water-sediment mixture and bed material in the control volume (CV) in Figure 2.1, and the mass flux of water and sediment through CV. In the following derivation it is assumed that the height of the bedload layer, $\delta_b \ll h$, a reasonable assumption since $\delta_b \approx 2d$ is often used, where d is the me-

dian particle diameter (Einstein, 1950). Thus, the depth of the water-sediment mixture is taken from the surface level of the bed above the datum, z_b, to the free surface elevation above the datum (or stage), η, i.e., δ_b is included in h. However, the mass flux of bed material is calculated as the mass flux of sediment in the bedload layer, $\rho_s q_{bx} \Delta x$, where ρ_s is the density of the sediment grains and q_{bx} is the bedload discharge in the x direction. With this in mind, the accumulation of mass in CV is the sum of the mass per unit breadth of water-sediment mixture and the mass per unit breadth of the bed in time Δt:

$$\frac{\partial}{\partial t}(\rho h + \rho_0 z_b)\Delta x \Delta t \ ,$$

where h is the local depth of water-sediment mixture, ρ is the depth-averaged variable density of the water-sediment mixture, ρ_0 is the density of the bed and z_b is bed elevation above a given datum (δ_b is neglected from z_b). Ignoring non-linear terms in the Taylor series expansion, the sum of the mass flux entering CV and the mass flux leaving CV, is

$$\Big(\frac{\partial}{\partial x}(\rho h u) + \frac{\partial}{\partial x}(\rho_s q_{bx})\Big)\Delta t \Delta x \ .$$

Ensuring conservation, the accumulation of mass must equal the total mass flux such that,

$$\frac{\partial}{\partial t}\big(\rho h + \rho_0 z_b\big) = -\frac{\partial \rho h u}{\partial x} - \frac{\partial \rho_s q_{bx}}{\partial x} \ . \tag{2.1}$$

If bed porosity is assumed constant in time, ρ_0 is constant and (2.1) is rewritten as the equation of conservation of mass of the water-sediment mixture:

$$\frac{\partial \rho h}{\partial t} + \frac{\partial \rho h u}{\partial x} = -\rho_0 \frac{\partial z_b}{\partial t} - \rho_s \frac{\partial q_{bx}}{\partial x} \ . \tag{2.2}$$

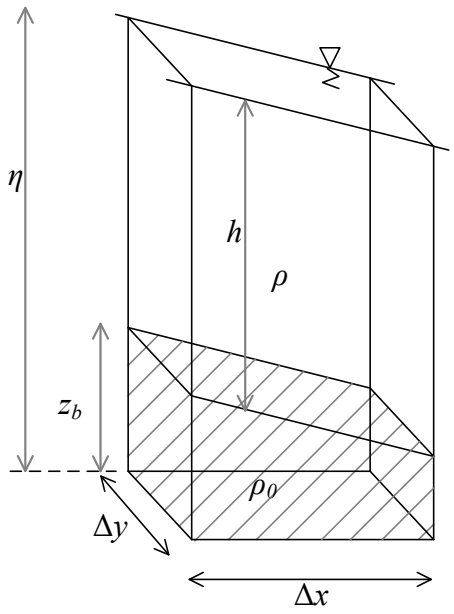

Figure 2.2: Control volume of bed and water sediment mixture in 2D, where Δx and Δy are element dimensions in the x and y directions, respectively.

Equation (2.2) can be extended to two dimensions resulting in,

$$\frac{\partial \rho h}{\partial t} + \frac{\partial \rho h u}{\partial x} + \frac{\partial \rho h v}{\partial y} = -\rho_s \frac{\partial q_{b_x}}{\partial x} - \rho_s \frac{\partial q_{b_y}}{\partial y} - \rho_0 \frac{\partial z_b}{\partial t} \ . \tag{2.3}$$

In the x and y directions respectively, u and v are velocity components, and q_{bx} and q_{by} are bedload discharge components, defined in Section 2.4.

2.2.2 Momentum Conservation of Water-Sediment Mixture

The accumulation of momentum in CV over time Δt equals the sum of the forces acting on CV; including, the balance of the impulse-momenta at the inflow and outflow, the weight component of the water-sediment mixture, and bed shear stresses. During a time interval Δt, across CV of width Δx, the total accumulation of momentum within CV, or the rate of change of momentum, is

$$\Big(\frac{\partial \rho u h}{\partial t} + \frac{\partial \rho_s q_{bx}}{\partial t} \Big) \Delta x \Delta t \ . \tag{2.4}$$

The sum of the momentum fluxes across CV is

$$-\Big(\frac{\partial \rho u^2 h}{\partial x} + \frac{\partial \rho_s u_{bx} q_{bx}}{\partial x}\Big)\Delta x \Delta t \ , \tag{2.5}$$

where $u_{bx} = q_{bx}/\delta_b$ is the bedload velocity, and δ_b is the approximate height of the bedload layer. The total impulse is

$$-\Big(\frac{\partial}{\partial x}(\rho g h^2) + \tau_{bx} + \rho g h \frac{\partial z_b}{\partial x}\Big)\Delta x \Delta t \ , \tag{2.6}$$

where the first term is due to hydrostatic pressure, the second term is related to bed friction and the third term accounts for body acceleration along the continuum.

Equating (2.4) to the sum of (2.5) and (2.6), dividing both sides by $\Delta x \Delta t$ and rearranging, we obtain the equation of conservation of momentum of water-sediment mixture in 1D:

$$\frac{\partial \rho h u}{\partial t} + \frac{\partial}{\partial x}\big(\rho u^2 h + \rho g h^2\big) = -\rho_s \frac{\partial q_{bx}}{\partial t} - \rho_s \frac{\partial u_{bx} q_{bx}}{\partial x} - \rho g h \frac{\partial z_b}{\partial x} - \tau_{bx} \ . \tag{2.7}$$

Equation (2.7) can be extended to two horizontal dimensions resulting in,

$$\frac{\partial \rho u h}{\partial t} + \frac{\partial}{\partial x}\big(\rho u^2 h + \frac{1}{2}\rho g h^2\big) + \frac{\partial (\rho u v h)}{\partial y}$$

$$= -\rho_s \frac{\partial q_{b_x}}{\partial t} - \rho_s \frac{\partial}{\partial x}(u_{b_x} q_{b_x}) - \rho g h \frac{\partial z_b}{\partial x} - \tau_{b_x} \ , \tag{2.8a}$$

and, $$\frac{\partial \rho v h}{\partial t} + \frac{\partial}{\partial y}\big(\rho v^2 h + \frac{1}{2}\rho g h^2\big) + \frac{\partial (\rho u v h)}{\partial x}$$

$$= -\rho_s \frac{\partial q_{b_y}}{\partial t} - \rho_s \frac{\partial}{\partial y}(u_{b_y} q_{b_y}) - \rho g h \frac{\partial z_b}{\partial y} - \tau_{b_y} \ . \tag{2.8b}$$

2.2.3 Mass Conservation of Suspended Sediment

The total accumulation of mass of suspended sediment in CV during time Δt is

$$\frac{\partial \rho_s ch}{\partial t} \Delta x \Delta t \ ,$$

where c is the depth-averaged volumetric concentration of suspended sediment. The total mass flux of suspended sediment across CV in Δt is

$$-\frac{\partial \rho_s ch}{\partial x} \Delta x \Delta t \ ,$$

and the net deposition (or entrainment) of sediment on the bed is given by

$$-\rho_s (D - E) \Delta x \Delta t \ ,$$

where D and E (calculated using empirical formula as discussed in Section 2.4) are the coefficients of deposition and entrainment of suspended sediment, respectively. Again, using mass continuity, we obtain the one-dimensional equation for the conservation of suspended sediment:

$$\frac{\partial \rho_s ch}{\partial t} + \frac{\partial \rho_s uch}{\partial x} = -\rho_s (D - E) \ , \tag{2.9}$$

or in two dimensions,

$$\frac{\partial \rho_s hc}{\partial t} + \frac{\partial \rho_s huc}{\partial x} + \frac{\partial \rho_s hvc}{\partial y} = -\rho_s (D - E) \ . \tag{2.10}$$

2.2.4 Mass Conservation of Bed Material

The total bed material in CV (Figure 2.1) is the sum of the material in the bed plus the material in the bedload layer. As mentioned previously, because $\delta_b \ll z_b$, the height of the bedload layer δ_b is neglected in the following derivation.

The accumulation of mass of bed material in CV is $\rho_s z_b(1-\varepsilon)\Delta x \Delta t$, where ε is the bed porosity. From conservation, equating the accumulation of mass of bed material in CV during time Δt, to the sum of the changes due to bedload transport plus net deposition of suspended sediment, and dividing by $\rho_s(1-\varepsilon)\Delta x \Delta t$, the equation for conservation of bed material in 1D is given by,

$$\frac{\partial z_b}{\partial t} = \frac{1}{(1-\varepsilon)}\Big(-\frac{\partial q_{b_x}}{\partial x} + D - E\Big) \ . \tag{2.11}$$

This is extended to 2D giving,

$$\frac{\partial z_b}{\partial t} = \frac{1}{(1-\varepsilon)}\Big(-\frac{\partial q_{b_x}}{\partial x} - \frac{\partial q_{b_y}}{\partial y} + D - E\Big) \ . \tag{2.12}$$

2.2.5 Summary of the Governing Equations

In 1D the depth-averaged equations for conservation of mass and momentum of the water-sediment mixture (x and y directions), conservation of mass of suspended sediment, and conservation of bed material can be summarised as:

$$\frac{\partial \rho h}{\partial t} + \frac{\partial \rho h u}{\partial x} = -\rho_s \frac{\partial q_{b_x}}{\partial x} - \rho_0 \frac{\partial z_b}{\partial t} \ , \tag{2.13a}$$

$$\frac{\partial \rho h u}{\partial t} + \frac{\partial}{\partial x}\big(\rho u^2 h + \rho g h^2\big) = -\rho_s \frac{\partial q_{bx}}{\partial t} - \rho_s \frac{\partial u_{bx} q_{bx}}{\partial x} - \rho g h \frac{\partial z_b}{\partial x} - \tau_{bx} \tag{2.13b}$$

$$\frac{\partial \rho_s h c}{\partial t} + \frac{\partial (\rho_s h u c)}{\partial x} = -\rho_s (D - E) \ , \tag{2.13c}$$

$$\text{and,} \quad \frac{\partial z_b}{\partial t} = \frac{1}{(1-\varepsilon)}\Big(-\frac{\partial q_{b_x}}{\partial x} + D - E\Big) \ . \tag{2.13d}$$

The corresponding depth-averaged 2D equations are:

$$\frac{\partial \rho h}{\partial t} + \frac{\partial \rho u h}{\partial x} + \frac{\partial \rho v h}{\partial y} = -\rho_0 \frac{\partial z_b}{\partial t} - \rho_s \frac{\partial q_{b_x}}{\partial x} - \rho_s \frac{\partial q_{b_y}}{\partial y} \ , \tag{2.14a}$$

$$\frac{\partial \rho u h}{\partial t} + \frac{\partial}{\partial x}\big(\rho u^2 h + \frac{1}{2}\rho g h^2\big) + \frac{\partial(\rho u v h)}{\partial y}$$

$$= -\rho_s \frac{\partial q_{b_x}}{\partial t} - \rho_s \frac{\partial}{\partial x}(u_{b_x} q_{b_x}) - \rho g h \frac{\partial z_b}{\partial x} - \tau_{b_x} \ , \tag{2.14b}$$

$$\frac{\partial \rho v h}{\partial t} + \frac{\partial}{\partial y}\big(\rho v^2 h + \frac{1}{2}\rho g h^2\big) + \frac{\partial(\rho u v h)}{\partial x}$$

$$= -\rho_s \frac{\partial (q_{b_y})}{\partial t} - \rho_s \frac{\partial}{\partial y}(u_{b_y} q_{b_y}) - \rho g h \frac{\partial z_b}{\partial y} - \tau_{b_y} \ , \tag{2.14c}$$

$$\frac{\partial \rho_s h c}{\partial t} = -\frac{\partial(\rho_s h u c)}{\partial x} - \frac{\partial(\rho_s h v c)}{\partial y} - \rho_s (D - E) \ , \tag{2.14d}$$

$$\text{and,} \quad \frac{\partial z_b}{\partial t} = \frac{1}{(1-\varepsilon)}\Big(-\frac{\partial q_{b_x}}{\partial x} - \frac{\partial q_{b_y}}{\partial y} + D - E\Big) \ , \tag{2.14e}$$

where h is the local depth of water-sediment mixture, ρ is the depth-averaged density of water-sediment mixture, ρ_s is the density of the sediment, u and v are mean flow velocity components in the x and y directions, respectively, t is time, z_b is bed elevation, u_{bx} and u_{by} are bedload velocities, and q_{bx} and q_{by} are bedload discharge components in the x and y directions, ε is bed porosity, g is acceleration due to gravity, and D and E quantify deposition and entrainment, representing the exchange of sediment between the bed and the fluid (discussed in greater detail in Section 2.4). The bed shear stress components, τ_{bx} and τ_{by},

are estimated from the following empirical expressions;

$$\tau_{bx} = \rho C_f u\sqrt{u^2+v^2}, \quad \text{and} \quad \tau_{by} = \rho C_f v\sqrt{u^2+v^2}, \tag{2.15}$$

in which C_f is the dimensionless bed friction coefficient. The bed density is

$$\rho_0 = \rho_w \varepsilon + \rho_s(1-\varepsilon), \tag{2.16}$$

where ρ_w is the density of clear water. The depth-averaged density of the water-sediment mixture ρ is a function of the depth-averaged volumetric concentration of suspended sediment c, such that

$$\rho = \rho_w + c(\rho_s - \rho_w) \ . \tag{2.17}$$

Rearranging (2.17) we can write the concentration of suspended sediment as a function of the densities of water, sediment, and water-sediment mixture;

$$c = \frac{\rho - \rho_w}{\rho_s - \rho_w} \ . \tag{2.18}$$

Profile factors, which arise from depth-averaging the governing equations to account for the non-uniform vertical distribution of concentration and velocity, are omitted in the above equations because they are set to unity for the purpose of this study. In the absence of bedload transport, suspended sediment transport and bed morphological change, when the density of the fluid is constant, (2.14a) - (2.14e) reduce to the classical shallow water equations of conservation of mass and momentum.

At this point it is important to note that (2.14) is valid only for horizontal or gently sloping beds. In the numerical solution of flow over variable bathymetry

with steep gradients, instabilities develop in the free surface because the surface gradient terms in the momentum equations (2.14b) and (2.14c) are split between the pressure flux gradient term, $\frac{1}{2}\rho g h^2$, and the source term which accounts for the bed slope, $\rho g h \frac{\partial z_b}{\partial y}$ (see, e.g. Rogers *et al.*, 2003). Avoiding these unphysical instabilities requires a balancing technique. In the present study, an algebraic balancing technique is employed to prevent such instabilities arising, based on a similar approach used by Liang and Borthwick (2009), in which the equations are written in term of the stage η. This avoids the need to implement a numerical balancing technique, which can increase the complexity of the numerical scheme.

2.3 Mathematical Balancing of the SWSE

Letting the water depth, $h = \eta - z_b$, where η is the free surface elevation above a given datum, and following a similar approach to Rogers *et al.* (2003) and Liang and Borthwick (2009), (2.14) is rewritten as,

$$\frac{\partial \rho\eta}{\partial t} + \frac{\partial \rho uh}{\partial x} + \frac{\partial \rho vh}{\partial y} = -\rho_0 \frac{\partial z_b}{\partial t} - \rho_s \frac{\partial q_{b_x}}{\partial x} - \rho_s \frac{\partial q_{b_y}}{\partial y} + \frac{\partial \rho z_b}{\partial t} \ , \tag{2.19a}$$

$$\frac{\partial \rho uh}{\partial t} + \frac{\partial}{\partial x}\Big(\rho u^2 h + \frac{1}{2}\rho g(\eta^2 - 2\eta z_b)\Big) + \frac{\partial(\rho uvh)}{\partial y}$$

$$= -\rho_s \frac{\partial q_{b_x}}{\partial t} - \rho_s \frac{\partial}{\partial x}(u_{b_x} q_{b_x}) - \rho g \eta \frac{\partial z_b}{\partial x} + \frac{1}{2} g z_b^2 \frac{\partial \rho}{\partial x} - \tau_{b_x} \ , \tag{2.19b}$$

$$\frac{\partial \rho vh}{\partial t} + \frac{\partial}{\partial y}\Big(\rho v^2 h + \frac{1}{2}\rho g(\eta^2 - 2\eta z_b)\Big) + \frac{\partial(\rho uvh)}{\partial x}$$

$$= -\rho_s \frac{\partial q_{b_y}}{\partial t} - \rho_s \frac{\partial}{\partial y}(u_{b_y} q_{b_y}) - \rho g \eta \frac{\partial z_b}{\partial y} + \frac{1}{2} g z_b^2 \frac{\partial \rho}{\partial y} - \tau_{b_y} \ , \tag{2.19c}$$

$$\frac{\partial \rho_s hc}{\partial t} = -\frac{\partial(\rho_s huc)}{\partial x} - \frac{\partial(\rho_s hvc)}{\partial y} - \rho_s(D - E) \ , \tag{2.19d}$$

$$\text{and} \quad \frac{\partial z_b}{\partial t} = \frac{1}{(1-\varepsilon)}\Big(-\frac{\partial q_{b_x}}{\partial x} - \frac{\partial q_{b_y}}{\partial y} + D - E\Big) \; . \tag{2.19e}$$

The system of equations given by (2.19) is *well-balanced* because the pressure terms of the momentum equations are implicitly balanced in the mathematical formulation. The advantage of using the above well-balanced equations is that the numerical model is now more generally applicable than (2.14), as demonstrated in Chapter 4, without the need for additional numerical balancing techniques.

2.4 Model Closure

To close the above system of governing equations, it is necessary to define parameters which describe the bed shear stresses, the sediment flux exchange between the bed layer and the liquid-sediment mixture, and the transport of material along the bed. Appropriate selection of the empirical parameters is paramount for obtaining a physically relevant numerical solution.

2.4.1 Bed Friction

In the following test cases C_f, the dimensionless bed friction coefficient, is defined using the Manning equation such that

$$C_f = \frac{gn^2}{h^{1/3}}, \tag{2.20}$$

where, n is the Manning coefficient ($\text{sm}^{-1/3}$).

2.4.2 Bedload and Suspended Sediment Transport

When the flow velocity exceeds a certain threshold value (see e.g. Soulsby, 1997), sediment can be transported along the bed by rolling, saltating, or sliding of particles. This bedload transport is traditionally defined by the bedload discharge components, q_{bx} and q_{by}, and bedload particle velocity components, u_{bx} and u_{by}. If the flow velocity increases further and the shear velocity u_f exceeds the set-

tling velocity of the particles w_s, particles are entrained into suspension. Later, when the flow velocity reduces, these particles can be deposited on the bed. Entrainment and deposition coefficients, E and D respectively, are used to express the processes which define this exchange of sediment between the bed and the water-sediment mixture.

The present study does not aim to present a comprehensive analysis of existing sediment transport formulae and empirical expressions. For the purpose of verifying the mathematical model presented above, and investigating some interesting properties of fully coupled water-sediment modelling, parameters are described using a selection of well-established empirical formulae taken from the literature.

The bedload discharge components in the x and y directions are expressed with either (1) the simple sediment transport flux, originally proposed by (Grass, 1981):

$$q_{bx} = Au\big(\sqrt{u^2+v^2}\big)^{m-1} \quad \text{and,} \quad q_{by} = Av\big(\sqrt{u^2+v^2}\big)^{m-1}, \tag{2.21}$$

where A is a dimensional constant, which incorporates grain diameter and kinematic viscosity, and m is a power parameter, which is normally defined as $m = 3$; or (2) the widely used Meyer-Peter-Mueller formula (Meyer-Peter and Müller, 1948),

$$q_{bx} = 8\sqrt{(s-1)gd^3}(\theta_x - \theta_{cx})^{3/2}, \tag{2.22a}$$

$$q_{by} = 8\sqrt{(s-1)gd^3}(\theta_y - \theta_{cy})^{3/2}, \tag{2.22b}$$

where d is the median diameter of the sediment particle, $\theta_x = \frac{\tau_{bx}}{\rho(s-1)gd}$ and $\theta_y = \frac{\tau_{by}}{\rho(s-1)gd}$ are the components of the dimensionless shear stress (Shields parameter) in the x and y directions. The relative density of sediment $s = \rho_s/\rho$. The above formulae were derived for bedload transport on horizontal or mildly-sloping channels. Several authors have proposed modifications which account for

the influence that bed-slope can have on bedload transport (e.g. Soulsby, 1997; Johnson and Zyserman, 2002; Maldonado-Villanueva, 2015); either modifying the critical Shields parameter which controls the initiation of sediment transport, or by including a modification coefficient when calculating the bedload transport discharge. In this work, the former method is implemented; the modified critical Shields parameters, θ_{cx} and θ_{cy}, which account for the influence that bed-slope can have on bedload transport, and are given by (Soulsby, 1997);

$$\theta_{cx} = \theta_c \frac{\sin(\varphi + \beta_x)}{\sin\varphi} \quad \text{and} \quad \theta_{cy} = \theta_c \frac{\sin(\varphi + \beta_y)}{\sin\varphi}, \tag{2.23a}$$

where β_x and β_y represent the angles of the bed slope in the x and y directions, φ is the angle of repose of the sediment, and θ_c is the critical Shields parameter for the initiation of sediment transport on an horizontal bed.

When sediment is present in suspension, it is necessary to define the deposition and entrainment fluxes; D and E. It is well known that D can be described as a function of the near bed concentration and the settling velocity of particles (Cao and Carling, 2002b; Garcia and Parker, 1991). Following Cao *et al.* (2004) and Cao (1999), the deposition flux coefficient of suspended sediment is given by

$$D = w_s \alpha_d c (1 - \alpha_d c)^{m_d} \ , \tag{2.24}$$

where m_d is an exponent. Setting $m_d > 0$ accounts for hindered settling velocity, caused by the presence of sediment particles in suspension (Richardson and Zaki, 1954). The settling velocity of the sediment particles, w_s, is calculated using the empirical formula of Zhang and Xie (1993),

$$w_s = \frac{\nu}{d}\Big[\sqrt{10.36^2 + 1.049(1-c)^{4.7} {D_*}^3} - 10.36\Big], \tag{2.25}$$

where ν is the kinematic viscosity and D_* is the dimensionless grain diameter,

$$D_* = \Big(\frac{g(s-1)}{\mu^2}\Big) d \ . \tag{2.26}$$

The deposition coefficient α_d relates the depth-averaged concentration of suspended sediment c, to the near-bed concentration c_a. For flows which can carry large concentrations of suspended sediment, the value of α_d remains uncertain, but generally, $\alpha_d > 1$. For hyperconcentrated flows, as the depth-averaged concentration increases and $c \to c_a, \alpha_d \to 1$. To ensure that c_a cannot exceed $(1-\varepsilon)$, which is physically inadmissible, following (Cao *et al.*, 2004);

$$\alpha_d = \min\Big[2, \frac{1-\varepsilon}{c}\Big] \ . \tag{2.27}$$

In the literature many different empirical formulae have been presented for estimating the entrainment function E, which is usually a function of the flow velocity, bed shear stresses and physical characteristics of the sediment (see for example, Van Rijn, 1984b; Garcia and Parker, 1991; Cao *et al.*, 2004, 2006). The numerical model results are highly sensitive to the choice of formula. In this study, two different formulae are tentatively employed in the test cases in Chapters 4 and 5, depending on the flow conditions and sediment characteristics.

For scenarios where large volumes of fine sediment can be entrained into suspension, the formula given by Cao *et al.* (2004) is used,

$$E = \begin{cases} \alpha_e(\theta - \theta_c) u h^{-1} d^{-0.2} & \text{if } \theta \geq \theta_c \ , \\ 0 & \text{else,} \end{cases} \tag{2.28}$$

where $\theta = \frac{\tau_b}{\rho(s-1)gd}$ is the local Shields parameter with the local bed shear stress, $\tau_b = \sqrt{\tau_{bx}^2 + \tau_{by}^2}$. The coefficient α_e in (2.28), an empirical dimensional constant (see Cao, 1999; Cao *et al.*, 2004), is a function of grain diameter (m), sediment density, bed porosity, and critical Shields parameter, and has to be calibrated for

each specific case.

Under certain hydraulic conditions, particularly when the bed is composed of coarse sediment, the depth-averaged concentration of suspended sediment remains small. In a sense, the dominant mode of transport could be described as bedload. However, use of the traditional Exner-type bedload transport formula, such as (2.22), does not allow for small local entrainment and deposition of particles. If E and D are neglected from (2.14e), certain bed forms may not be captured. One method of admitting sediment entrainment while ensuring that the depth-averaged volumetric concentration remains small is to calculate E using the bedload transport capacity concentration at equilibrium, c_{eq}. It is assumed that, at equilibrium, $E = D$ (Garcia and Parker, 1991), and therefore,

$$E = \alpha_d w_s c_{eq}, \quad D = \alpha_d w_s c, \tag{2.29}$$

where w_s is given by (2.25). For this empirical relationship, *i.e.* when E and D are used to describe bedload transport, α_d is defined as the ratio of the flow depth to the thickness of the bedload layer δ_b, (Cao *et al.*, 2010);

$$\alpha_d = \frac{h}{\delta_b}, \tag{2.30}$$

in which,

$$\delta_b = \begin{cases} 9\theta d & \text{if } \theta \geq {}^2/_9 \ , \\ 2d & \text{else,} \end{cases} \tag{2.31}$$

such that δ_b is a function of θ (e.g. Van Rijn, 1984a; Cao *et al.*, 2010), but the minimum bedload layer thickness is twice the particle diameter (Einstein, 1950). The equilibrium concentration of suspended sediment c_{eq} is the ratio of the local

flow discharge and bedload discharge (Van Rijn, 1984a), such that

$$c_{eq} = \frac{hu}{q_b} \ , \tag{2.32}$$

and the unit-width bedload discharge is calculated using the Meyer-Peter-Mueller formula; $q_b = \phi_e \sqrt{(s-1)gd^3}(\theta - \theta_c)^{3/2}$; where $\phi_e = 8$ (2.32) reduces to the original MPM formula proposed by Meyer-Peter and Müller (1948). The coefficient ϕ_e is employed so that the model can be easily extended to scenarios which differ from the uniform, steady flow conditions under which the MPM formula was derived. For example, $\phi_e > 8$ can be used under fast, transient flows, such as dam break flows, where sediment transport is expected to be more intense (Cao *et al.*, 2010). When $\phi_e = 4$, q_b is approximately equal to the variation described by Wong and Parker (2006), who showed that for horizontal beds with no bedforms, their modified MPM provided better agreement with laboratory-based data than the original formula presented by Meyer-Peter and Müller (1948). Othman *et al.* (2014) proposed several optimum ϕ_e values for modelling sediment transport in the swash zone based on a set of experimental measurements, and found ϕ_e was also a function of grain size. This method of calculating E and D is widely used but once again, the results are sensitive to the choice of bedload discharge formula.

Use of E and D, by definition, does not account for bedload transport in the traditional manner, because sediment is entrained into suspension. Instead local entrainment and deposition of particles, combined with appropriate closure relationships, (2.30) and (2.32), mimics the saltation of bedload particles; the choice of α_d in (2.30) results in a very large value of α_d, increasing the settling velocity in (2.29). Consequently, particles entrained into suspension are deposited quickly on the bed. This approach ensures that the depth-averaged concentration remains small. Following from (2.17), the density of the fluid is not significantly altered. As a result the flow hydrodynamics are not affected significantly by the presence of suspended sediment and are impacted solely by changes in bed morphology, as would be expected for bedload transport mechanisms.

For all test cases in this study, $\theta_c = 0.047$.

2.4.3 Determining the Dominant Transport Regime

The Rouse number, R_n, is used to determine whether the transport process is predominantly bedload or suspended sediment transport, or a combination of both. It is defined as

$$R_n = \frac{w_s}{\kappa u_f},$$

where w_s is the settling velocity of an individual sediment particle, $\kappa = 0.4$ is the von Kármán constant, and $u_f = \sqrt{\tau_b/\rho}$ is the shear (friction) velocity.

The dominant transport process is selected by implementing the condition (Soulsby, 1997, see, e.g.),

$$R_n \geq 2.5 \qquad \text{bedload only,}$$

$$1.2 \leq R_n < 2.5 \qquad \text{suspended sediment and bedload,}$$

$$\text{and,} \qquad R_n < 1.2 \qquad \text{suspended sediment only.}$$

The importance of using the Rouse number to obtain accurate results is demonstrated in Section 4.2.5.

The foregoing empirical formulae have been proposed for case-specific values of bed friction and resulting shear stress. Closure relationships are often derived from experimental data for cases of low shear stress (Cao *et al.*, 2004). For practical applications, a calibration study is necessary when selecting the appropriate formulations and corresponding empirical coefficients prior to applying the model.

2.5 Concluding Remarks

The depth-averaged shallow water-sediment equations have been derived; they include bedload and suspended sediment transport mechanisms, and bed morphological change. In deriving the above system of governing equations, it was

assumed that the vertical velocity was negligible and the pressure was hydrostatic. Under certain hydrodynamic conditions these assumptions are not valid. For example, during the initial seconds following a dam break, there is a strong vertical velocity and acceleration component, exacerbated by the presence of a mobile bed. It is important to remember this when interpreting the results of the numerical solver presented in the following chapters. Moreover, the shallow water equations are derived for smoothly varying bathymetries and small bed slopes. Caution must be exercised when analysing shallow flows on steep slopes or bed profiles which exhibit discontinuities. Closure relationships for sediment transport must be chosen carefully for each application; numerical results should always be interpreted with consideration for the physical conditions under which the empirical formulae chosen were developed. The numerical solver of (2.14) and (2.19) will now be presented.

Chapter 3

Finite Volume Numerical Model

3.1 Introduction

A Godunov-type finite volume HLLC scheme is used to solve (2.14) on a rectangular grid. The solver, which is second-order accurate in space, is conservative, and preserves shocks and discontinuities, such as those which occur in the free surface or velocity gradients following an abrupt dam breach. MUSCL-Hancock time integration, combined with a TVD slope limiter, is used to ensure the solution is second-order accurate in time. Before the equations can be solved using this scheme, they are written in conservative, hyperbolic, stage-discharge form. Fluxes are approximated at each side of each grid cell, at every time step. Boundary conditions are applied at the domain boundaries. The bed update equation (2.14e) is solved using a simple, second-order accurate finite difference scheme.

In a first instance, the HLLC Riemann solver will be presented for (2.14a) to (2.14d). It will be shown later how this solver is easily extended to the mathematically balanced form of the equations (2.19).

3.2 Hyperbolic Form of the Governing Equations

Equations (2.14a) to (2.14d) form a hyperbolic system of partial differential equations written as,

$$\frac{\partial \mathbf{q}}{\partial t} + \frac{\partial \mathbf{f}}{\partial x} + \frac{\partial \mathbf{g}}{\partial y} = \mathbf{s} \ , \tag{3.1}$$

where

$$\mathbf{q} = \begin{Bmatrix} \rho h \\ \rho u h \\ \rho v h \\ \rho_s c h \end{Bmatrix} \ , \ \mathbf{f} = \begin{Bmatrix} \rho u h \\ \rho u^2 h + \frac{1}{2}\rho g h^2 \\ \rho u v h \\ \rho_s c h u \end{Bmatrix} \ , \ \mathbf{g} = \begin{Bmatrix} \rho v h \\ \rho u v h \\ \rho v^2 h + \frac{1}{2}\rho g h^2 \\ \rho_s c h v \end{Bmatrix} \ ,$$

and

$$\mathbf{s} = \begin{Bmatrix} -\rho_0 \frac{\partial z_b}{\partial t} - \rho_s \frac{\partial q_{b_x}}{\partial x} - \rho_s \frac{\partial q_{b_y}}{\partial y} \\ -\rho_s \frac{\partial q_{b_x}}{\partial t} - \rho_s \frac{\partial}{\partial x}(u_{b_x} q_{b_x}) - \rho g h \frac{\partial z_b}{\partial x} - \tau_{b_x} \\ -\rho_s \frac{\partial q_{b_y}}{\partial t} - \rho_s \frac{\partial}{\partial y}(u_{b_y} q_{b_y}) - \rho g h \frac{\partial z_b}{\partial y} - \tau_{b_y} \\ -\rho_s (D - E) \end{Bmatrix} \ .$$

where the symbols have their usual meaning, as given in Chapter 2 and the Notation list.

Once written in hyperbolic form, the equations can now be solved using a Godunov-type scheme.

3.3 Godunov-Type Finite Volume Scheme

Finite volume schemes are more widely applicable, and in some scenarios more accurate, than their finite difference counterparts, because the equations are pre-

sented in conservative form, ensuring that the local numerical fluxes are conserved at each time step, across each of the grid cells. Unlike finite difference schemes, in which the differential form of the equations is maintained, the volume integral form of the conservation equations is employed in finite volume schemes, allowing shocks and discontinuities to be preserved. In the present work, a Godunov-type HLLC approximate Riemann solver is used to calculate values of the conserved variables at the centre of each grid point every time step.

The hyperbolic system of conservation laws given by (3.1) is expressed as a volume integral,

$$\frac{\partial}{\partial t}\int_{\Omega}\mathbf{q}\;d\Omega+\int_{\Omega}\frac{\partial\mathbf{f}}{\partial x}d\Omega+\int_{\Omega}\frac{\partial\mathbf{g}}{\partial y}d\Omega=\int_{\Omega}\mathbf{s}\;d\Omega. \tag{3.2}$$

In Cartesian form we can write the solution at the centre of each cell;

$$\mathbf{q}_{i,j}^{k+1}=\mathbf{q}_{i,j}^{k}-\frac{\Delta t}{\Delta x}(\mathbf{f}_{i+1/2,j}-\mathbf{f}_{i-1/2,j})-\frac{\Delta t}{\Delta y}(\mathbf{g}_{i,j+1/2}-\mathbf{g}_{i,j-1/2})+\Delta t\mathbf{s}_{i,j}, \tag{3.3}$$

where $\mathbf{f}_{i+1/2,j}$, $\mathbf{f}_{i-1/2,j}$, $\mathbf{g}_{i,j+1/2}$ and $\mathbf{g}_{i,j-1/2}$ are the flux vectors passing through the east, west, north and south faces of the cell, respectively. Δx and Δy are the cell dimensions in the x and y directions. $\mathbf{q}_{i,j}$ and $\mathbf{s}_{i,j}$ are the vectors of the dependent variables and source terms, respectively. The flux terms are evaluated at time step $k+\frac{1}{2}$ and source terms are evaluated at time step $k+1$, but the superscripts have been left out for simplicity.

3.4 Variable Density Riemann Problem

An HLLC (Harten-Lax-vanLeer-Contact) approximate Riemann solver (see e.g Fraccarollo and Toro, 1995) is used to solve (3.2). Toro *et al.* (1994b) gives a complete description of this scheme. The Riemann solver uses the linearised, approximate solution of the flux components, reducing the computational complexity of having to find the exact solution. One of the major advantages of the HLLC scheme, expanded from the earlier HLL (Harten *et al.*, 1983) Riemann

problem by Toro *et al.* (1994b), is that it can account for intermediate waves (S_* in Figure 3.1); examples include shear waves which arise in the case of 2D flow over a dry bed, or contact waves in the case of a discontinuity in the mixture (fluid) density. Figure 3.1 presents the four constant states separated by three waves, S_L, S_R, and S_*. The waves in Figure 3.1 are approximated as discontinuous waves but S_L and S_R could be replaced with rarefaction waves, depending on the physical problem.

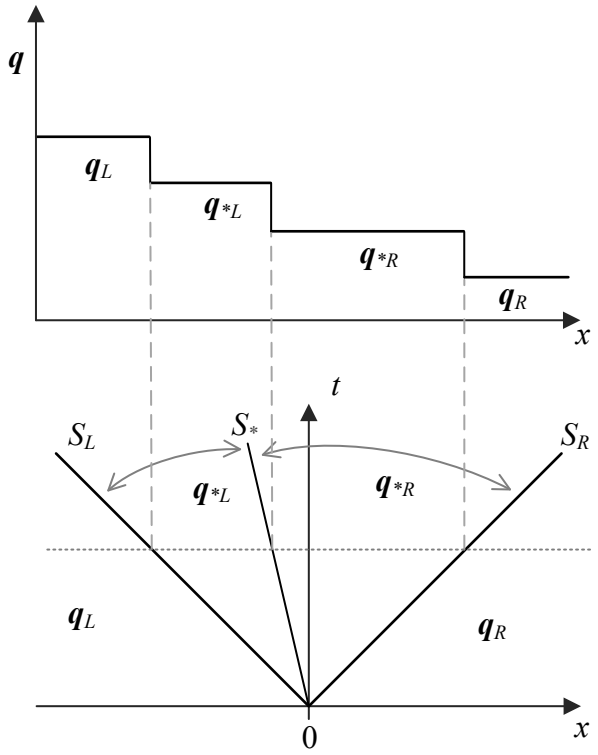

Figure 3.1: Wave structure of the HLLC Riemann problem (bottom) with S_L, S_* and S_R describing the wave speeds of the left, intermediate (middle) and right waves, separating four constant states (top) at time t.

By analysing the eigenstructure of the conventional shallow water equations, Fraccarollo and Toro (1995) showed that the normal velocity component and the water depth remain constant across the contact wave S_*; only the tangential velocity is discontinuous. It will be demonstrated herein that the property of constant normal velocity holds also across the contact and shear waves for the variable-density equations. However, across the contact wave associated with a discontinuity in mixture density, the water depth can vary, and is determined by the mixture density. Moreover, it will be shown that the density of the water-

sediment mixture is constant across rarefaction and shock waves. Similarly to Fraccarollo and Toro (1995) and Toro (2001), the solution to the Riemann problem is derived by determining the Jacobian matrix, eigenvalues, and eigenvectors of system (3.2), and then solving the Riemann invariants across the continuous waves, and the Rankine-Hugoniot conditions across the shock waves.

3.4.1 Eigenvalue Problem

The Jacobian matrix and the corresponding eigenstructure of the variable-density problem differ from the conventional shallow water problem and also from the formulation of the variable-density problem proposed by Cao *et al.* (2004), in which the variable-density term ρ is eliminated from the conserved variables of the water-sediment mixture mass and momentum equations, and redistributed to the source terms. The Jacobian matrix $\mathbf{C}$ is an extension of the 1D problem presented by Leighton *et al.* (2010), and is similar to the Jacobian matrix given by Murillo *et al.* (2012);

$$\mathbf{C} = \begin{bmatrix} 0 & \mathrm{n}_x & \mathrm{n}_y & 0 \\ (a^2 - u^2 + \alpha)\mathrm{n}_x - uv\mathrm{n}_y & 2u\mathrm{n}_x + v\mathrm{n}_y & u\mathrm{n}_y & -\beta\mathrm{n}_x \\ -uv\mathrm{n}_x + (a^2 - u^2 + \alpha)\mathrm{n}_y & v\mathrm{n}_x & u\mathrm{n}_x + 2v\mathrm{n}_y & -\beta\mathrm{n}_y \\ -\frac{\rho_s c}{\rho}(u\mathrm{n}_x + v\mathrm{n}_y) & \frac{\rho_s c}{\rho}\mathrm{n}_x & \frac{\rho_s c}{\rho}\mathrm{n}_y & u\mathrm{n}_x + v\mathrm{n}_y \end{bmatrix},$$

where the local dynamic wave velocity, $a = \sqrt{gh}$, n_x and n_y are unit vectors, and coefficients,

$$\alpha = \frac{(\rho_s - \rho_w)ca^2}{2\rho_w} \quad \text{and} \quad \beta = \frac{(\rho_s - \rho_w)\rho a^2}{2\rho_s\rho_w} \ .$$

The vector of eigenvalues of the combined system is found to be

$$\left\{ \begin{array}{c} \lambda_1 \\ \lambda_2 \\ \lambda_3 \\ \lambda_4 \end{array} \right\} = \left[\begin{array}{c} u\mathrm{n}_x + v\mathrm{n}_y - a \\ u\mathrm{n}_x + v\mathrm{n}_y \\ u\mathrm{n}_x + v\mathrm{n}_y + a \\ u\mathrm{n}_x + v\mathrm{n}_y \end{array} \right] . \tag{3.4}$$

Given that the 2D Riemann problem is treated as two 1D problems applied in the x and y directions, the solution across the rarefaction, shock, and shear waves shall be presented in the x direction only.

Letting n_x equal unity, the corresponding Jacobian, $\mathbf{A} = \mathbf{A}(\mathbf{q})$, of the *quasi-linear* system,

$$\mathbf{q}_t + \mathbf{A}(\mathbf{q})\mathbf{q}_x = \mathbf{s} \ , \tag{3.5}$$

is

$$\mathbf{A} = \left[\begin{array}{cccc} 0 & 1 & 0 & 0 \\ (a^2 - u^2 + \alpha) & 2u & 0 & -\beta \\ -uv & v & u & 0 \\ -\frac{\rho_s c}{\rho} u & \frac{\rho_s c}{\rho} & 0 & u \end{array} \right] ,$$

where $\mathbf{q}_t$ is the derivative of the matrix of conserved variables with respect to time t, $\mathbf{q}_x$ is the derivative of the matrix of conserved variables with respect to x and $\mathbf{s}_x$ is the matrix of source terms in the x direction. The the eigenvalues of Jacobian matrix $\mathbf{A}$ are

$$\left\{ \begin{array}{c} \lambda_1 \\ \lambda_2 \\ \lambda_3 \\ \lambda_4 \end{array} \right\} = \left[\begin{array}{c} u - a \\ u \\ u + a \\ u \end{array} \right] . \tag{3.6}$$

Vector (3.6) is similar to that of the constant-density 2D shallow-water problem but with a fourth eigenvalue, noting that the present variable-density problem is hyperbolic, but not strictly hyperbolic, since one of the eigenvalues has a multiplicity of 2; $\lambda_2 = \lambda_4 = u$.

The left and right eigenvectors of the Jacobian matrix, $\mathbf{A}(\mathbf{q})$, are

$$\mathbf{L} = \begin{bmatrix} u + a + \frac{(\rho_s - \rho_w)ac}{2\rho_w} & -1 & 0 & -\frac{(\rho_s - \rho_w)a\rho}{2\rho_s\rho_w} \\ -\frac{\rho_s(\rho_w - \rho)ac}{\rho_w\rho} & 0 & 0 & \frac{(\rho_w - \rho)a}{\rho_w} \\ 0 & 0 & 1 & 0 \\ a - u + \frac{(\rho_s - \rho_w)ac}{2\rho_w} & 1 & 0 & -\frac{(\rho_s - \rho_w)a\rho}{2\rho_s\rho_w} \end{bmatrix},$$

and

$$\mathbf{R} = \begin{bmatrix} 1 & 0 & 1 & \frac{\rho(\rho_s - \rho_w)}{\rho_s(\rho_w + \rho)} \\ u - a & 0 & u + a & u\frac{\rho(\rho_s - \rho_w)}{\rho_s(\rho_w + \rho)} \\ v & 1 & v & 0 \\ \frac{\rho_s c}{\rho} & 0 & \frac{\rho_s c}{\rho} & 1 \end{bmatrix}.$$

3.4.2 Properties of the HLLC Wave Structure

The Riemann problem is now solved in a similar way to the conventional shallow water problem (Toro, 2001) by considering the generalised Riemann invariants across the rarefaction and shear waves using the right eigenvector of the Jacobian matrix, and by analysing the Rankine-Hugoniot condition across the shock wave.

Rarefaction Waves

For a left rarefaction, consider the Riemann invariants of $\mathbf{R}^{(1)}$,

$$\frac{d\rho h}{1} = \frac{d\rho u h}{u - a} = \frac{d\rho v h}{v} = \frac{d\rho_s c h}{\rho_s c/\rho}. \tag{3.7}$$

Equating the first and fourth terms of (3.7) we find

$$\frac{d\rho h}{\rho} = \frac{dch}{c} \ . \tag{3.8}$$

This clearly shows that ρ = constant and c = constant, from the relationship between ρ and c, defined in (2.18).

Using (3.8), the first two equations of (3.7) reduce to the constant density problem such that

$$v = \text{constant}, \quad \text{and} \quad u - 2a = \text{constant}.$$

In summary, across a left rarefaction,

$$\rho = \text{constant}, \quad c = \text{constant}, \quad v = \text{constant}, \quad \text{and} \quad u - 2a = \text{constant}. \tag{3.9}$$

Similar considerations across the right rarefaction using $\mathbf{R}^{(3)}$ yield,

$$\rho = \text{constant}, \quad c = \text{constant}, \quad v = \text{constant}, \quad \text{and} \quad u + 2a = \text{constant}. \tag{3.10}$$

Shock Waves

For a shock wave, the Rankine-Hugoniot condition holds such that

$$\mathbf{f}(\mathbf{q}_{*L}) - \mathbf{f}(\mathbf{q}_L) = \mathbf{S}_L(\mathbf{q}_{*L} - \mathbf{q}_L) \quad \text{for a left shock wave,} \tag{3.11}$$

$$\mathbf{f}(\mathbf{q}_R) - \mathbf{f}(\mathbf{q}_{*R}) = \mathbf{S}_R(\mathbf{q}_R - \mathbf{q}_{*R}) \quad \text{for a right shock wave,} \tag{3.12}$$

where S_L and S_R are the speeds of the left and right shock waves respectively, and subscripts $L, *L, R$ and $*R$ denote the states of the Riemann problem as shown in Figure 3.1.

Considering a left shock wave, the conserved variables to the left of the star

(or middle) wave, q_{*L}, and to the left of the shock wave, q_L are

$$\mathbf{q}_{*L} = \left\{ \begin{array}{c} \rho_{*L} h_{*L} \\ \rho_{*L} u_{*L} h_{*L} \\ \rho_{*L} v_{*L} h_{*L} \\ \rho_s c_{*L} h_{*L} \end{array} \right\} \qquad \text{and} \qquad \mathbf{q}_L = \left\{ \begin{array}{c} \rho_L h_L \\ \rho_L u_L h_L \\ \rho_L v_L h_L \\ \rho_s c_L h_L \end{array} \right\},$$

and the corresponding flux matrices are

$$\mathbf{f}(\mathbf{q}_{*L}) = \left[\begin{array}{c} \rho_{*L} u_{*L} h_{*L} \\ \rho_{*L} u_{*L}^2 h_{*L} + \frac{1}{2} \rho_{*L} g h_{*L}^2 \\ \rho_{*L} u_{*L} v_{*L} h_{*L} \\ \rho_s c_{*L} u_{*L} h_{*L} \end{array} \right] \quad \text{and} \quad \mathbf{f}(\mathbf{q}_L) = \left[\begin{array}{c} \rho_L u_L h_L \\ \rho_L u_L^2 h_L + \frac{1}{2} \rho_L g h_L^2 \\ \rho_L u_L v_L h_L \\ \rho_s c_L u_L h_L \end{array} \right].$$

The Rankine-Hugoniot conditions for the first two equations of (3.11) are

$$\rho_{*L} u_{*L} h_{*L} - \rho_L u_L h_L = S_L (\rho_{*L} h_{*L} - \rho_L h_L), \tag{3.13}$$

$$\text{and,} \quad \rho_{*L} u_{*L}^2 h_{*L} + \frac{1}{2} \rho_{*L} g h_{*L}^2 - (\rho_L u_L^2 h_L + \frac{1}{2} \rho_L g h_L^2) = S_L (\rho_{*L} u_{*L} h_{*L} - \rho_L u_L h_L) \ . \tag{3.14}$$

Following Toro (2001), to facilitate the use of the Rankine-Hugoniot conditions, the frame of reference of the problem described by (3.11) is transformed to that moving with the speed of the shock wave, S_L. The relative velocities, $\hat{u}$, are:

$$\hat{u}_L = u_L - S_L, \quad \text{and,} \quad \hat{u}_{*L} = u_{*L} - S_L. \tag{3.15}$$

Substituting (3.15) into (3.13) and (3.14), the RH conditions can be written in

the transformed frame of reference as,

$$\rho_{*L}\hat{u}_{*L}h_{*L} = \rho_L\hat{u}_L h_L \ , \tag{3.16}$$

$$\text{and,} \qquad \rho_{*L}u_{*L}^2 h_{*L} + \frac{1}{2}\rho_{*L}gh_{*L}^2 = \rho_L u_L^2 h_L + \frac{1}{2}\rho_L g h_L^2 \ . \tag{3.17}$$

Similarly, substitution of (3.15) into the third and fourth equations of (3.11) yields,

$$\rho_{*L}\hat{u}_{*L}\hat{v}_{*L}h_{*L} = \rho_L\hat{v}_L\hat{u}_L h_L \ , \tag{3.18}$$

$$\text{and,} \qquad c_{*L}\hat{u}_{*L}h_{*L} = c_L\hat{u}_L h_L \ . \tag{3.19}$$

Dividing (3.18) by (3.16) confirms that the tangential velocity across a shock wave is constant, as expected following from the constant-density problem, i.e.,

$$\hat{v}_{*L} = \hat{v}_L \ , \tag{3.20}$$

Rewriting (3.16) and substituting it into (3.19) we can write

$$\frac{\rho_L}{c_L} = \frac{\rho_{*L}}{c_{*L}} \ . \tag{3.21}$$

Combining the relationship between ρ and c, given by (2.18), with (3.21), dividing both sides by $(\rho_s - \rho_w)$, and rearranging, we obtain

$$\rho_L = \rho_{*L} \ , \tag{3.22}$$

i.e. the density of the water-sediment mixture is preserved across the shock wave.

This mathematical derivation demonstrates consistency with the physical assumption made when deriving the governing equations; that the suspended sed-

iment particles are carried at the same speed as the water particles. Thus, the presence of sediment does not impact the properties of the flow velocity and water depth across shock waves and rarefaction waves.

Similar analysis can be performed across a right shock wave to yield the same results; $v_{*R} = v_R$, $c_{*R} = c_R$ and $\rho_{*R} = \rho_R$.

In summary, across a shock wave,

$$\rho_{*L} = \rho_L \ , \qquad \rho_{*R} = \rho_R \ , \tag{3.23}$$

$$c_{*L} = c_L \ , \qquad c_{*R} = c_R \ , \tag{3.24}$$

$$\text{and,} \qquad v_{*L} = v_L \ , \qquad v_{*R} = v_R \ . \tag{3.25}$$

Shear Waves

The Riemann invariants across the shear waves associated with a 2D dry bed contact discontinuity and a density discontinuity are $\mathbf{R^{(2)}}$ and $\mathbf{R^{(4)}}$, respectively. It is easily shown that the Riemann invariants across $\mathbf{R^{(2)}}$ yield similar results to the constant density problem;

$$\rho h = \text{constant}, \quad u = \text{constant}, \quad v \neq \text{constant}. \tag{3.26}$$

Across the contact wave associated with a density discontinuity, the Riemann invariants give

$$\frac{\rho_s(\rho_w + \rho)d\rho h}{\rho(\rho_s - \rho_w)} = \frac{\rho_s(\rho_w + \rho)d\rho uh}{u\rho(\rho_s - \rho_w)} = \frac{d\rho_s h}{1}. \tag{3.27}$$

Equating the first two terms and dividing by $\frac{\rho_s(\rho_w+\rho)}{\rho(\rho_s-\rho_w)}$, it is straightforward to show that $u =$ constant. Now, equating the first and last terms, and substituting $c = \frac{\rho-\rho_w}{\rho_s-\rho_w}$, after some simple manipulation we can write,

$$2\rho dh + h d\rho = 0, \tag{3.28}$$

or, multiplying both sides by h and integrating,

$$\rho h^2 = \text{constant}, \tag{3.29}$$

in agreement with the hydrostatic pressure assumption made in the initial derivation of the shallow water-sediment equations. Note here that if the bathymetry is variable, the change in bed elevation needs to be incorporated in the pressure term such that $\rho(h^2 - z_b^2) = \text{constant}$. The eigenvector element of ρvh is zero, i.e. there is no variation in ρvh, thus $v = \text{constant}$.

In summary, across a contact discontinuity, the following properties are defined;

$$u_{*L} = u_{*R} = S_* \ , \tag{3.30}$$

$$\rho_{*L} h_{*L} = \rho_{*R} h_{*R} = \rho_* h_* \quad \text{for } \mathbf{R^{(2)}}, \tag{3.31}$$

$$\rho_{*L} h_{*L}^2 = \rho_{*R} h_{*R}^2 = \rho_* h_*^2 \quad \text{for } \mathbf{R^{(4)}}, \tag{3.32}$$

$$v_{*L} \neq v_{*R} \quad \text{for } \mathbf{R^{(2)}}, \tag{3.33}$$

$$\text{and,} \qquad v_{*L} = v_{*R} \quad \text{for } \mathbf{R^{(4)}}. \tag{3.34}$$

From (3.32), it is clear that the depth of the fluid must change across a contact discontinuity associated with a jump in fluid density. This will be verified numerically in Sections 4.2.1 and 4.2.5. The properties defined in (3.9) to (3.34) are now used to solve approximately the Riemann problem using the HLLC approach, similar to Toro (2001).

3.4.3 HLLC Riemann Solver

Letting $u_* = S_*$, the Rankine-Hugoniot condition across the left and right shock waves gives,

$$(\rho h^2)_{*L} = -\frac{\rho_L h_L^2 (S_L - u_L)}{(S_* - S_L)} \ , \tag{3.35}$$

and,

$$(\rho h^2)_{*R} = -\frac{\rho_R h_R^2 (S_R - u_R)}{(S_* - S_R)} \ . \tag{3.36}$$

Following from condition (3.32), equating (3.35) and (3.36) such that,

$$\rho_R h_R^2 (S_R - u_R)(S_* - S_R) = \rho_L h_L^2 (S_L - u_L)(S_* - S_R) \ , \tag{3.37}$$

the equation for the middle wave speed S_* is obtained;

$$S_* = \frac{S_L \rho_R h_R^2 (S_R - u_R) - S_R \rho_L h_L^2 (S_L - u_L)}{\rho_R h_R^2 (S_R - u_R) - \rho_L h_L^2 (S_L - u_L)} \ . \tag{3.38}$$

This is very similar to the solution for S_* obtained from the classical shallow-water equations presented by Toro (2001). The main difference is that here, the variable depth-integrated mass of the water-sediment mixture, ρh, must be incorporated when calculating S_*. Equation (3.38) is a generalised form of the equation given by Toro (2001). When ρ is constant in space and time, (3.38) reduces exactly to the equation for S_* proposed by Toro (2001). For the examples considered herein, a similar result is obtained when using either (3.38) or the equation for the middle wave given by Toro (2001). However, the results could be expected to differ for a highly concentrated bore of water-sediment mixture flowing into a region of clear water, such as a mud flow entering a lake or a tsunami front in the form of a broken wave.

The approximate solution to the numerical flux, $\mathbf{f}_{i+\frac{1}{2}}$, at the interface between two adjacent grid cells can now be calculated as

$$\mathbf{f}_{i+\frac{1}{2},\,j} = \begin{cases} \mathbf{f}_L & \text{if} \quad 0 \leq S_L \\ \mathbf{f}_{*L} & \text{if} \quad S_L \leq 0 \leq S_* \\ \mathbf{f}_{*R} & \text{if} \quad S_* \leq 0 \leq S_R \\ \mathbf{f}_R & \text{if} \quad 0 \geq S_R \end{cases},$$

where $\mathbf{f}_L = \mathbf{f}(\mathbf{q}_L)$ and $\mathbf{f}_R = \mathbf{f}(\mathbf{q}_R)$ are calculated from the left and right Riemann states, $\mathbf{q}_L$ and $\mathbf{q}_R$, respectively. The fluxes to the left and right of the contact wave, $\mathbf{f}_{*L}$ and $\mathbf{f}_{*R}$, are given by

$$\mathbf{f}_{*L} = \begin{bmatrix} f_{*1} \\ f_{*2} \\ v_L f_{*1} \\ \frac{\rho_s c_L}{\rho_L} f_{*1} \end{bmatrix} \quad \text{and} \quad \mathbf{f}_{*R} = \begin{bmatrix} f_{*1} \\ f_{*2} \\ v_R f_{*1} \\ \frac{\rho_s c_R}{\rho_R} f_{*1} \end{bmatrix},$$

where the fluxes, f_{*1} and f_{*2} are the HLL flux components calculated using the vector equation (Harten *et al.* (1983))

$$\mathbf{f}_* = \frac{S_R \mathbf{f}_L - S_L \mathbf{f}_R + S_L S_R (\mathbf{q}_R - \mathbf{q}_L)}{S_R - S_L}.$$

Values of the left and right wave speeds for the two-wave Riemann problem, S_L and S_R, are estimated following Fraccarollo and Toro (1995) as:

$$S_L = \begin{cases} u_R - 2\sqrt{g h_R} & \text{if} \quad h_L = 0 \\ \min(u_L - \sqrt{g h_L}, u_* - \sqrt{g h_*}) & \text{if} \quad h_L > 0 \end{cases},$$

and

$$S_R = \begin{cases} u_L + 2\sqrt{gh_L} & \text{if} \quad h_R = 0 \\ \max(u_R + \sqrt{gh_R}, u_* + \sqrt{gh_*}) & \text{if} \quad h_R > 0 \end{cases} ,$$

where u_L, u_R, h_L and h_R are the left and right constant Riemann states, and the velocity and water depth in the star region, u_* and h_* are given by

$$u_* = \frac{1}{2}(u_L + u_R) + \sqrt{gh_L} - \sqrt{gh_R} \ , \tag{3.39}$$

and,

$$h_* = \frac{1}{g}\left[\frac{1}{2}(\sqrt{gh_L} + \sqrt{gh_R}) + \frac{1}{4}(u_L - u_R)\right]^2 . \tag{3.40}$$

3.5 MUSCL-Hancock Scheme

Godunov-type schemes, such as the HLLC approximate Riemann solver used in the present work, are at most first-order accurate in time (Godunov, 1959). The MUSCL-Hancock method is a predictor-corrector approach used to ensure second-order accuracy, which was first presented by van Leer (1985), although the name was first coined by Toro (1999). This method includes three main steps (i) reconstruction of cell-centred data, (ii) evolution of the reconstructed data in time and (iii) solution of the Riemann problem.

The first step (predictor) estimates values of the conserved variables of cell (*i,j*) at the cell interfaces using interpolation. The cell interface fluxes are calculated with the reconstructed variables and used to advance the solution of the cell-centred variables in time by half a time step, $\frac{\Delta t}{2}$ using the formula (shown for conserved variable in x direction only),

$$\mathbf{q}^{k+\frac{1}{2}}_{i+\frac{1}{2},j} = \mathbf{q}^{k}_{i+\frac{1}{2},j} - \frac{\Delta t}{2\Delta x}\Big(\mathbf{f}(\mathbf{q}_{i+\frac{1}{2},j}) - \mathbf{f}(\mathbf{q}_{i-\frac{1}{2},j})\Big) \tag{3.41a}$$

$$- \frac{\Delta t}{2\Delta y}\Big(\mathbf{g}(\mathbf{q}_{i,j+\frac{1}{2}}) - \mathbf{g}(\mathbf{q}_{i,j-\frac{1}{2}})\Big) + \frac{\Delta t}{2}\mathbf{s}_{i,j}, \tag{3.41b}$$

$$\text{and,} \quad \mathbf{q}^{k+\frac{1}{2}}_{i-\frac{1}{2},j} = \mathbf{q}^{k}_{i-\frac{1}{2},j} - \frac{\Delta t}{2\Delta x}\Big(\mathbf{f}(\mathbf{q}_{i+\frac{1}{2},j}) - \mathbf{f}(\mathbf{q}_{i-\frac{1}{2},j})\Big) \tag{3.41c}$$

$$- \frac{\Delta t}{2\Delta y}\Big(\mathbf{g}(\mathbf{q}_{i,j+\frac{1}{2}}) - \mathbf{g}(\mathbf{q}_{i,j-\frac{1}{2}})\Big) + \frac{\Delta t}{2}\mathbf{s}_{i,j}. \tag{3.41d}$$

Equation (3.41) is also applied in the y direction to update $\mathbf{q}^{k+\frac{1}{2}}_{i,j+\frac{1}{2}}$ and $\mathbf{q}^{k+\frac{1}{2}}_{i,j-\frac{1}{2}}$. The updated cell interface fluxes, for example, $\mathbf{f}^{k+\frac{1}{2}}_{i+\frac{1}{2},j} = \mathbf{f}\big(\mathbf{q}^{k+\frac{1}{2}}_{i+\frac{1}{2},j}\big)$, are then used to find the solution of the Riemann problem using (3.3), advancing the solution over the full time step, Δt.

It is well known that high order schemes can produce spurious oscillations in regions of steep gradients. To contain the solution and avoid numerical oscillations, a total variation diminishing (TVD) slope limiter, $\Phi(\mathbf{r})$, is applied when interpolating the cell interface values, such that

$$\mathbf{q}_e^{k+\frac{1}{2}}(i,j) = \mathbf{q}_{i,j}^{k+\frac{1}{2}} + \frac{1}{2}\Phi(\mathbf{r})(\mathbf{q}^k_{i,j} - \mathbf{q}^k_{i-1,j}), \tag{3.42a}$$

$$\mathbf{q}_w^{k+\frac{1}{2}}(i,j) = \mathbf{q}_{i,j}^{k+\frac{1}{2}} - \frac{1}{2}\Phi(\mathbf{r})(\mathbf{q}^k_{i,j} - \mathbf{q}^k_{i-1,j}), \tag{3.42b}$$

$$\mathbf{q}_n^{k+\frac{1}{2}}(i,j) = \mathbf{q}_{i,j}^{k+\frac{1}{2}} + \frac{1}{2}\Phi(\mathbf{r})(\mathbf{q}^k_{i,j} - \mathbf{q}^k_{i,j-1}), \tag{3.42c}$$

$$\text{and,} \quad \mathbf{q}_s^{k+\frac{1}{2}}(i,j) = \mathbf{q}_{i,j}^{k+\frac{1}{2}} - \frac{1}{2}\Phi(\mathbf{r})\mathbf{r}(\mathbf{q}^k_{i,j} - \mathbf{q}^k_{i,j-1}), \tag{3.42d}$$

where subscripts e, w, n, s represent the east, west, north, and south faces of cell

(i, j), and $\mathbf{r}$ is the ratio of consecutive gradients given by

$$\mathbf{r} = \begin{cases} \frac{\mathbf{q}_{i+1,j} - \mathbf{q}_{i,j}}{\mathbf{q}_{i,j} - \mathbf{q}_{i-1,j}} & \text{if} \quad \mathbf{q}_{i,j} \neq \mathbf{q}_{i-1,j} \\ 0 & \text{if} \quad \mathbf{q}_{i,j} = \mathbf{q}_{i-1,j} \end{cases}, \tag{3.43}$$

for calculating $\mathbf{q}_e$ and $\mathbf{q}_w$ in the x direction, and

$$\mathbf{r} = \begin{cases} \frac{\mathbf{q}_{i,j+1} - \mathbf{q}_{i,j}}{\mathbf{q}_{i,j} - \mathbf{q}_{i,j-1}} & \text{if} \quad \mathbf{q}_{i,j} \neq \mathbf{q}_{i,j-1} \\ 0 & \text{if} \quad \mathbf{q}_{i,j} = \mathbf{q}_{i,j-1}, \end{cases}, \tag{3.44}$$

for updating $\mathbf{q}_n$ and $\mathbf{q}_s$ in the y direction.

The slope limiter is evaluated using a well-tested formula suggested by Sweby (1984);

$$\Phi(\mathbf{r}) = \max[0, \min(\beta\mathbf{r}, 1), \min(\mathbf{r}, \beta)], \tag{3.45}$$

where $\Phi(\mathbf{r})$ is the MINIMOD limiter when β is equal to 1 and the SUPERBEE limiter when β is taken to be 2.

3.6 HLLC Riemann Solver for Balanced Stage-Discharge Equations

Rogers *et al.* (2003) showed that the Jacobian matrix and the eigenstructure of the balanced shallow water equations (2.19) are the same as the unbalanced equations for the constant density case. For the variable density equations presented here, the Jacobian matrix of (2.19) is not identical to that of (2.14). However, because balancing does not change the wave speeds of the physical variables, here we assume that the eigenvalues of system (2.19) are the same as those of (2.14). As a result, the wave speeds derived in this chapter are retained in the HLLC solver of

the balanced equations (2.19). The the hyperbolic system for the mathematically balanced equations, (2.19a) to (2.19d), is given by,

$$\frac{\partial \mathbf{q}}{\partial t} + \frac{\partial \mathbf{f}}{\partial x} + \frac{\partial \mathbf{g}}{\partial y} = \mathbf{s} \ , \tag{3.46}$$

where,

$$\mathbf{q} = \begin{Bmatrix} \rho\eta \\ \rho uh \\ \rho vh \\ \rho_s hc \end{Bmatrix} \ , \ \mathbf{f} = \begin{Bmatrix} \rho uh \\ \rho u^2 h + \frac{1}{2}g(\eta^2 - 2\eta z_b) \\ \rho uvh \\ \rho_s huc \end{Bmatrix} \ , \ \mathbf{g} = \begin{Bmatrix} \rho vh \\ \rho uvh \\ \rho v^2 h + \frac{1}{2}g(\eta^2 - 2\eta z_b) \\ \rho_s hvc \end{Bmatrix} \ ,$$

and

$$\mathbf{s} = \begin{Bmatrix} -\rho_0 \frac{\partial z_b}{\partial t} - \rho_s \frac{\partial q_{b_x}}{\partial x} - \rho_s \frac{\partial q_{b_y}}{\partial y} + \frac{\partial(\rho z_b)}{\partial t} \\ -\rho_s \frac{\partial q_{b_x}}{\partial t} - \rho_s \frac{\partial}{\partial x}(u_{b_x} q_{b_x}) - \rho g\eta \frac{\partial z_b}{\partial x} + \frac{1}{2} g {z_b}^2 \frac{\partial \rho}{\partial x} - \tau_{b_x} \\ -\rho_s \frac{\partial q_{b_y}}{\partial t} - \rho_s \frac{\partial}{\partial y}(u_{b_y} q_{b_y}) - \rho g\eta \frac{\partial z_b}{\partial y} + \frac{1}{2} g {z_b}^2 \frac{\partial \rho}{\partial y} - \tau_{b_y} \\ -\rho_s(D - E) \end{Bmatrix} .$$

The validity of this assumption is investigated in Section 4.2.5.

3.7 Convenient Form of the Governing Equations

To facilitate the numerical scheme and solve (2.19) (or (3.46)) simultaneously each time step, the dependent variables, ρ, η (or h when system (2.14) is used), c, u and v in (2.19a)-(2.19d) are substituted for by new variables, M, p_x, p_y, and M_S, following the approach of Apostolidou (2011). Let,

$$M = \rho\eta, \quad p_x = \rho uh, \quad p_y = \rho vh, \text{ and } \quad M_S = \rho_s ch, \tag{3.47}$$

where M incorporates the mass of the water-sediment mixture, p_x and p_y are momenta of the water-sediment mixture in the x and y directions, and M_S is the depth-integrated mass of suspended sediment.

Substituting for the above variables, (2.19a)-(2.19d) can be rewritten as

$$\frac{\partial M}{\partial t} + \frac{\partial p_x}{\partial x} + \frac{\partial p_y}{\partial y} = -\rho_0 \frac{\partial z_b}{\partial t} - \rho_s \frac{\partial q_{b_x}}{\partial x} - \rho_s \frac{\partial q_{b_y}}{\partial y} + \frac{\partial \rho z_b}{\partial t}, \tag{3.48a}$$

$$\begin{aligned} &\frac{\partial p_x}{\partial t} + \frac{\partial}{\partial x}\Big(p_x u + \frac{1}{2} g \frac{M^2}{\rho} - g z_b M\Big) + \frac{\partial p_x v}{\partial y} \\ &\qquad = -\rho_s \frac{\partial q_{b_x}}{\partial t} - \rho_s \frac{\partial}{\partial x}(u_{b_x} q_{b_x}) - \rho g \eta \frac{\partial z_b}{\partial x} + \frac{1}{2} g {z_b}^2 \frac{\partial \rho}{\partial x} - \tau_{b_x}, \end{aligned} \tag{3.48b}$$

$$\begin{aligned} &\frac{\partial p_y}{\partial t} + \frac{\partial}{\partial y}\Big(p_y v + \frac{1}{2} g \frac{M^2}{\rho} - g z_b M\Big) + \frac{\partial p_y u}{\partial x} \\ &\qquad = -\rho_s \frac{\partial q_{b_y}}{\partial t} - \rho_s \frac{\partial}{\partial y}(u_{b_y} q_{b_y}) - \rho g \eta \frac{\partial z_b}{\partial y} + \frac{1}{2} g {z_b}^2 \frac{\partial \rho}{\partial y} - \tau_{b_y}. \end{aligned} \tag{3.48c}$$

and

$$\frac{\partial M_S}{\partial t} = -\frac{\partial M_S u}{\partial x} - \frac{\partial M_S v}{\partial y} - \rho_s (D - E), \tag{3.48d}$$

The components of the hyperbolic system (3.46) are now given by,

$$\mathbf{q} = \begin{Bmatrix} M \\ p_x \\ p_y \\ M_S \end{Bmatrix}, \ \mathbf{f} = \begin{Bmatrix} p_x \\ p_x u + \frac{1}{2} g \frac{M^2}{\rho} - g z_b M \\ p_y u \\ M_S u \end{Bmatrix}, \ \mathbf{g} = \begin{Bmatrix} p_y \\ p_x v \\ p_y v + \frac{1}{2} g \frac{M^2}{\rho} - g z_b M \\ M_S v \end{Bmatrix},$$

and

$$\mathbf{s} = \begin{Bmatrix} -\rho_0 \frac{\partial z_b}{\partial t} - \rho_s \frac{\partial q_{b_x}}{\partial x} - \rho_s \frac{\partial q_{b_y}}{\partial y} + \frac{\partial(\rho z_b)}{\partial t} \\ -\rho_s \frac{\partial q_{b_x}}{\partial t} - \rho_s \frac{\partial}{\partial x}(u_{b_x} q_{b_x}) - \rho g \eta \frac{\partial z_b}{\partial x} + \frac{1}{2} g {z_b}^2 \frac{\partial \rho}{\partial x} - \tau_{b_x} \\ -\rho_s \frac{\partial q_{b_y}}{\partial t} - \rho_s \frac{\partial}{\partial y}(u_{b_y} q_{b_y}) - \rho g \eta \frac{\partial z_b}{\partial y} + \frac{1}{2} g {z_b}^2 \frac{\partial \rho}{\partial y} - \tau_{b_y} \\ -\rho_s (D - E) \end{Bmatrix}.$$

The problem is solved at each time step using the numerical method described previously in this chapter above. The relationships defined in (3.47) are then used to find updated values of the conserved variables; η, ρ, u, v and c.

3.8 Discretisation of Source Terms and Bed Update Equation

Unlike the four equations of system (3.1) solved above, in its general form, the bed morphological equation (2.14e) is not a traditional advection equation. Several researchers (see e.g. Hudson and Sweby, 2003; Murillo and García-Navarro, 2010; Benkhaldoun *et al.*, 2013; Briganti *et al.*, 2012) have solved (2.14e) using finite volumes by including it in the above eigenvalue problem. However, a straightforward extension of the eigenvalue problem is possible only for subcritical and supercritical flows when the Grass bedload formula is used to estimate the bedload discharge. To ensure that the model can be extended and applied to a wider range of physical scenarios while avoiding additional computational effort (as required by Murillo and García-Navarro, 2010, for example), here the bed morphological equation (2.14e) is calculated using second-order central differences. The system of equations is still defined as a fully coupled model because the bed morphological equation and (3.1) or (3.46) are simultaneously updated at each time step.

The source terms are evaluated at the centre of the grid cells, also using second-order accurate central differences. After mathematical balancing, in the

equation of conservation of mass of water-sediment mixture, (2.19a) is written,

$$\frac{\partial \rho \eta}{\partial t} + \frac{\partial \rho u h}{\partial x} + \frac{\partial \rho v h}{\partial y} = -\rho_0 \frac{\partial z_b}{\partial t} - \rho_s \frac{\partial q_{b_x}}{\partial x} - \rho_s \frac{\partial q_{b_y}}{\partial y} + \frac{\partial \rho z_b}{\partial t} \ .$$

The partial derivative of the last term on the right hand side, $\frac{\partial \rho z_b}{\partial t}$, cannot be solved for explicitly using the finite difference scheme. A simple iterative method is adopted for this term.

Verification and validation tests (see Chapter 4 and Chapter 5) will show that the second-order central difference scheme is an acceptably accurate method for updating the source terms and the bed update equation for the engineering applications considered here.

3.9 Numerical Stability

The stability of the present numerical scheme is determined using the Courant-Friedrichs-Lewy (CFL) number, C_{cfl}. The minimum appropriate time step, Δt, is estimated using the formula (see, e.g. Fraccarollo and Toro, 1995),

$$\Delta t = \min\Big(\frac{C_{cfl}\Delta x}{\sqrt{gh}+u}, \frac{C_{cfl}\Delta y}{\sqrt{gh}+v}\Big) \ , \tag{3.49}$$

where Δx and Δy are the dimensions of the grid cell, u and v are the velocity components in the x and y directions, respectively, g is acceleration due to gravity and h is the water depth at the centre of the grid cell. The numerical scheme remains stable when the CFL condition satisfies

$$0 < C_{cfl} \leq 1.$$

Grid and time step convergence tests have been carried out for every test case to obtain a sensible balance between accuracy and computational efficiency.

3.10 Boundary Conditions

In the majority of the cases presented in this work, two simple boundary conditions are applied: closed, slip conditions; or open, transmissive conditions. Slip conditions represent a frictionless, reflective solid boundary where the velocity normal to the wall is zero and the tangential flow along the wall is unrestrained. For a solid boundary is running in the x direction,

$$M_B^{k+1} = M_I^{k+1}, \quad p_{xB}^{k+1} = 0, \quad p_{yB}^{k+1} = p_{yI}^{k+1}, \tag{3.50}$$

$$M_{S_B}^{k+1} = M_{S_I}^{k+1}, \quad z_{bB}^{k+1} = z_{bI}^{k+1},$$

where B represents the cell outside the domain boundary, I is the cell inside the domain boundary and k is the k^{th} timestep. A similar condition is applied to a boundary running in the y direction except that,

$$p_{xB}^{k+1} = p_{xI}^{k+1}, \quad \text{and} \quad p_{yB}^{k+1} = 0\ . \tag{3.51}$$

Transmissive, or open, boundary conditions are applied to allow inflow to and outflow from the domain.

$$M_B^{k+1} = M_I^{k+1}, \quad p_{xB}^{k+1} = p_{xI}^{k+1}, \quad p_{yB}^{k+1} = p_{yI}^{k+1}, \tag{3.52}$$

$$M_{S_B}^{k+1} = M_{S_I}^{k+1}, \quad z_{bB}^{k+1} = z_{bI}^{k+1}.$$

In some of the test cases in Chapter 4 and Chapter 5, the discharge is prescribed at the inflow or outflow;

$$p_{xB}^{k+1} = p_{xB}^{k}. \tag{3.53}$$

3.11 Conclusion

A robust, finite volume numerical scheme has been presented to solve the shallow water-sediment equations. An updated solution has been derived for the speed of the middle wave of the HLLC Riemann problem, to include the depth-averaged variable density of the water-sediment mixture. This is a general form of the equation given by Toro (2001), and reduces exactly to Toro's equation when the density of the mixture is constant. It has been demonstrated that the properties of the water depth and flow velocities are not altered across shock and rarefaction waves when sediment is present in suspension. However, it has been shown that the water depth is discontinuous across a contact wave associated with a density discontinuity, with the square of the water depth directly proportional to the mixture density.

A detailed solution of the Riemann problem has been presented for the water depth-discharge ($h - q$) form of the equations. It will be shown in the following chapters that the wave speeds of this problem remain unchanged for the mathematically balanced equations, written in free surface elevation-discharge form ($\eta - q$), allowing the solution presented in this chapter to be used to solve the well-balanced governing equations.

In the numerical solver described above, no specific wetting and drying algorithm has been used. As will be demonstrated in Chapter 4, the numerical model described above is able to simulate flow over an initially dry, frictionless, horizontal bed. For a sloping bed or a rough bed (i.e. bed with friction slope), the numerical model is not valid for flow over an initially dry bed. To account for this, the dry-bed is modelled by including a very small layer of water in the initially dry section of the domain, $\approx 10^{-6}$m (see Chapter 5). It is important to note, however, that this method is only approximately valid for modelling flow over a fixed bed. In the absence of a wetting and drying algorithm, the numerical solver cannot be used to model intense sediment transport over an almost dry bed, such as a dam break over an initially dry bed.

The numerical solver will now be verified and validated extensively in Chapter 4 and Chapter 5.

Chapter 4

Model Performance Verification Tests

To ensure the present scheme is accurate and reliable, the numerical model is verified against a variety of well-established test cases with analytical and semi-analytical solutions, and numerical predictions from high resolution models (e.g. Toro, 2001). These tests are used to verify that mass and momentum are conserved, and that the implemented boundary conditions accurately represent the physics of the surrounding environment. The tests were chosen carefully to verify complex hydrodynamic scenarios over a fixed bed, and the interaction of the steady flow and sediment transport over a mobile bed. In all of the following test cases the pressure is hydrostatic, the vertical motion is negligible, and all waves are assumed to be long with small amplitude.

4.1 Clear Water Test Cases

If the initial density of the water-sediment mixture is constant, in the absence of sediment transport, the governing equations (2.19) reduce to the constant density shallow-water equations. The following test cases are used to verify the ability of the numerical scheme to simulate constant density flows, including, steady flow over a fixed bed hump, a frictionless rectangular dam breach, one dimensional bores and rarefactions, and a circular dam break.

4.1.1 Case 1: Steady Flow over a Fixed Hump

This test case considers one-dimensional steady flow over a fixed hump in a channel 25 m long and 1 m wide. It is a widely used benchmark test problem for numerical methods which simulate dam break flows, because it tests the scheme's ability to model supercritical flow and hydraulic jumps (see e.g. García-Navarro *et al.*, 1992; Zhou *et al.*, 2001; Ying and Wang, 2008). The rectangular channel has a horizontal, frictionless bed, except for a single hump. The bed profile (in m) is defined by

$$z_b(x,t) = \begin{cases} 0.2 - 0.05(x-10)^2 & \text{if} \quad 8 \leq x \leq 12 \ , \\ 0.0 & \text{otherwise.} \end{cases}$$

where x is the distance downstream from the inlet and all the above values are given in m. At the downstream boundary, the free surface elevation, η, is fixed at 0.33 m and the discharge is free to vary. At the inflow, a transmissive condition is used for the free surface elevation and the discharge is fixed such that $q_x = 0.18$ m^{2}s^{-1}.

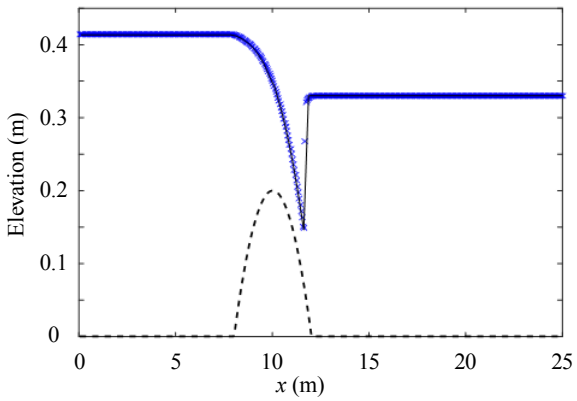

Figure 4.1: Formation of a hydraulic jump in steady flow over a bed hump; analytical solution (solid line) and numerical results (blue x) of free surface elevation, η (m). Bed elevation, z_b (m), shown as dashed line.

Grid convergence was carried out to determine the optimum mesh size to ensure accuracy and computational efficiency. The computational domain is mapped on a uniform grid with $\Delta x = \Delta y = 0.1$ m. The corresponding time step chosen to ensure stability is $\Delta t = 0.02$ s.

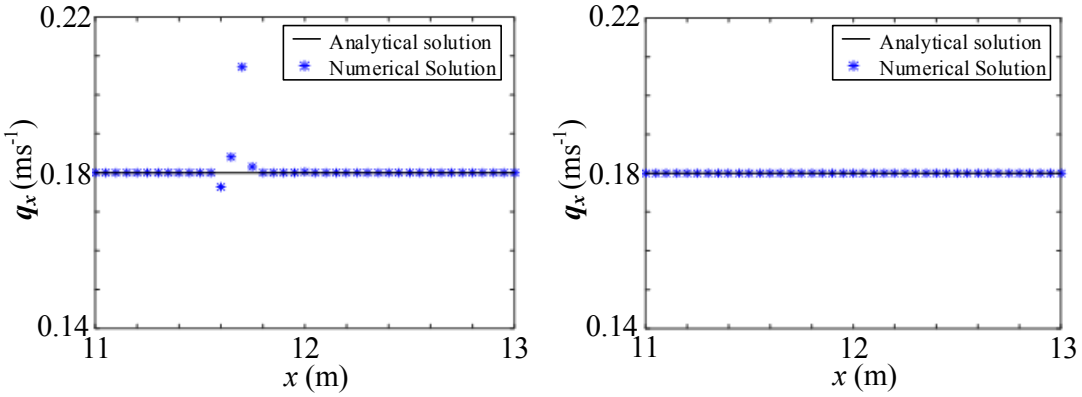

Figure 4.2: Steady flow over a hump; discharge profiles at $t = 1000$ s; (a) updated using momentum equation; (b) sampled following Ying and Wang (2008).

Figure 4.1 shows the results for the free surface elevation and the bed elevation after 1000 s, in 1D and 2D, respectively. Results are in excellent agreement with the analytical solution, obtained by Goutal and Maurel (1997), using the Bernoulli equation and the continuity equation. Figure 4.2(b) presents the discharge profile, obtained following Ying and Wang (2008), using values directly taken from the flux terms of (2.19a), rather than using the updated momentum variables, p_x and p_y, calculated from (2.19b) and (2.19c). If the momentum equation method is used, the discharge produces a spurious result at one or two cells near the hydraulic jump, as seen in Figure 4.2(a). This is merely an artefact of the numerical solver, as explained fully by Ying and Wang (2008).

This test case not only verifies that the numerical model can simulate a hydraulic jump, but also that it can accurately predict the discharge in the presence of a hydraulic jump, verifying the well-balanced property of (2.19).

4.1.2 Case 2: One Dimensional Bores and Rarefactions

The following test cases are taken from Toro (2001). The channel is 50 m in length and has a flat, frictionless bed. Transmissive boundary conditions are applied at each end of the domain. For all five cases $\Delta x = 0.0625$ m, $\Delta y = 0.2$ m and $\Delta t = 0.00125$ s. In cases 2a, 2c, 2d, and 2e, the results are in very close agreement with Toro (2001). For this reason the comparison is not shown in the corresponding figures. For case 2b, there are some discrepancies (discussed below), and the comparison has been included.

Case 2a: Dam break - left rarefaction & right shock

This case simulates the instantaneous removal of a dam wall, located at $x = 10$ m. Initial upstream and downstream water depths in the channel are $h = 1$ m and $h = 0.1$ m, respectively. Initial flow velocity upstream is $u = 2.5$ ms^{-1}. Elsewhere, $u = 0$ ms^{-1}. The model is run until $t = 7.0$ s. As shown in Figure 4.3, a shock wave propagates to the right while a left rarefaction simultaneously propagates to the left. The results for h_* and u_*, the values for the water depth and flow velocity in the region between the shock and rarefaction waves, respectively, are 0.6117 m and 3.865 ms^{-1}, respectively. These results are excellent agreement with those obtained by Toro (2001), who used a very high resolution solver and found $h_* = 0.611753$ m, and $u_* = 3.86398$ ms $^{-1}$.

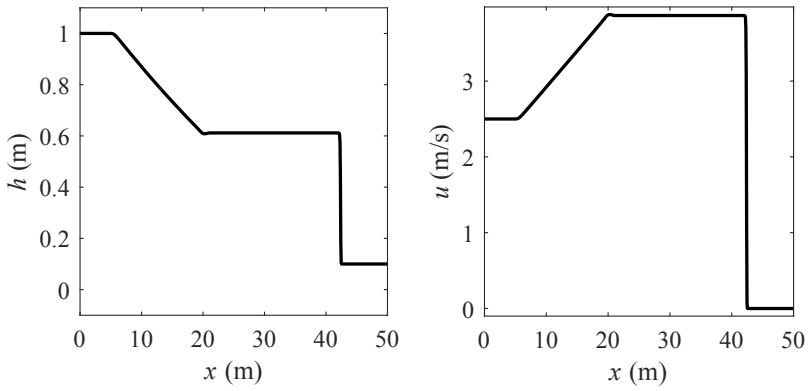

Figure 4.3: Dam break, right wet-bed Riemann problem: water depth (m) and flow velocity (m/s) profiles at $t = 7$ s.

Case 2b: Two rarefactions and nearly dry bed

Two regions of constant water depth, $h = 1$ m, with opposite currents, with speed, $u = 5.0$ ms $^{-1}$, are released. The initial flow discontinuity occurs at the centre of the channel at $x = 25$ m. Figure 4.4 shows the results obtained at $t = 2.5$ s, which are in close agreement to those presented by Toro (2001), noting that there is a slight oscillation in the present numerical results at the original location of the discontinuity. These oscillations do not appear in the solution of Toro (2001) due to the very high resolution of the numerical solver used.

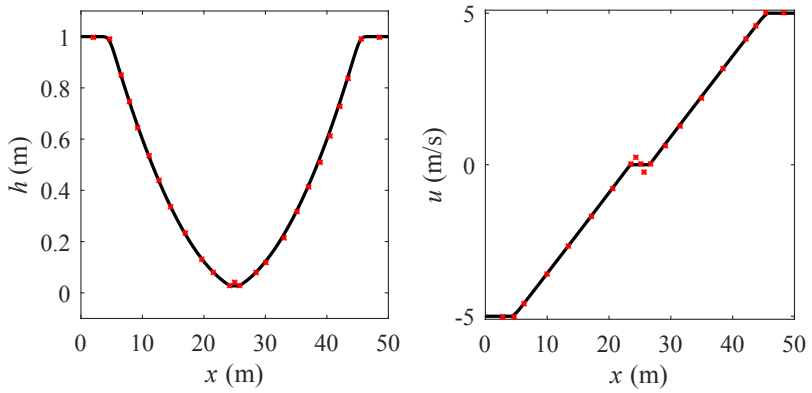

Figure 4.4: Two opposing rarefaction waves: water depth (m) and flow velocity (m/s) profiles at $t = 2.5$ s.

Case 2c: Generation of a dry bed

As with Case 2b, in this case considers two regions of water with opposing currents of equal speed, but with $u = 0.3$ ms $^{-1}$. The initial water depth in both regions is $h = 0.1$ m. The results for the free surface elevation and flow velocity, Figure 4.5, are again in close agreement with those of Toro (2001) at $t_{end} = 5.0$ s.

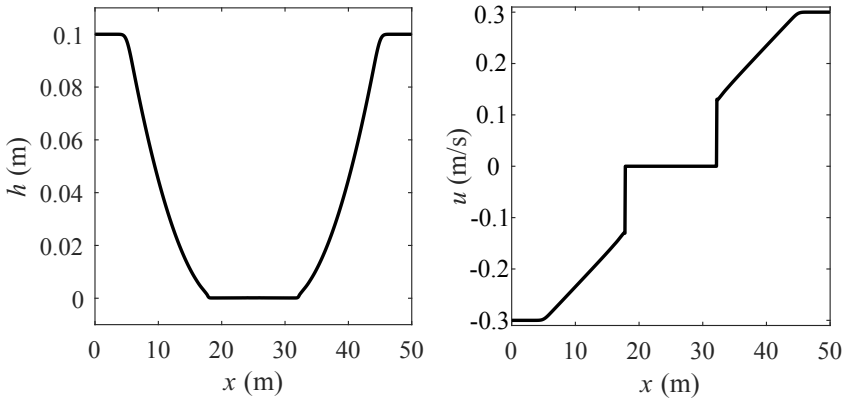

Figure 4.5: Two opposing rarefaction waves generating dry bed: water depth and flow velocity profiles at $t = 5$ s.

Case 2d & 2e: Right/Left dry bed Riemann problem

In this case a dam break, with initial water depth upstream of the dam $h = 1$ m, travels over an initially dry, frictionless horizontal bed, producing a right rarefaction wave. Figure 4.6 shows the results at $t = 4.0$ s, which again, are very similar to those presented by Toro (2001). The left dry bed Riemann problem

is the mirror of the right dry bed problem, as seen in Figure 4.7. This test case verifies the solver's ability to model a simple wet/dry front over a frictionless horizontal bed.

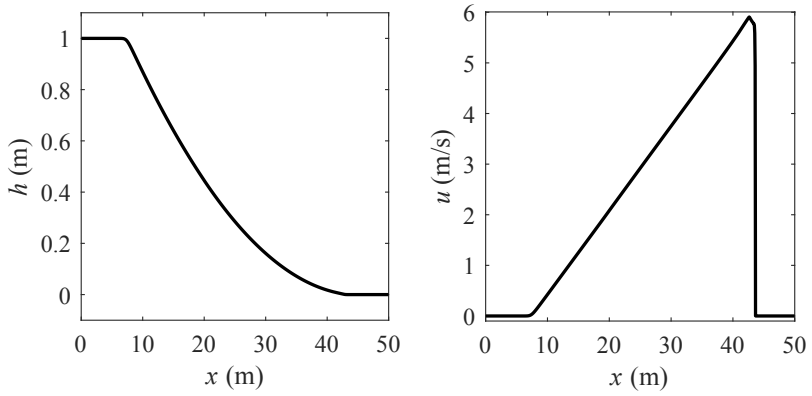

Figure 4.6: Dam break, right dry-bed Riemann problem: water depth and flow velocity profiles at $t = 4$ s.

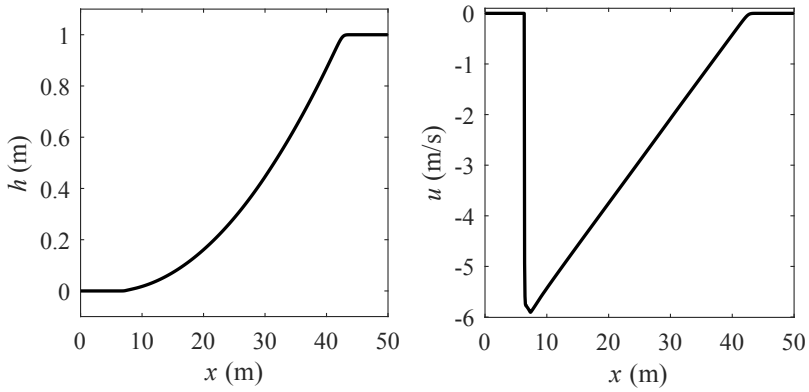

Figure 4.7: Dam break, left dry-bed Riemann problem: water depth and flow velocity profiles at $t = 4$ s.

4.1.3 Case 3: Frictionless Rectangular Dam Breach

This test case involves an asymmetric dam breach in a frictionless channel due to the rapid opening of a sluice gate. It has been used extensively in the literature to examine the performance of Riemann solvers applied to complex, initially discontinuous, shallow-water flows (see e.g. Fennema and Chaudhry, 1990; Alcrudo and García-Navarro, 1993; Mingham and Causon, 1998; Fujihara and Borthwick, 2000; Liang *et al.*, 2004). The discontinuous flow and the lack of symmetry present

a difficult numerical test for the solver. The domain consists of a 200 m square box with a horizontal bed, divided into two equal regions by an infinitesimally thin wall. Two different cases are run; a) an initially wet bed downstream, $h = 5$ m and b) an initially dry bed downstream, $h = 0$ m. In both cases the still water depth upstream of the wall is 10 m. The domain is mapped on a uniform square mesh with 125 cells in both the x and y directions, such that $\Delta x = \Delta y = 1.6$ m. Refining the grid further did not alter the results significantly, ensuring grid convergence was achieved. The time step $\Delta t = 0.01$ s. At $t = 0$ s, a 75 m wide breach is created instantaneously in the dam wall from $y = 95$ m to 170 m. From the results presented in Figure 4.8, at $t = 7.2$ s, it is observed that a shock wave propagates downstream while expanding laterally. At the same time a depression wave propagates upstream. The results are in good agreement with those of Mingham and Causon (1998) and other authors mentioned above, including Liang *et al.* (2004), the latter whose results are included in Figures 4.8 and 4.9 for comparison.

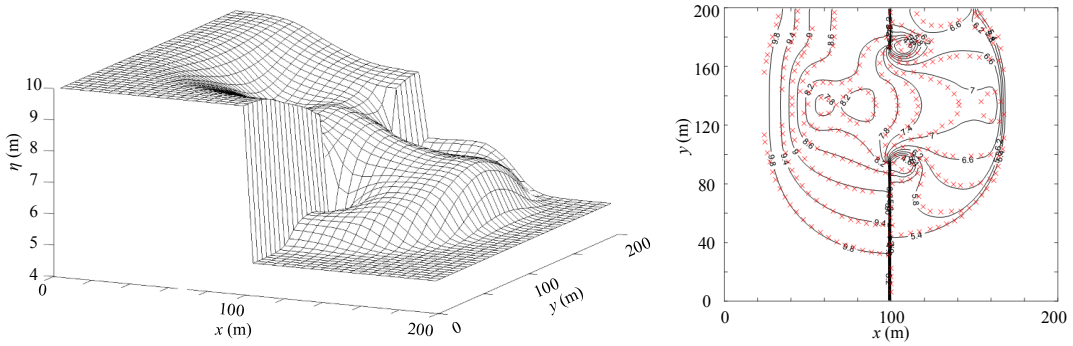

Figure 4.8: Frictionless rectangular dam break with wet bed at $t = 7.2$ s free surface elevation, η, surface and contour plots (m).

It is seen in Figure 4.8 that vortices form at the corners of the dam wall breach, which were also observed by previously mentioned authors. In a real dam breach scenario, these eddies would be produced as a result of flow separation and recirculation at the sharp corner of the dam wall, due to the fluid viscosity. In the numerical simulation, the eddies are a result of artificial numerical viscosity which prevents the velocity going to infinity, as would be predicted using potential theory. This is an interesting component of partial dam breach flows, and will be important when interpreting the numerical simulations of laboratory dam break

flows over mobile beds described in Chapter 5, because the high velocities at these locations can result in an overestimated scour hole being produced during the numerical simulation.

Figure 4.9 show the free surface elevation as a 3D visualisation and a contour plot at $t = 5$ s for the dam breach over an initially dry downstream bed. The bore free surface elevation is lower than in the wet-bed case, and the bore does not expand significantly in the transverse direction. However, the bore propagates at a much faster speed over the dry bed, reaching further downstream by $t = 5$ s than the wet-bed case at $t = 7.2$ s. Again, the results are very similar to those presented by Liang *et al.* (2004).

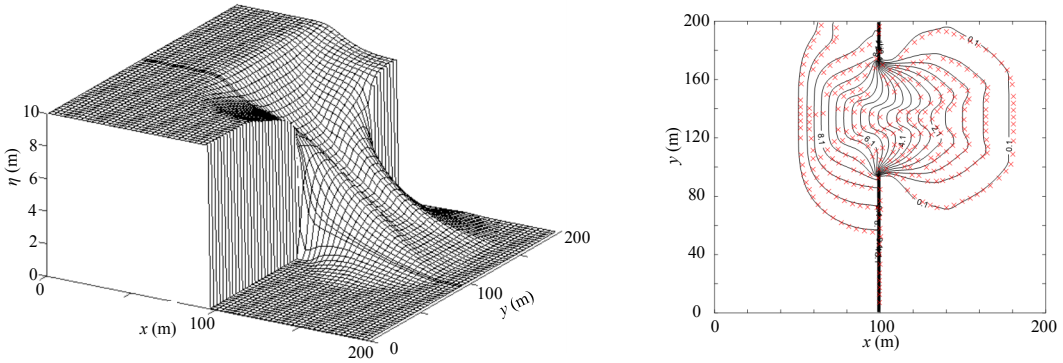

Figure 4.9: Frictionless rectangular dam break with dry bed at $t = 5$ s free surface elevation, η, surface and contour plots (m).

This test confirms that the model can simulate shallow water flows over both wet beds, and dry frictionless, horizontal beds, even for a complicated case involving initially discontinuous, asymmetric flow conditions over an initially dry bed.

4.1.4 Case 4: Circular Dam Breach

The instantaneous collapse of an idealised two-dimensional circular dam is now considered (see for example, Toro, 2001; Liang *et al.*, 2004). It is also noted that Alcrudo and García-Navarro (1993), Lai and Khan (2012) and Liu *et al.* (2013) modelled a similar case, but with different dam geometries. The initial radius of the dam is $r = 2.5$ m. The dam is centred at $x_c = 20$ m and $y_c = 20$ m in a square domain of plan dimensions 40 m x 40 m, which is discretised using square grid cells of length, $\Delta x = \Delta y = 0.16$ m. The time step chosen is $\Delta t = 0.01$ s.

Transmissive boundary conditions are applied at all domain boundaries.

Initially the flow velocity is set to zero everywhere ($u = v = 0$ ms^{-1}) and the initial water depth is given by

$$h(x,y) = \begin{cases} h_{dam} = 2.5\text{m} & \text{if} \quad (x-x_c)^2 + (y-y_c)^2 \leq r^2, \\ h_{domain} = 0.5\text{m} & \text{if} \quad (x-x_c)^2 + (y-y_c)^2 > r^2. \end{cases}$$

The infinitesimally thin wall of the dam is removed instantaneously at the beginning of the simulation. Figure 4.10 shows the model predictions of the free surface and velocity profiles across the centreline of the basin, along the x or y direction, at three time instants. The predictions are in close agreement with the results presented by Toro (2001) and Liang *et al.* (2004). Figure 4.11 presents a 3D representation, and contour plots of the water depth, at $t = 0.4$ s (Figure 4.11a & b), and at $t = 4.7$ s (Figure 4.11c & d). This test case verifies that the model predictions are not affected by grid alignment and also validates the solver's ability to handle transmissive boundary conditions.

The grid chosen for the current model is similar to that used by Toro (2001), but the shock waves produced by the present model are slightly less steep. When the grid resolution of the model is increased, the results converge to Toro's. It should be noted that the WAF numerical method used by Toro (2001) is more accurate than the current method but has the drawback of requiring a large computational stencil, making it awkward to apply near complicated boundaries.

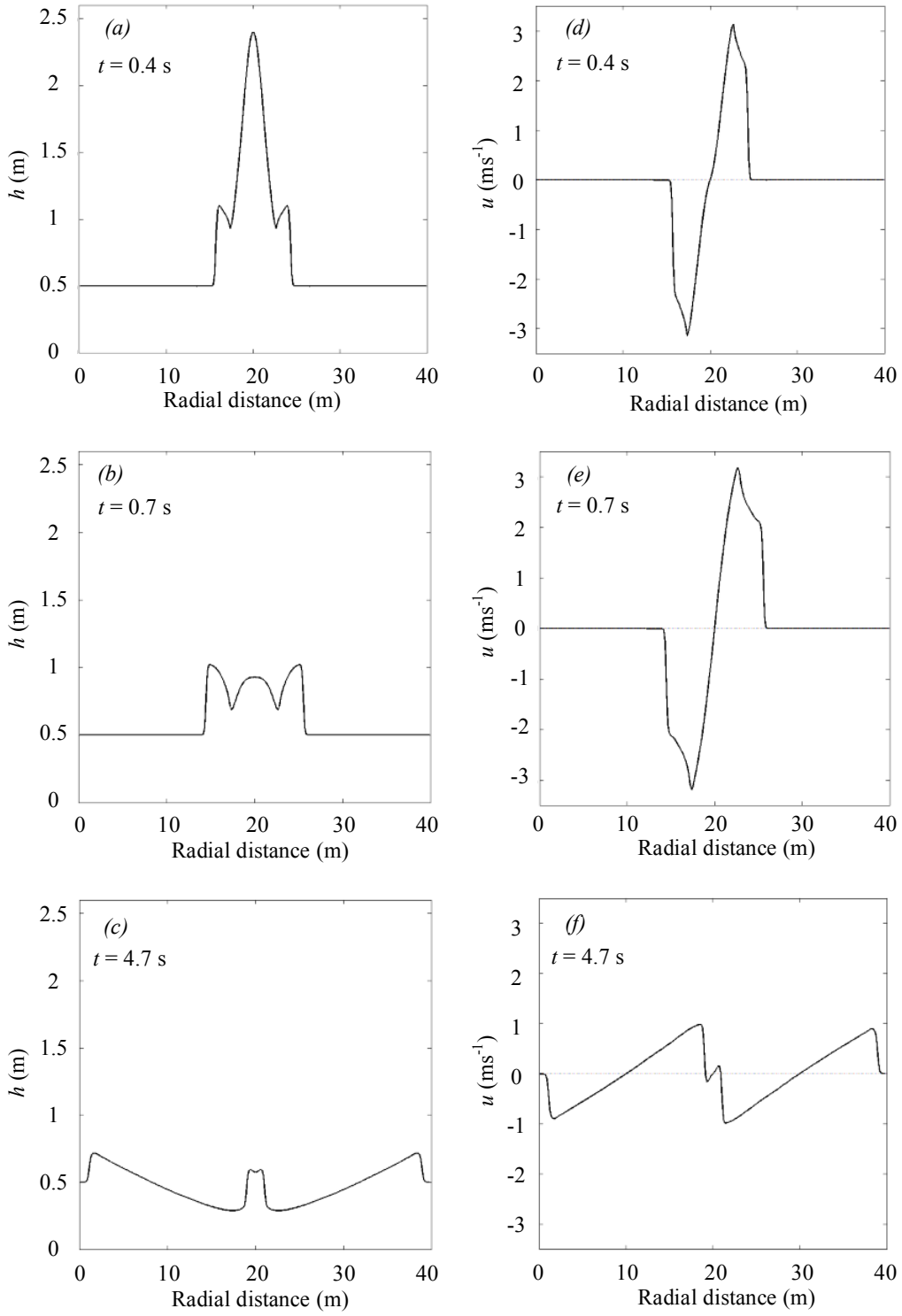

Figure 4.10: Circular dam break; transverse profile of water depth (a-c) and velocity (d-f) along the centreline at $t = 0.4$ s, 0.7 s, and 4.7 s.

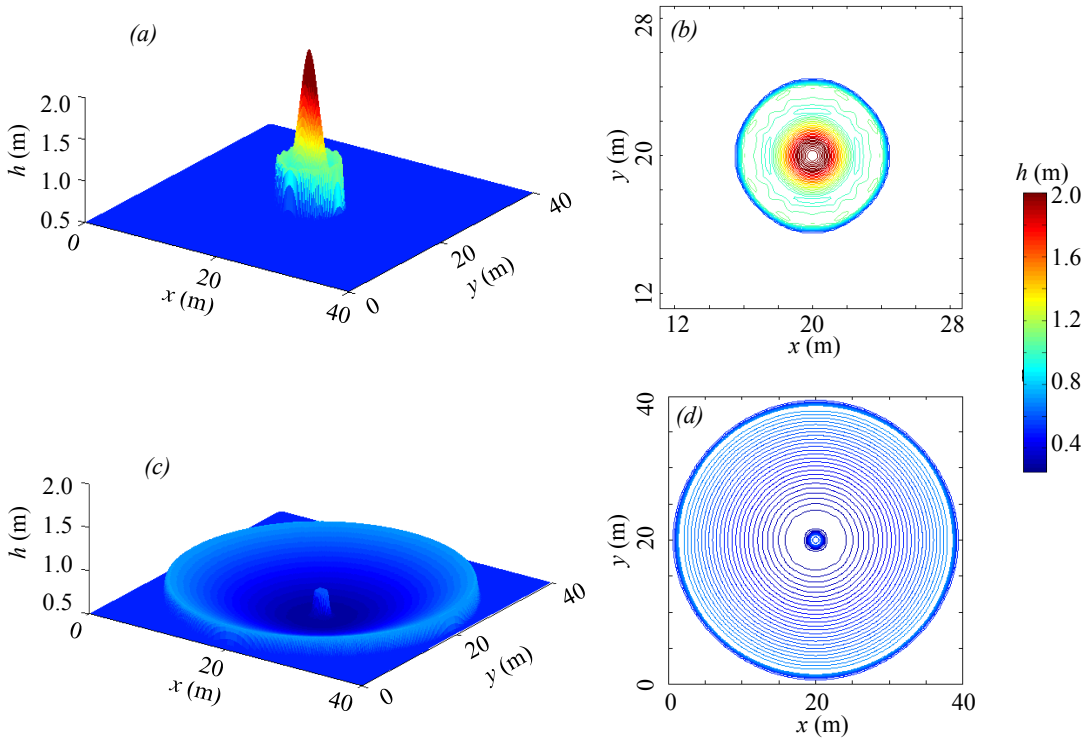

Figure 4.11: Circular dam break water depth h; 3D visualisation and contour plots at; $t = 0.4$ s, and $t = 4.7$ s.

4.2 Shallow Water-Sediment Test Cases

The following test cases are used to analyse the numerical scheme's ability to simulate water-sediment interaction for bedload or suspended sediment transport, or a combination of both. In the case of suspended sediment, it is assumed that the water-sediment mixture is well mixed, and the concentration of suspended sediment is constant through the depth. The well-balanced property of the solver is verified for a variable-density dam break over a immobile bed step. Bedload transport is compared to the semi-analytical solution of Hudson and Sweby (2003) for the evolving morphology of a sandbar under steady flow conditions. Following Apostolidou (2011), suspended sediment entrainment and deposition are simulated separately in a flat-bottomed rectangular tank of still water, and the results compared to semi-analytical solutions. Finally, the model is verified against a benchmark numerical test of a 1D dam break over a mobile bed, first presented by Cao *et al.* (2004).

4.2.1 Case 5: Dam Break over a Bed Step

In order to demonstrate further the need to use the well-balanced shallow water-sediment equations (2.19) under certain conditions, thus improving the general applicability of the numerical model, a test case of variable-density dam break flow over a bed step is presented, which includes a discontinuity in fluid density, similar to test cases presented by Murillo *et al.* (2012).

The dam, located at the centre of a 300 m long channel (at $x = 0$ m), is instantaneously removed at $t = 0$ s. Initially, the upstream and downstream water depths are 4 m and 0.78 m, respectively. For $x \leq 0$ m, $z_b = 0$ m and $c = 0.8$. For $x > 0$ m, $z_b = 1.5$ m and $c = 0$. The relative density of the particles, $s = 2.65$. The bed is fixed and $D = E = 0$.

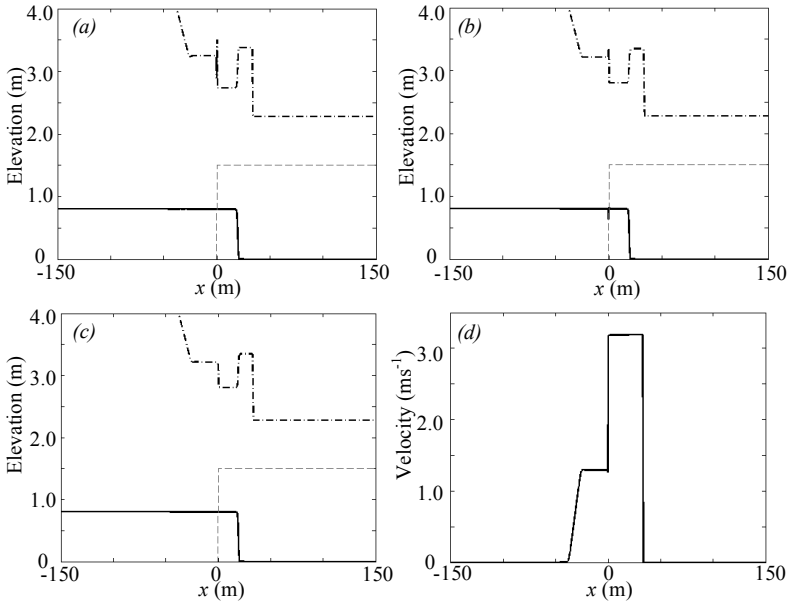

Figure 4.12: Variable density dam break over a bed step: spatial profiles of concentration (solid line), free-surface elevation (dashed-dot) and bed elevation (dashed line) at $t = 6$ s for (a) unbalanced equations (3.1), (b) well-balanced equations, and (c) well-balanced equations including a simple upwinding treatment of $c(i)$ at the bedstep. The velocity profile at $t = 6$ s is given in (d).

This test case is run with three different numerical models. In DB1, the water depth-discharge formulation of the governing equations, (2.14) is used. The results presented in Figure 4.12(a) show that this formulation of the equations is not well-balanced and cannot account for the pressure change at the bed step. Equation (2.19) is used in the two other models. No additional treatment of the density term is used at the bed step for DB2. As seen in Figure 4.12(b), when

(2.19) is used, a small discontinuity develops in the concentration profile at the bed step. This is due to the fact that c is a function of M, M_S and z_b. When the discontinuity in the bed Δz_b is large with respect to η, an unphysical discontinuity is produced in the concentration profile. In order to account for this, a simple upwinding treatment is used in DB3 to update c at the location of a vertical bed step. As seen in Figure 4.12(c), the upwinding eliminates the discontinuity.

In addition, Figure 4.12(d) confirms the property of the Riemann solver identified in Chapter 3, (3.30); the velocity is constant across the shear wave associated with the density discontinuity.

This test case shows that, in theory, the well-balanced governing equations are required to avoid unphysical discontinuities in the free surface elevation profile at a bed step, particularly when the step is large. However, it should be noted that the bathymetry is not discontinuous for most of the laboratory data presented in the literature for variable-density flows. As such, further laboratory studies are necessary to validate well-balanced models for real engineering scenarios of variable-density flow over sharp discontinuities.

4.2.2 Case 6: Bedload Evolution of a 1D Sandbar in Steady Flow

This test is used to verify that the solver is capable of modelling bedload transport and bed morphodynamic change. It is a 2D simulation analogous to the 1-D test case presented by Hudson and Sweby (2003) to predict the evolution of a sandbar along a flat, frictionless, non-erodible bed in an open channel. The case was subsequently modelled by other researchers including, Castro Díaz *et al.* (2008), Huang *et al.* (2008) and Zhou (2014). An approximate analytical solution for the bed morphology was developed by Hudson and Sweby (2003) following De Vries (1973).

The problem domain consists of a frictionless channel of plan dimensions length 1000 m x width 240 m. The initial horizontal bed is flat everywhere, except for a 1 m high hump located between $x_1 = 300$ m and $x_2 = 500$ m. The

initial conditions for flow depth, h, bed elevation, z_b, and flow velocity, u are:

$$h(x, t_0) = 10.0 \text{ m} - z_b(x, t_0) \ ,$$

$$z_b(x, t_0) = \begin{cases} z_{b\max} \sin^2\left(\frac{\pi(x-x_1)}{(x_2-x_1)}\right) \text{ m} & \text{if} \quad 300 \text{ m} \leq x \leq 500 \text{ m}, \\ 0 & \text{otherwise}, \end{cases}$$

and

$$u(x, t_0) = \frac{q_0}{h(x, t_0)} \ ,$$

where $z_{b\max} = 1$ m is the maximum initial height of the hump, and $q_0 = 10$ m^{2}s^{-1} is the initial flow discharge. The bedload flux, q_b, is calculated using the Meyer-Peter-Mueller formula (2.22). The porosity of the bed, $\varepsilon = 0.4$. Bedload transport dominates, and so suspended sediment, deposition and entrainment processes are set to zero.

Hudson and Sweby (2003) use the sediment transport flux of Grass, (2.21), to model bedload transport. For $m = 3$, $\eta = 10$ m and $A = 0.01$ s^{2}m^{-1}, the approximate analytical solution presented by Hudson and Sweby (2003) is valid until t ≈ 23800 s.

It is possible to model bedload transport over a frictionless bed using (2.21), because the value of A can be chosen arbitrarily. However, in order to use the MPM formula (2.22), it is necessary to define an equivalent friction coefficient $\mathcal{C}_f$ to estimate the value of the Shields parameter θ, required for (2.22). Assuming that $\theta \gg \theta_c$ - a reasonable assumption for intense bedload transport (Hudson and Sweby, 2003) - following Maldonado-Villanueva (2015), and noting that $\theta =$

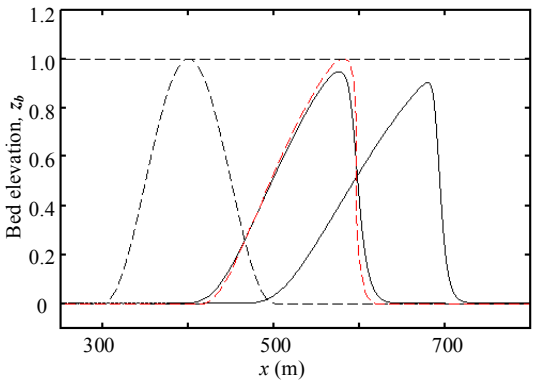

Figure 4.13: Evolution of a 1D hump; bed hump profile at $t = 0$ (dashed black line), analytical solution at $t/T = 11.9$ (dashed red line), and the numerical results (solid black line) at $t = 23800$ s and 33000 s.

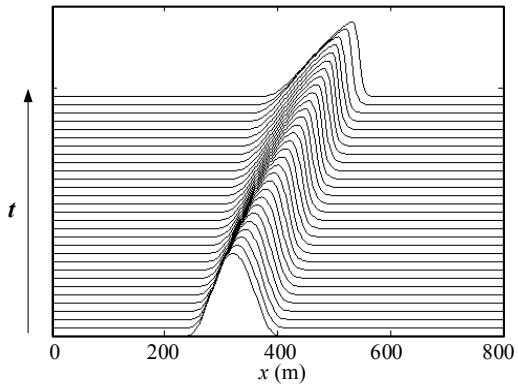

Figure 4.14: Evolution of 1D hump; stacked x - t plots from t= 0 until t = 33000 s.

$\frac{C_f u|u|}{(s-1)gd}$, the bedload discharge can be rewritten from (2.22) as

$$q_b = \frac{8C_f^{3/2}}{(s-1)g} u|u|^2 = Au|u|^2 \ . \tag{4.1}$$

Rearranging (4.1), C_f is estimated by

$$C_f = \frac{A(s-1)g}{8}^{2/3} \ . \tag{4.2}$$

The value of C_f derived from (4.2) is used only to calculate the bedload discharge. The friction coefficient in the momentum equations is still zero, maintaining the frictionless channel modelled by Hudson and Sweby (2003).

The numerical grid comprises 400 cells in the x direction, such that $\Delta x =$ 2.5 m, and 5 cells in the y direction, such that $\Delta y = 5$ m. The time step, $\Delta t = 0.1$ s. The model is initially run for approximately 40,000 s, with the bed fixed, until a steady-state flow field is achieved. The model is then run for 33,000 s with a mobile bed. Since no exact analytical solution exists for this problem, the numerical results are compared to the approximate analytical solution given by Hudson and Sweby (2003), where it is assumed that the flow discharge and the

free surface elevation remain constant throughout the whole domain.

Figure 4.13 shows the numerical model results are in satisfactory agreement with the approximate analytical solution. As the sandbar propagates along the bed (Figure 4.14), the downstream face steepens, eventually forming a vertical shock after $t \approx 23800$ s, after which time the analytical solution is no longer valid. However, as seen in Figure 4.13, the numerical model is valid for all $t > 0$ s. Use of the modified critical Shields parameter from (2.23) prevents non-physical oscillations forming in the bed profile which can occur when using a finite difference solver for the bed morphological equation (2.19e) (see e.g. Huang *et al.*, 2008), because it allows for the diffusion which occurs naturally in bedload transport on steep-sloping beds (see e.g. Soulsby, 1997).

4.2.3 Case 7: Bedload Evolution of a 2D hump in Steady Flow

This test case was presented first by de Vriend (1987), and later simulated by Hudson and Sweby (2005), Huang *et al.* (2010) and Castro Díaz *et al.* (2009), among others. A similar case was modelled by Lesser *et al.* (2004), who used different geometry and initial conditions. The test case consists of a channel with dimensions, 1500 m $\times$ 1000 m, and initial conditions,

$$h(x,t_0) = 10.0 - z_b(x,t_0) \ ,$$

$$z_b(x,t_0) = \begin{cases} z_{b\max}\sin^2\left(\frac{\pi(x-x_1)}{(x_2-x_1)}\right)\sin^2\left(\frac{\pi(y-y_1)}{(y_2-y_1)}\right) & \text{if} \quad 300 \le x \le 500, \ 400 \le y \le 600 \\ 0 & \text{otherwise,} \end{cases}$$

$$\text{and} \quad u(x,t_0) = \frac{q_0}{h(x,t_0)} \ ,$$

where all values are in (m) and (s); $z_{b\max} = 1$m is the initial height of the dome, and $q_0 = 10\text{m}^2\text{s}^{-1}$ is the initial flow discharge. Previous authors used the Grass bedload equation to calculate the bedload discharge q_b. Using an approximate

analytical solution, de Vriend (1987) deduced that the dome would spread into a star shape as it propagated downstream by $t = 200$ hrs for$A = 0.001$ s^{2}m^{-1}, where A is the Grass constant in (2.21). This time is equivalent to $t = 2$ hrs for $A = 0.1$ s^{2}m^{-1}.

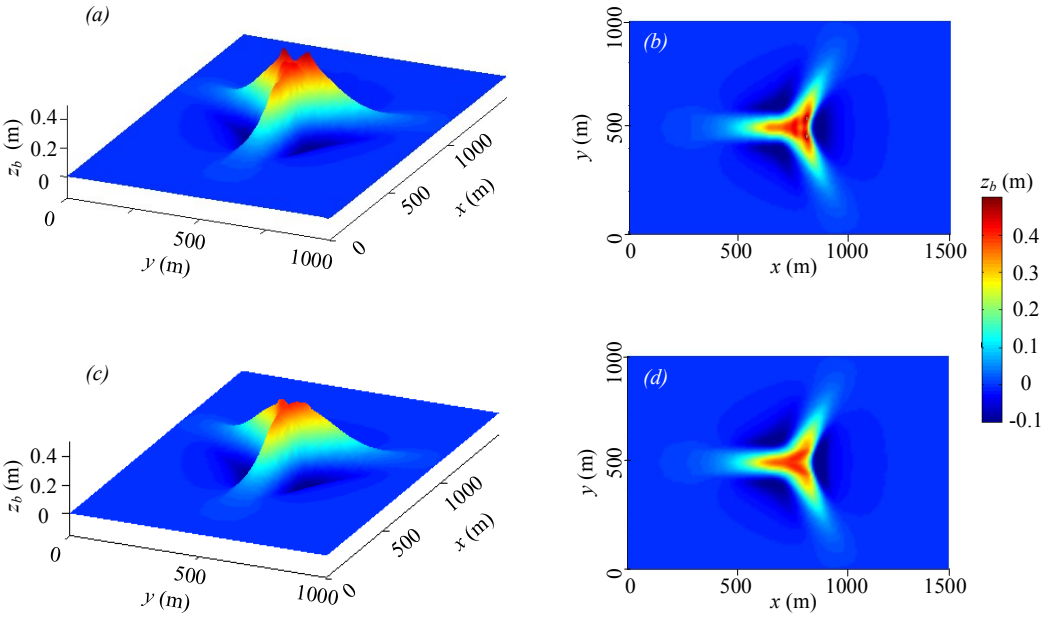

Figure 4.15: Evolution of a 2D hump at $t = 2$ hrs; 3D and plan view. Bed-load transport calculated using (a) second-order central differences, and (b) a combination of second-order central differences and upwinding.

Again, C_f is calculated with (4.1). The bed porosity $\varepsilon = 0.4$, the grain diameter $d = 0.2$ mm and the density of sediment grains $\rho_s = 2650$ kgm^3. In the numerical model, the domain is mapped onto a uniform mesh with $\Delta x = \Delta y = 10$ m. The time step $\Delta t = 0.4$ s. As with the previous case 4.2.2, the model is initially run over a fixed bed until a steady state flow field is achieved. The model is then run over a mobile bed for $t = 2$ hrs.

Results in Figure 4.15 are presented for two different methods for updating the bed morphology equation (2.19e) using; (i) second-order central differences; or (ii) a weighted finite difference scheme, such that,

$$\frac{\partial q_b}{\partial x} = \frac{1}{2}\left(\frac{q_b(i+1,j) - q_b(i-1,j)}{2\Delta x} + \frac{3q_b(i,j) - 4q_b(i-1,j) - q_b(i-2,j)}{2\Delta x}\right), \tag{4.3a}$$

and

$$\frac{\partial q_b}{\partial y} = \frac{1}{2}\left(\frac{q_b(i,j+1) - q_b(i,j-1)}{2\Delta x} + \frac{3q_b(i,j) - 4q_b(i,j-1) - q_b(i,j-2)}{2\Delta x}\right) . \tag{4.3b}$$

In both cases, the dome spreads into a star shape, as expected following de Vriend (1987). In Figure 4.15a, small peaks are observed in the bed surface as is steepens with time. This is a common difficulty encountered when using central difference schemes (Huang *et al.*, 2010), even when the critical Shields parameter is modified to account for flow over steep-sloping beds, as in (2.22). As mentioned in Chapter 2, other methods have been presented in the literature to account for the effect of bed-slope on bedload transport, which include a diffusion term in the calculation of the bedload discharge q_b (see e.g. Johnson and Zyserman, 2002; Maldonado-Villanueva, 2015). For future work, it would be interesting to investigate the final bed topography of this test case using a diffusion-based bedload transport model.

4.2.4 Case 8: Suspended Sediment

To verify the model's capability to simulate accurately deposition and entrainment of suspended sediment, simple semi-analytical solutions are derived using the water depth-discharge form of the governing equations (2.14), following a similar approach to that of Apostolidou (2011). Two cases are presented below: deposition in the absence of entrainment; and entrainment without deposition. In both cases, the problem consists of a flat-bottomed rectangular tank with a fixed free surface elevation. Neglecting bedload transport, (2.14) is rearranged following Cao *et al.* (2004) so that the variable density term does not appear on the left-hand side. This is achieved by substituting (2.14d) and (2.14e) into (2.14a), (2.14b) and (2.14c), and rearranging, such that,

$$\frac{\partial h}{\partial t} + \frac{\partial hu}{\partial x} + \frac{\partial hv}{\partial y} = \frac{E - D}{(1-\varepsilon)} , \tag{4.4a}$$

$$\frac{\partial uh}{\partial t} + \frac{\partial}{\partial x}\big(u^2h + \frac{1}{2}gh^2\big) + \frac{\partial (uvh)}{\partial y}$$

$$= -gh\frac{\partial z_b}{\partial x} - \frac{\tau_{b_x}}{\rho} - \frac{(\rho_s - \rho_w)}{2\rho}gh^2\frac{\partial c}{\partial x} - \frac{(\rho_0 - \rho)(E-D)u}{\rho(1-\varepsilon)} \ , \qquad (4.4b)$$

$$\frac{\partial (vh)}{\partial t} + \frac{\partial}{\partial y}(v^2h + \frac{1}{2}\rho gh^2) + \frac{\partial (uvh)}{\partial x}$$

$$= -gh\frac{\partial z_b}{\partial y} - \frac{\tau_{b_y}}{\rho} - \frac{(\rho_s - \rho_w)}{2\rho}gh^2\frac{\partial c}{\partial y} - \frac{(\rho_0 - \rho)(E-D)v}{\rho(1-\varepsilon)} \ , \qquad (4.4c)$$

$$\frac{\partial hc}{\partial t} + \frac{\partial huc}{\partial x} + \frac{\partial hvc}{\partial y} = E - D \ , \qquad (4.4d)$$

and

$$\frac{\partial z_b}{\partial t} = \frac{1}{(1-\varepsilon)}\big(D - E\big) \ . \qquad (4.4e)$$

No further assumptions are required to obtain (4.4) from (2.14).

When there is no horizontal flow, but there is intense vertical mixing to maintain a homogeneous concentration along the depth, in a tank with a horizontal bed and a horizontal free surface, the governing equations further reduce to

$$\frac{\partial h}{\partial t} = \frac{E-D}{(1-\varepsilon)} \ , \qquad (4.5a)$$

$$\frac{\partial ch}{\partial t} = E - D \ , \qquad (4.5b)$$

and

$$\frac{\partial z_b}{\partial t} = \frac{D-E}{(1-\varepsilon)} = -\frac{\partial h}{\partial t} \ . \qquad (4.5c)$$

Case 8a: Deposition in flat-bottomed tank of still water with no entrainment

For deposition of dilute suspended sediment in a flat-bottomed tank with no net flow and no entrainment, but intense vertical mixing, $u = 0$, $E = 0$, $\tau_b = 0$, and $D = cw_s$,

$$\frac{\partial h}{\partial t} = \frac{-w_s}{(1-\varepsilon)}c = -\frac{\partial z_b}{\partial t} \ , \tag{4.6a}$$

and

$$\frac{\partial ch}{\partial t} = -cw_s \ , \tag{4.6b}$$

Using the chain rule, (4.6b) becomes

$$c\frac{\partial h}{\partial t} + h\frac{\partial c}{\partial t} = -cw_s. \tag{4.7}$$

Assuming that the solution is in the form $c = c_0 e^{-t/T}$ for any time $0 \leq t \leq \infty$, where T is a characteristic time constant, then $\frac{\partial c}{\partial t} = -\frac{c_0}{T}e^{-t/T}$ and, substituting into (4.7) and dividing both sides by $c = c_0 e^{-t/T}$, gives

$$\frac{\partial h}{\partial t} - \frac{h}{T} = -w_s. \tag{4.8}$$

Combining (4.6a) with (4.8) yields

$$\frac{-w_s}{(1-\varepsilon)}c_0 e^{-t/T} - \frac{h}{T} = -w_s \ . \tag{4.9}$$

At $t = 0$

$$\frac{-w_s}{(1-\varepsilon)}c_0 - \frac{h_0}{T} = -w_s \ , \tag{4.10}$$

and so

$$T = \frac{h_0}{w_s\left(1 - \frac{1}{(1-\varepsilon)}c_0\right)} \ . \tag{4.11}$$

Now, integrating (4.6a) one obtains

$$h = h_0 + \frac{-w_s}{(1-\varepsilon)} \int_0^t c\mathrm{dt} \ . \tag{4.12}$$

The change in depth of the mixture can thus be written

$$h - h_0 = \frac{-w_s}{(1-\varepsilon)} \int_0^t c_0 e^{-t/T} dt = \frac{-c_0 w_s T}{(1-\varepsilon)}(e^{-t/T} - 1) = z_{b0} - z_b \ . \tag{4.13}$$

Substituting (4.11) into (4.13) for T, one can write

$$h = h_0 - \frac{c_0 h_0}{(1-\varepsilon-c_0)}(e^{-t/T} - 1) \ , \tag{4.14}$$

and

$$z_b = z_{b0} + \frac{c_0 h_0}{(1-\varepsilon-c_0)}(e^{-t/T} - 1) \ . \tag{4.15}$$

In the above equations, h_0, z_{b0}, and c_0 are initial values for the water depth, the bed elevation above a fixed horizontal datum and the depth-averaged concentration of suspended sediment (at time $t = 0$). h, z_b and c are the water height, bed elevation and depth-averaged concentration of suspended sediment at any time, $t > 0$.

In the numerical model, the initial free surface water elevation and bed elevation are 6 m and 1 m above the datum, respectively. The numerical model is run for 5000 s with an initial concentration of suspended sediment equal to 0.5 %. Figure 4.16 depicts the time histories of the bed elevation, water depth and ele-

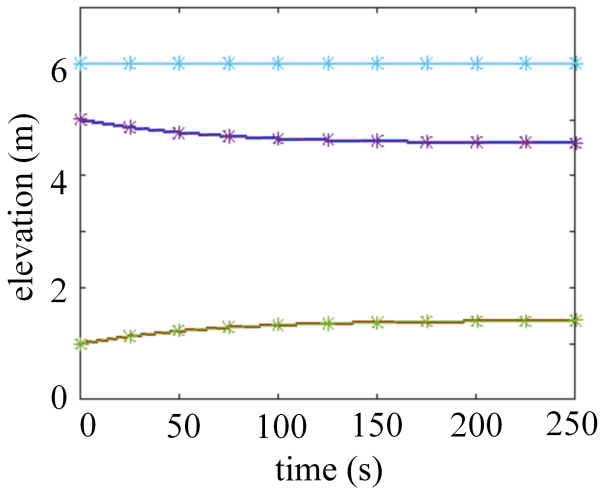

Figure 4.16: Evolution of deposition of suspended sediment at cross section of tank; profiles of bed elevation (brown), water depth (dark blue) and free surface (light blue). Analytical solution shown as solid line. Numerical results shown as stars.

vation of the free surface. The majority of the sediment settles out in the first few hundred seconds and the rate of deposition decreases exponentially with time, in perfect agreement with the semi-analytical solution. The results confirm that the bed level increases at the same rate as the water depth decreases and that the free surface elevation remains constant, thus conserving the mass of water and sediment.

Case 8b: Entrainment in flat-bottomed tank of still water without deposition

This test case is used to verify that the model can simulate the entrainment of sediment into suspension while conserving the mass of sediment and water. There is no deposition of suspended sediment. The numerical results are again compared to a semi-analytical solution derived from Equations (4.5). The entrainment, E, is given by Soulsby (1997) as

$$E = \begin{cases} E_M\left(\frac{\tau_b - \tau_c}{\tau_c}\right) & \text{for} \quad \tau_b > \tau_c \\ 0 & \text{otherwise,} \end{cases}$$

where τ_b is the total bed shear stress, τ_c is the critical bed shear stress and E_M is the entrainment constant. Here E is kept constant by fixing E_M, τ_b and τ_c as constants.

For constant entrainment of dilute suspended sediment in a frictionless, flat-bottomed tank with no net flow and no entrainment but intense vertical mixing, $u = 0$ and $D = 0$, and equations (4.5a) and (4.5c) can be written,

$$\frac{\partial h}{\partial t} = \frac{E}{(1-\varepsilon)}, \tag{4.16a}$$

and

$$\frac{\partial z_b}{\partial t} = -\frac{E}{(1-\varepsilon)} \ . \tag{4.16b}$$

Integrating (4.16), the solution of h and z_b is obtained, such that,

$$h = h_0 + \frac{E}{(1-\varepsilon)} t \ , \tag{4.17}$$

and

$$z_b = z_{b0} - \frac{E}{(1-\varepsilon)} t \ . \tag{4.18}$$

The initial free surface water elevation and bed elevation are again set to 6 m and 1 m, respectively. The bed shear stress, τ_b = 1 Nm^{-2}, the threshold bed shear stress, τ_c= 0.2 Nm^{-2} and the entrainment constant, E_M = 0.001 ms^{-1}. The numerical model is run until t = 5000 s with an initial concentration of suspended sediment equal to zero. The numerical predictions are in excellent agreement with the analytical solution. Figure 4.17 shows that the concentration of suspended sediment increases at a constant rate with time, as would be expected given that the entrainment is constant. The bed elevation decreases at the same rate as the depth of water increases. The excellent agreement between the model prediction and the analytical solution confirms that the mass of sediment and water is conserved.

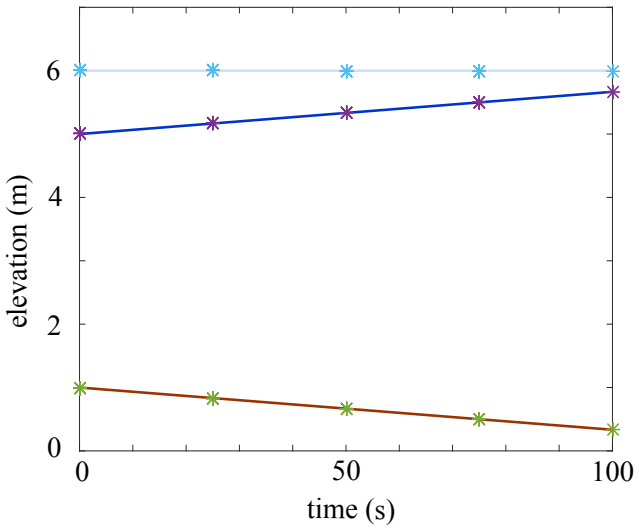

Figure 4.17: Evolution of entrainment of bed material into suspension at cross section of tank; bed elevation (brown), water depth (dark blue) and free surface (light blue). Analytical solution shown as solid line. Numerical results shown as stars.

4.2.5 Case 9: Idealised Dam Break over Mobile Bed

To test the capacity of the model to simulate accurately the interaction between a mobile bed and rapidly-varying dam break flow dynamics and to investigate further the eigenvalue problem of the variable-density governing equations, numerical solutions are compared to a numerical test presented by Cao *et al.* (2004) of a 1D idealised dam break over a mobile bed. The dam, placed at the centre of

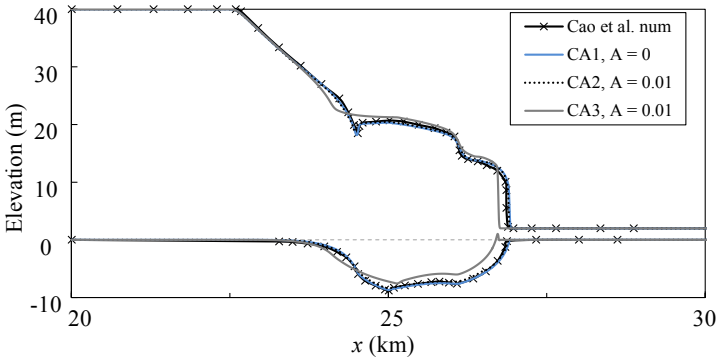

Figure 4.18: Cao *et al.* (2004) dam break: bed elevation and free surface elevation (m) at $t = 2$ min. Numerical results (solid or dashed lines) plotted alongside numerical results of Cao *et al.* (2004) ($\times$). Initial bed level is also included (dashed line).

a 50 km long channel, separates initial upstream and downstream river depths, 40 m and 2 m, respectively. The bed is composed of uniform sediment, $d = 4$ mm,

and is erodible along the entire channel length. The Manning's roughness coefficient, $n = 0.03$ sm$^{-1/3}$, is used to calculate the bed shear stress. For simplicity, the bedload discharge components in the x and y directions are expressed using the Grass formula given by (2.21).

Three different variations of the test case were modelled; CA1, CA2 and CA3. In CA1, all of the parameters were chosen to be identical to those used by Cao

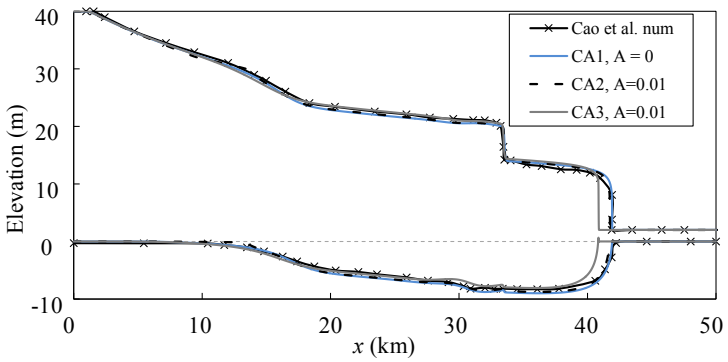

Figure 4.19: Cao *et al.* (2004) dam break: bed elevation and free surface elevation (m) at $t = 20$ min. Numerical results (solid or dashed lines) plotted alongside numerical results of Cao *et al.* (2004) ($\times$). Initial bed level is also included (dashed line).

et al. (2004), including the grid size, $\Delta x = 10$ m and entrainment coefficient, $\alpha_e = 0.015$, and the Grass constant in (2.21), $A = 0$ s, i.e. only suspended sediment is considered. In CA2, $A = 0.01$ s$^2m^{-1}$ and the Rouse number condition (Section 2.4.3) is used to determine the dominant transport process. For CA3, $A = 0.01$ s$^2m^{-1}$ but the Rouse number is not used, i.e. it is assumed that both bedload transport and suspended sediment transport occur simultaneously for all $t > 0$. The third case is similar to the model proposed by Benkhaldoun *et al.* (2013). Figure 4.18 and Figure 4.19 show the results for bed elevation and free surface elevation at $t = 2$ min and $t = 20$ min, respectively.

Figure 4.20 shows the volumetric concentration of suspended sediment as it evolves from $t = 2$ min to $t = 20$ min for case CA1 only.

In Figures 4.18 and 4.19, there is very little difference between the results of cases CA1 and CA2, and these are in almost exact agreement with the numerical results computed by Cao *et al.* (2004). This confirms the assumption made by Cao *et al.* (2004) that suspended sediment is the dominant transport mechanism. However, if bedload transport is assumed to occur for all $t > 0$ (CA3; R_n not

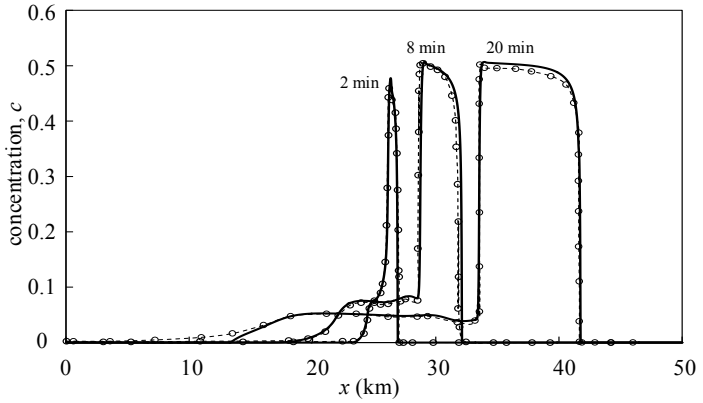

Figure 4.20: Cao *et al.* (2004) dam break: volumetric concentration of suspended sediment after 2 min, 8 min and 20 min. Numerical results (solid lines) are plotted against results obtained by Cao *et al.* (2004) (dotted lines with circles).

considered but $A = 0.01$), the bed elevation and free surface elevation profiles are somewhat different from cases CA1 and CA2. The results of case CA3 are very similar to the results obtained by Benkhaldoun *et al.* (2013) who did not consider which mode of transport dominated, but instead assumed bedload transport occurred for all $t > 0$ used in case 3, although Benkhaldoun *et al.* proposed a different method of solving the bed morphological equation (2.19e). These results highlight the importance of the Rouse number condition and the sensitivity of the final results to the sediment transport equations used in the model.

An important aspect of this test case to note is that the excellent agreement with Cao *et al.* (2004), who used an HLLC solver of the water depth-discharge $(h - q)$ form of the shallow water-sediment equations, confirms the assumption made in Section 3.4; the same wave speed estimates can be used for the well-balanced form of the governing equations, even when the Jacobian matrices of the two systems are not identical. Figure 4.21 shows the stacked $x-t$ plots of the evolution of free surface elevation, η, the horizontal flow velocity, u, the volumetric concentration, c and the bed elevation, z_b from time, $t > 0$ to $t = 20$ min. After the initial dam break, a large volume of sediment is entrained into suspension as the fast moving bore front passes along the bed. The fast-moving bore continues to entrain sediment as it propagates downstream, creating a deep scour hole in the region between the bore front and the contact discontinuity. This contact discontinuity, which is represented by a sharp increase in free surface elevation and a sharp decrease in sediment concentration, marks the interface between

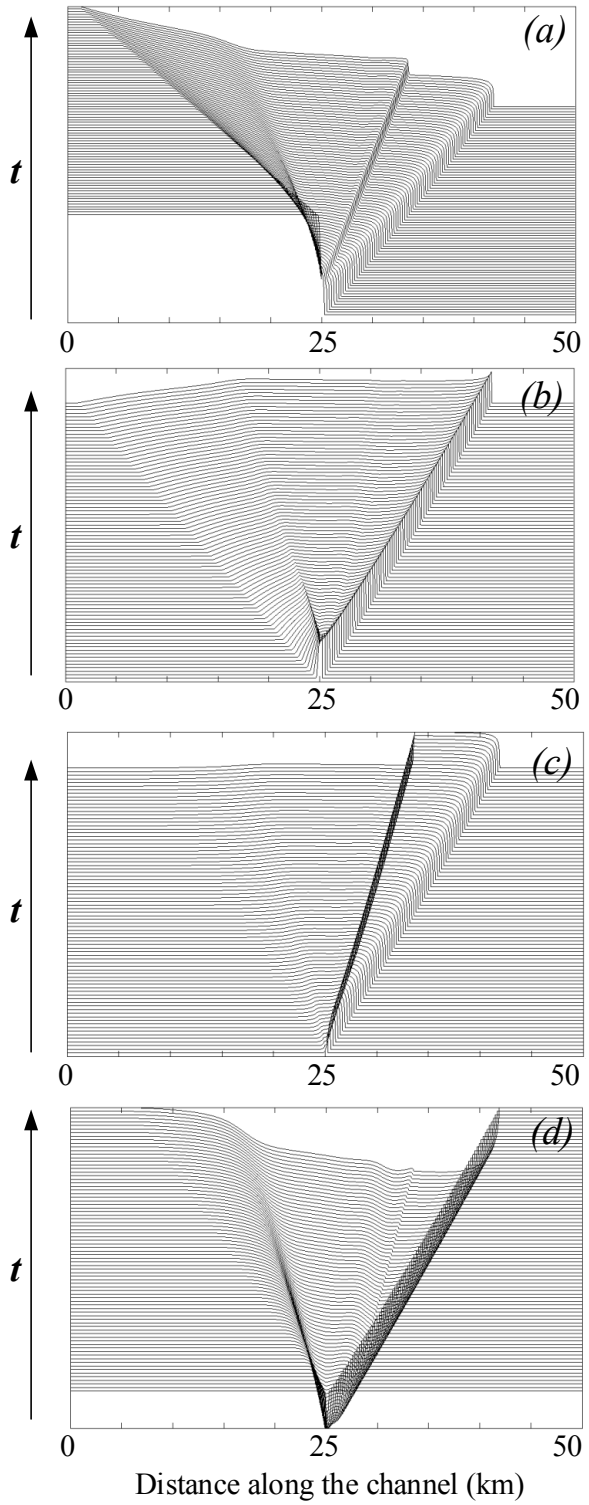

Figure 4.21: Cao *et al.* (2004) dam break: stacked $x - t$ plots for (a) the free surface elevation (m), (b) the streamwise velocity, u, (c) suspended sediment concentration, and (d) bed elevation (m) for $t \leq 20$ minutes.

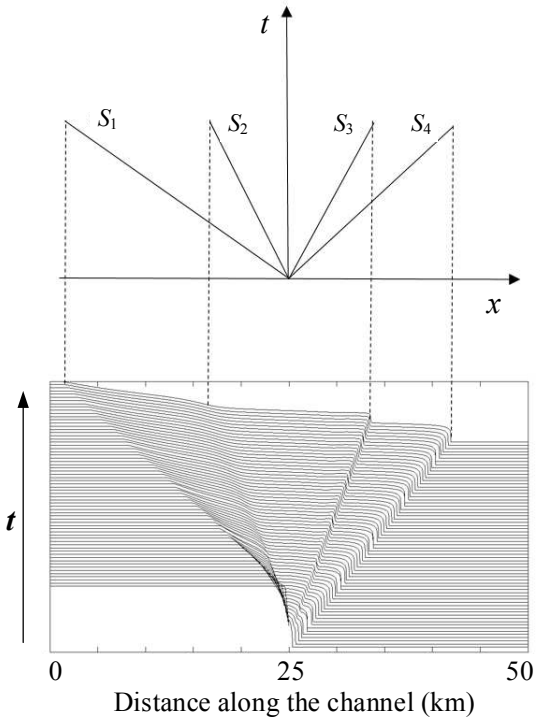

Figure 4.22: Cao *et al.* (2004) dam break: characteristic wave structure of the dam-break flow over mobile bed. (dotted lines with markers).

the highly concentrated water-sediment mixture in the bore, and the region of lower volumetric concentration. The sharp increase in free surface elevation at this point ensures that there is mass conservation of the water-sediment mixture. Upstream of the initial dam location ($x < 25$ km), a small amount of bed erosion is observed due to the passing of the rarefaction wave, but only in the region where the velocities are large enough for the bed shear stress to exceed the critical shear stress. Investigating the wave celerities and eigenvalues of the dam break problem, the local dynamic wave velocity $a = \sqrt{gh}$, of the bore front is approximately 14 ms^{-1}. Figure 4.22 shows the waves, S_1 to S_4, which demark the leading faces of the shock, rarefaction and shear waves. The speeds of these waves are calculated using the $x - t$ plot in Figure 4.21, where S_1 = -19.3 ms^{-1}, S_2 = -6.3 ms^{-1}, $S_3 = 7.05$ ms^{-1} and $S_4 = 14$ ms^{-1}. S_1 is the left rarefaction wave speed, S_4 is the right shock wave and bore front wave speed, and $S_2 \approx S_3$ is the contact wave speed. These wave speeds are in agreement with the eigenvalue problem where,

$$\lambda_1 = u_1 - a = 0 - \sqrt{gh_1} = -\sqrt{(9.81)(40)} = -19.8 \text{ ms}^{-1} = S_1,$$

$$\lambda_2 = S_* = 7 \text{ ms}^{-1} = S_2 = S_3,$$

$$\lambda_3 = u_2 + a = 0 + \sqrt{gh_2} = \sqrt{(9.81)(20)} = 14 \text{ ms}^{-1} = S_4,$$

where u_1 and h_1 are the flow velocity and water depth upstream of the rarefaction wave, u_2 is the flow velocity downstream of the shock wave, h_2 is the water depth of the shock wave and S_* is the flow velocity of the plateau which develops between the rarefaction and shock waves. This provides further verification of the numerical solver, in that the eigenvalues, (3.4), are the same for the variable-density and constant density cases, except for an additional eigenvalue in the variable-density case which represents the contact discontinuity in fluid density.

4.3 Chapter Summary

This chapter has presented numerical test cases carefully selected to verify that the numerical solver is capable of reproducing accurately complex shallow water flows and water-sediment interactions. Dam break flows in one and two dimensions have verified that the model can predict the correct propagation of a hydraulic bore over wet and dry beds. The numerical simulation results are in satisfactory agreement with high resolution numerical models in the literature.

The well-balanced property of the equations has been verified for clear water flow over a smoothly varied, but steep sloping bathymetry, and variable-density flow over a bed step. The results are in excellent agreement with analytical solutions.

Simulations of bedload transport and suspended sediment transport have verified conservation of mass and momentum for variable-density shallow water flows. Again, excellent agreement with semi-analytical models was achieved. The importance of the use of the Rouse number to determine the dominant transport mode has been highlighted.

The solution presented for the variable-density Riemann problem in Chapter 3 has been verified against a dam break over a mobile bed. Excellent agreement with an extensively-validated model in the literature confirms that the use of the solution to the Riemann problem for the unbalanced depth-discharge formulation

of the governing equations can be successfully extended to the well-balanced, stage-discharge formulation.

The numerical solver will now be used to model high-quality laboratory based experiments of complex dam break flows over fixed and mobile beds.

Chapter 5

Validation Test Cases for Water-Sediment Transport

5.1 Introduction

The model validation tests were carefully selected to test the scheme's ability to reproduce accurately the complicated flow field after a dam or dyke breach over fixed wet and initially-dry beds, and wet mobile beds. The first case was presented by Stelling and Duinmeijer (2003) and subsequently modelled using finite volume schemes by several authors, including Liang *et al.* (2004). It investigates a dyke breach over an immobile, wet or initially-dry bed. The second set of experimental results were described by Soares-Frazão *et al.* (2012) as part of the NSF-Pire project, obtained from a laboratory based study of a partial dam breach over a coarse-grained mobile bed in the Hydraulics Laboratory, Université Catholique de Louvain, Belgium. The third case is based on a case modelled by Xia *et al.* (2010) of an experiment carried out in Tsinghua University, China, of a partial dam breach over a mobile bed composed of fine sand.

5.2 Case 10: Partial Dam Breach in a Rectangular Laboratory-scale Basin with Non-erodible Bed

Figure 5.1 presents the layout of an experiment carried out by Stelling and Duinmeijer (2003) who investigated a dam breach flood into a basin with a flat, horizontal bed, 28.9 m long and 8 m wide, in the Fluid Mechanics Laboratory of Delft University of Technology, the Netherlands. This test was subsequently modelled numerically using finite volume schemes by Liang *et al.* (2004), Liang *et al.* (2006), Cui *et al.* (2010), and Li *et al.* (2013b).

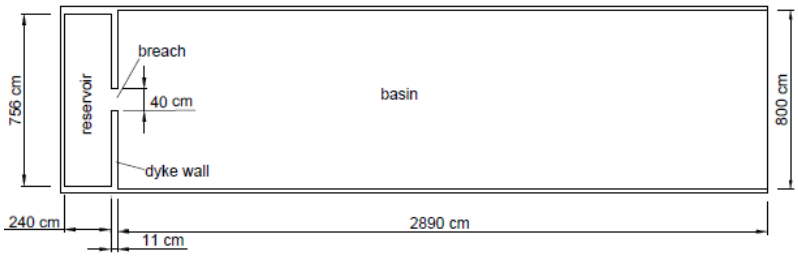

Figure 5.1: Plan view set up of the laboratory basin, Delft University of Technology

The reservoir upstream of the dam wall initially contains still water of depth 0.6 m. The section of the basin downstream of the wall is initially set either to be dry or to contain still water 0.05 m deep. At time $t = 0$ s, a sluice gate, 40 cm wide, located in the centre of the dam commences opening at a speed of 0.16 ms^{-1}. For comparison purposes, Manning's roughness coefficients $n = 0.012$ $sm^{-1/3}$ for the wet-bed case, and $n = 0.01$ $sm^{-1/3}$ for the dry-bed case are chosen following Stelling and Duinmeijer (2003). The computational domain is discretised on a uniform mesh of square cells, each of length $\Delta x = \Delta y = 0.078$ m. The time step, Δt, is set to 0.01 s for the initially wet basin and 0.001 s for the initially dry basin, in order to ensure stability. Slip boundary conditions are imposed at all of the walls, except at the outflow; an open, transmissive boundary.

Because the dam was not removed instantaneously, and the gate was opened relatively slowly in the laboratory tests, the computation of discharge and water depth is modified at the gate inflow cells for the initial gate opening stage. When

the vertical opening height, h_g, is less than the water level in the reservoir, the gate is taken to be a solid wall, and the water depth flowing through the gate is set to h_g. The flow discharge passing through the gate per unit width, Q (m/s) is then calculated using the following hydraulic formula for submerged culvert flow:

$$Q = C_c h_g \sqrt{2g(h_1 - C_c h_g)} \,, \tag{5.1}$$

where C_c is the contraction coefficient accounting for the combined effect of the vertical and horizontal contractions, and h_1 is water level in the reservoir. The value of C_c, normally taken as 0.6 for a culvert with square edges, is modified to 0.9 and 0.8 for the wet and dry-bed cases respectively, following Liang *et al.* (2004), and after numerical trials. The value of C_c is altered from the standard value of 0.6 because the opening in the dam wall is very small with respect to the width of the reservoir.

5.2.1 Dam Breach over a Wet-bed

Figure 5.2 shows predicted free surface elevation distributions and contours at t = 4 s and t = 18 s for flow over the wet downstream bed. Initially, the high-velocity jet emanating from the sluice causes the water to spread laterally as well as causing the bore to propagate downstream from the gate. This results in a symmetrical, almost semi-circular wave front propagating away from the gate. The bore is followed by a rarefaction wave which is pushed downstream by the high discharge emanating from the gate. At t = 4 s (Figure 5.2a), the primary bore wave reaches the sides of the channel and is reflected back into the channel. The reflected waves interact with a water plateau behind the bore front, resulting in the formation of an increasingly complicated wave pattern, symmetric about the centre of the channel, y = 0 m. The interaction of the reflected waves and the bore front also results in the formation of a Mach stem which causes the primary bore front to become uniform across the basin by t = 18 s (Figure 5.2b). By this time, the rarefaction wave behind the bore is held almost stationary, about 5 m downstream of the gate, by the supercritical flow issuing through the sluice.

Meanwhile, the wave pattern becomes increasingly complicated with time, due partly to side wall interactions. A full description of the flow physics is given by Liang *et al.* (2004).

In Figure 5.3, the positions of the bore front obtained from the numerical model and laboratory experiments are superimposed at $t = 1$ s, 2 s, 3 s and 4s. When the inflow is modified to account for the slow opening of the gate, as described above, the propagation speed of the bore in the numerical model is in excellent agreement with the numerical results, as seen in Figure 5.3(a). For comparison purposes, the bore position is plotted in Figure 5.2(b) if the gate is removed instantaneously in the numerical simulation. It is evident that the initial propagation speed of the bore front in this case is faster than the laboratory experiments, highlighting the sensitivity of the numerical model results to the boundary conditions imposed at the inflow.

Time history plots of the free surface elevation at four locations along the centreline of the basin are presented in Figure 5.4 for both scenarios; when the inflow condition is modified to account for the gate opening, and when the dam breach is modelled as instantaneous. Despite the better agreement between laboratory data and numerical results for the bore front location when the gate is opened slowly (Figure 5.3a), it is observed clearly in Figure 5.4 (a & b) that modifying the inflow affects the free surface elevation close to the gate significantly, particularly during the initial stage of the numerical simulation. At the gauge located 1 m downstream of the dam wall (Figure 5.4b), the magnitude of the initial bore elevation is lower when the gate is opened slowly (at ≈ 1 s), as expected. However, after the primary bore front has moved further downstream, and up until $t \approx 4$ s, the free surface elevation is overestimated when the breach is not instantaneous. For $t > 4$ s, after which time the gate is fully open in both scenarios, the discrepancy between the results is greatly reduced.

From Figure 5.4, it is evident that the results of the free surface elevation are most sensitive to inflow conditions immediately downstream of the dam breach, during the initial seconds following the rupture. Further downstream, free surface elevation profiles are less affected by initial inflow conditions. These results underline the difficulty of modelling complex, supercritical dam break flows using

the depth-averaged shallow-water equations, particularly for the region close to the dam wall during the initial seconds following the dam break, when the vertical velocity component of the flow is significant at this location. The results presented in Figures 5.3 and 5.4 underline the care required when choosing the appropriate inflow boundary conditions, and in interpreting the corresponding numerical results, the latter of which should always be done with consideration for the limitations of the particular numerical solver, in this instance the limitations of the depth averaged scheme. However, these results confirm that the shallow water equations can be used for successful modelling of complicated dam break flows, provided that the initial seconds following the dam breach are interpreted with care. Although this test case does not include sediment, the difficulties involved in modelling the initial hydrodynamics following a dam breach could have a significant impact on the final bed profiles if the downstream bed is erodible. This is discussed in further detail in Section 5.2.3.

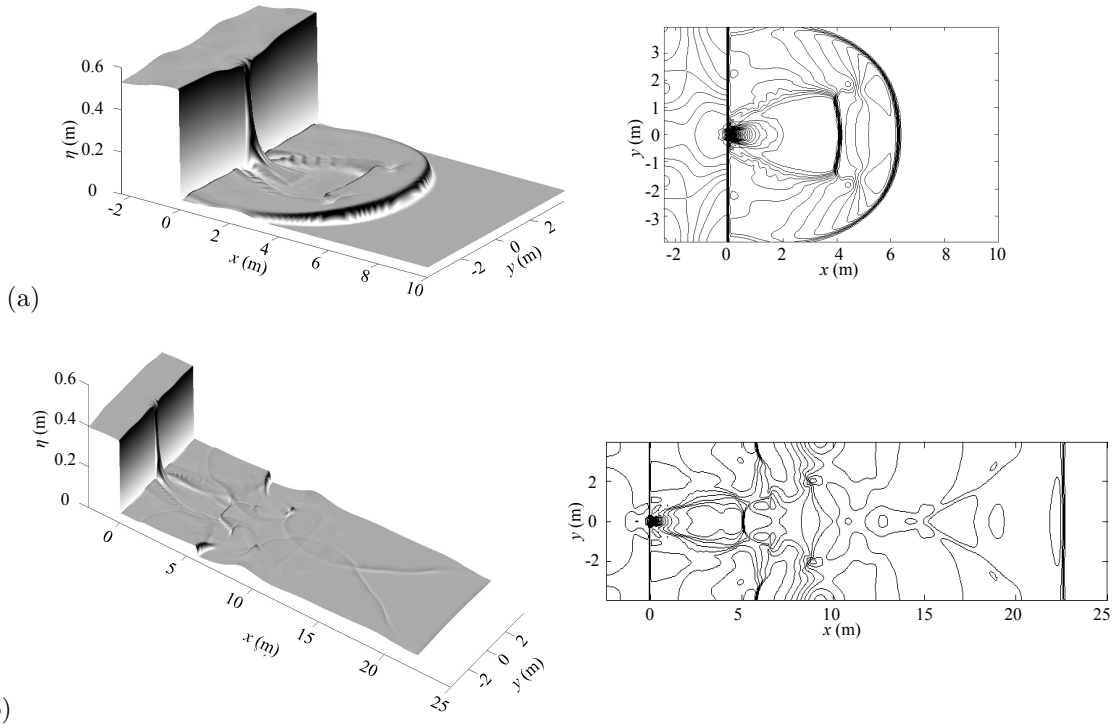

Figure 5.2: Delft University of Technology wet-bed partial dam breach: surface and contour plots at (a) $t = 4$s and (b) $t = 18$s.

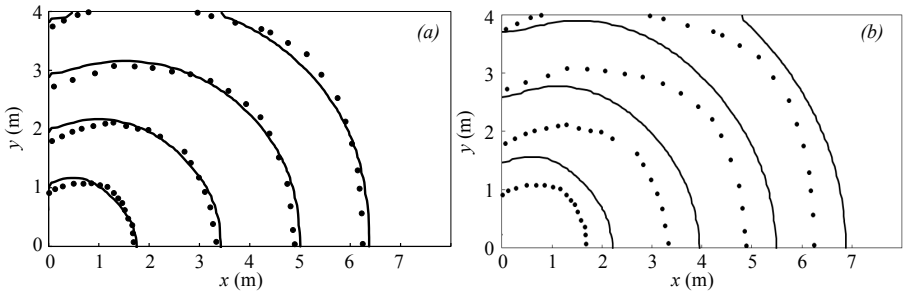

Figure 5.3: Delft University of Technology wet-bed partial dam breach: bore front locations at $t = 1$ s, 2 s, 3 s and 4 s; laboratory data from Stelling and Duinmeijer (2003) (dotted line) and present numerical model (solid black line) for two cases; (a) slow gate opening included in numerical predictions, and (b) gate removed instantaneously at $t = 0$ s.

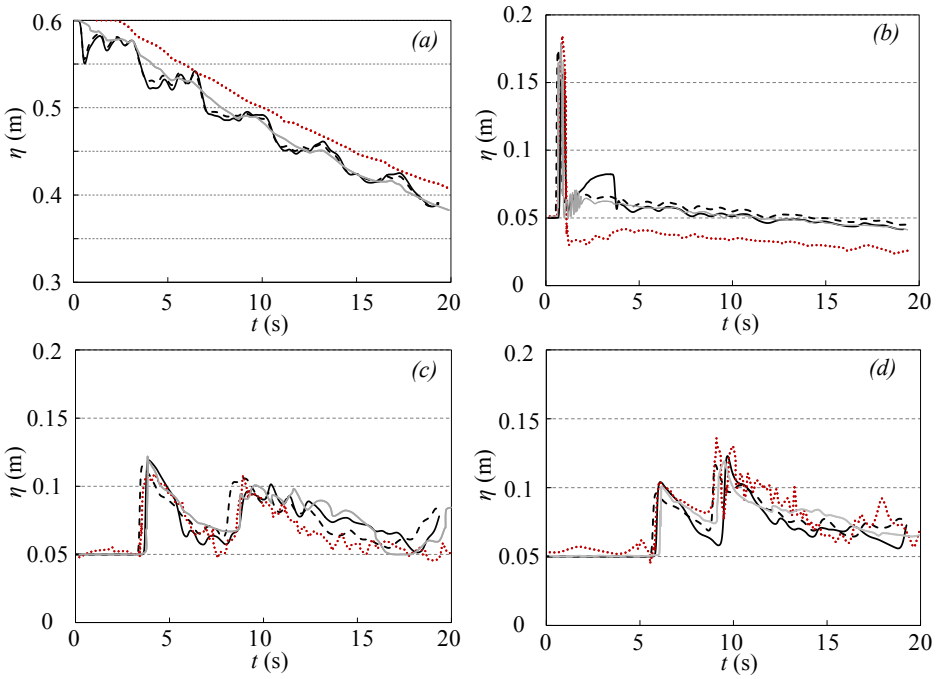

Figure 5.4: Delft University of Technology wet-bed partial dam breach: time history plots at different gauge locations, -1 m, 1 m, 6 m, 13 m from gate, along the centre of the basin for laboratory data (red dotted line), numerical model of Stelling and Duinmeijer (2003) (grey line) and present numerical model; solid black line - inflow modified using (5.1), dashed black line - instantaneous dam breach.

5.2.2 Dam Breach over a Dry-bed

As mentioned briefly in Chapter 4, to compensate for the lack of a wetting and drying algorithm required for flow over initially-dry, sloping or rough beds, a very thin layer of water is used to represent the initially-dry downstream bed test

case. The 'dry' downstream basin is covered with water of depth, $h = 1 \times 10^{-5}$m. Similarly to the frictionless rectangular dam breach (see Section 4.1.3), when the downstream basin is initially dry, the bore front propagates downstream at a higher velocity than in the initially wet-bed case, but the bore does not expand as much laterally in the early part of the simulation (Figure 5.5a). A rarefaction wave is not evident in the dry-bed case; however, a water plateau forms between the bore front and the dam wall. As in the wet-bed case, after the circular bore front has reached the channel sides, the reflected waves, propagating towards the centre of the channel, begin to interact with the bore, causing the bore front to straighten. By $t = 18$ s (Figure 5.5b), the interaction of the reflected waves in the centre of the channel approximately 10 m from the gate results in the formation of a symmetric, free surface pattern. The results are in excellent agreement with the numerical results presented by Liang *et al.* (2004), included in Figure 5.5a, who used an extensively-validated shallow-water model and a quadtree grid.

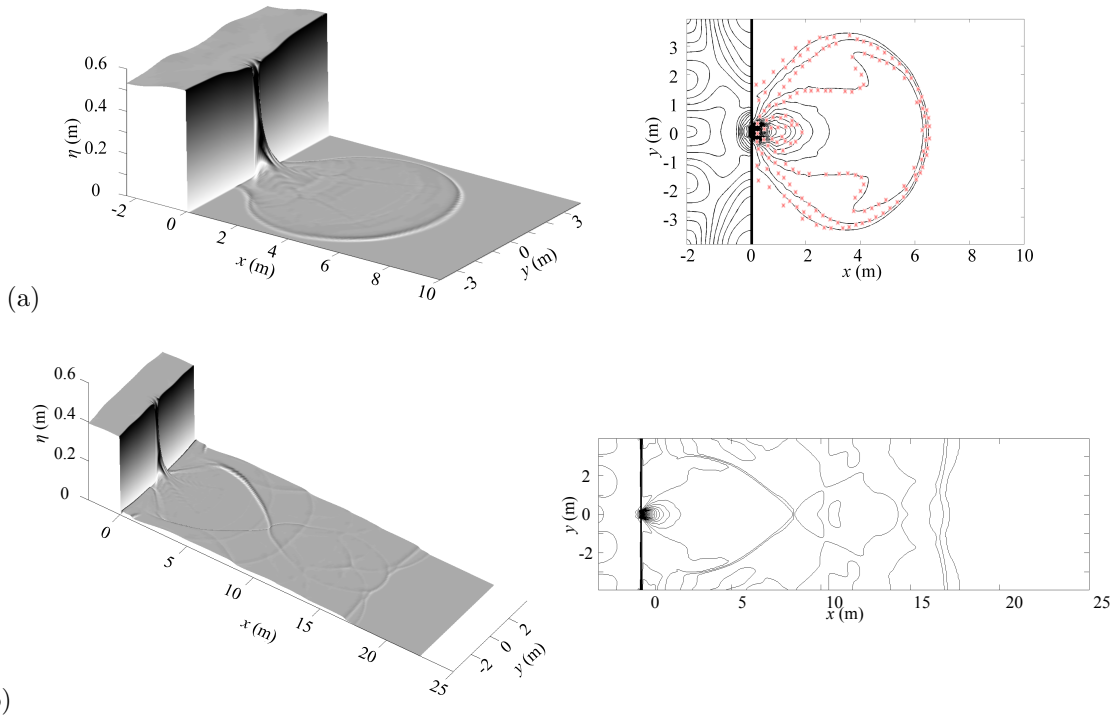

Figure 5.5: Delft University of Technology dry-bed partial dam breach: surface and contour plots at $t = 4$s and $t = 18$s.

The locations of the bore front, presented in Figure 5.6, at $t = 1$ s, 2 s, 3 s, and 4 s, are in satisfactory agreement with the laboratory data. As is observed for the wet-bed case, the speed of the bore front is much faster in the numerical

simulation than in the physical experiment if the breach forms instantaneously at $t = 0$ s, but the difference is more significant for the dry-bed case, as seen clearly in Figure 5.6.

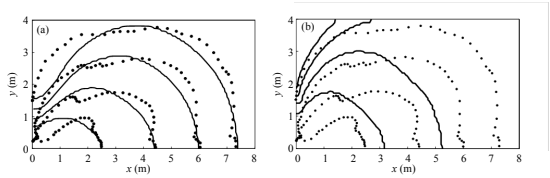

Figure 5.6: Delft University of Technology dry-bed partial dam breach: bore front location at $t = 1$ s, 2 s, 3 s and 4 s; laboratory data from Stelling and Duinmeijer (2003) (dotted line) and present numerical model (solid black line); (a) slow gate opening included in numerical predictions, and (b) gate removed instantaneously at $t = 0$ s.

Figure 5.7 presents the time history plots of the free surface elevation at different gauge points for both scenarios; instantaneous removal of the dam wall and slow lifting of the gate. The results of the initially 'dry' bed case appear to be more sensitive to the inflow boundary conditions than in the wet-bed case. This is because the water depths are a factor of 10 smaller in this case; a small absolute difference in the results appears as a large relative difference between numerical simulations, particularly evident in Figure 5.7(b). Similarly to the wet-bed experiment, the largest discrepancies between the present numerical results and the laboratory-based data are observed at the gauge nearest to the dam wall, in the first 4 s seconds following the breach (Figure 5.7b). Again, this is the region where the shallow-water approximations are likely to deviate from the physical experiment because the vertical velocity component is non-negligible, and the curvature of the free surface profile does not strictly conserve hydrostatic pressure, as is assumed in the derivation of the governing equations. However, at all other gauges, and for $t > 4$s, the numerical results are in satisfactory agreement with the experimental results. It is also interesting to note that, in Figures 5.4(a) and 5.7(a), more fluctuation is observed in the free surface elevation in the numerical model than in the laboratory-based data. These exaggerated free surface variations were also observed by other authors, including Stelling and Duinmeijer (2003), Liang *et al.* (2004), and Li *et al.* (2013b), and could be a result of the difficulty in modelling supercritical flow through the narrow gate

and reflections observed in the reservoir in the numerical model.

Allowing for the above discrepancies and the well-known limitations of the shallow water equations for modelling the initial seconds following a dam breach, the overall results obtained by the present numerical model are in close agreement with the numerical results obtained by Stelling and Duinmeijer (2003) and Liang *et al.* (2004), and in good agreement with laboratory-based data for the wet-bed and 'dry'-bed cases, shown in Figures 5.2 and 5.4, and Figures 5.5 and 5.7.

Although this test case does not consider sediment transport, the geometry of the experiment is similar to Section 5.2.3, a dam breach over a mobile bed. The hydrodynamics presented above will be exploited to explain qualitatively the final bed topography of Section 5.2.3.

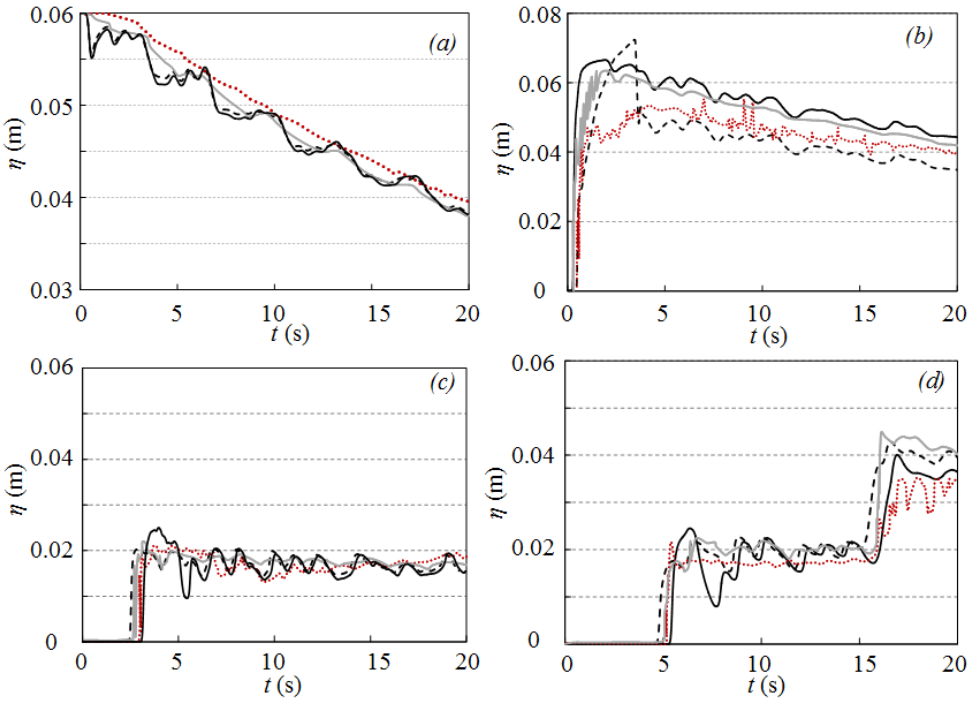

Figure 5.7: Delft University of Technology dry-bed partial dam breach: time history plots at different gauge locations, -1 m, 1 m, 6 m, 13 m from gate, along the centre of the basin for laboratory data (red dotted line), numerical model of Stelling and Duinmeijer (2003) (grey line) and present numerical model; solid black line - inflow modified using (5.1), dashed black line - instantaneous dam breach.

5.2.3 Case 11: Experimental 2D Dam Break over Mobile Ded

This test case considers a 2D dam break experiment conducted in the Hydraulics Laboratory, Université Catholique de Louvain, within the framework of the NSF-Pire project (Soares-Frazão *et al.*, 2012). The flume was 3.6 m wide and had a test length of approximately 27 m. A 1 m wide dam breach, induced by rapidly lifting a gate located at $x = 0$ m (Figure 5.8), modelled numerically as an instantaneous breach, created a laterally and longitudinally expanding wave. The mobile bed, initially 0.085 m deep, was spread 1 m upstream and 9 m downstream of the dam wall. In the rest of the flume, the horizontal, flat bed was fixed. The sediment had a median grain size $d = 1.61$ mm and relative density $s = 2.63$. The mobile bed porosity $\varepsilon = 0.42$. The Manning coefficient was estimated as $n = 0.0165$ sm$^{1/3}$ for the mobile bed and $n = 0.01$ sm$^{1/3}$ for the fixed bed. The initial water level was 0.51 m upstream and 0.15 m downstream of the gate. The experiment was run for 20 s, after which time the gate was closed and the flow stopped. At 8 gauge locations (see Figure 5.8 and Table 5.1) the water level was measured every 0.1 s for the 20 s duration using ultrasonic gauges. The final bed elevation was then measured from $x = 0.5$ m to $x = 8$ m every 0.05 m (Figure 5.10).

The computational domain is discretised on a uniform mesh of square cells, each of length $\Delta x = \Delta y = 0.05$ m, with the time step $\Delta t = 0.01$ s to ensure stability. Slip boundary conditions are imposed at all walls, with an open, transmissive boundary at the outflow. Bedload is the dominant mode of transport. Two numerical tests were run using different closure relationships for sediment transport, CB1 and CB2. In CB1, the entrainment and deposition coefficients E and D, are set to zero, and (2.19e) reduces to a traditional Exner-type bed morphology equation, where the bedload discharge is calculated using the Meyer-Peter-Mueller formula (2.22). For CB2 and CB3, the bedload discharge components q_{bx} and q_{by} are neglected and E and D are used to model the sediment transport using (2.29) for entrainment and deposition, respectively, such that,

$$E = \alpha_d w_s c_{eq}, \quad D = \alpha_d w_s c, \tag{5.2}$$

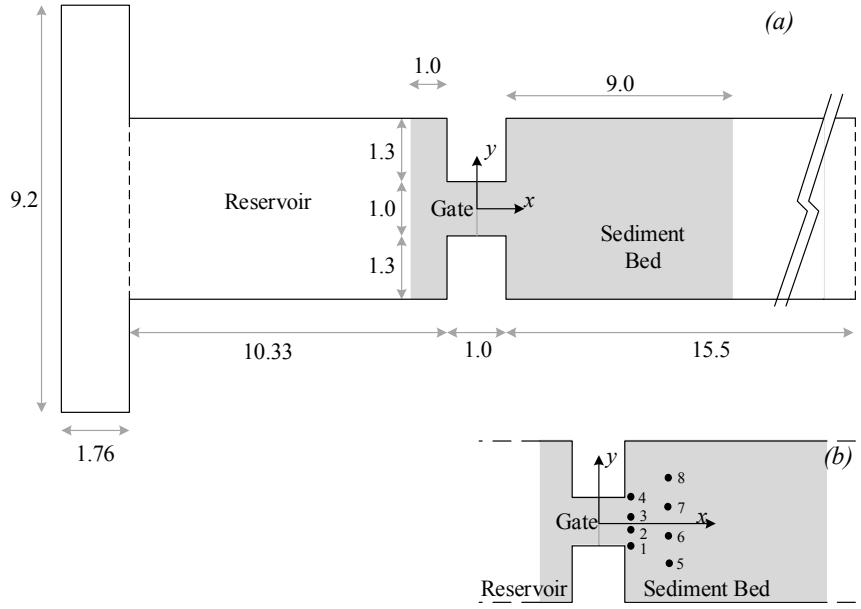

Figure 5.8: Plan view of (a) the experimental set up and (b) the location of the water depth gauges for the 2D partial dam breach experiment at the Université Catholique de Louvain (UCL Soares-Frazão *et al.*, 2012). All distances given in m.

where, α_d is calculated using (2.30) and c_{eq} is calculated using (2.32). In CB2, the modification factor $\phi_e = 1$. In CB3, $\phi_e = 2$ is chosen to account for the fast, transient flow observed during the dam breach experiment.

Gauge	x (m)	y (m)
US1	0.640	-0.500
US2	0.640	-0.165
US3	0.640	0.165
US4	0.640	0.500
US5	2.340	-0.990
US6	2.340	-0.330
US7	2.340	0.330
US8	2.340	0.990

Table 5.1: Université Catholique de Louvain partial dam breach experiment: gauge locations for recording the flow depth in the flume.

These two cases are used to validate the accuracy of the numerical solver, to investigate the uncertainty which lies in the choice of closure relationships and to highlight the importance of using fully-coupled solvers to model accurately the interaction between highly unsteady flows and sediment transport.

Figure 5.9 compares the free surface elevation time histories for cases CB1

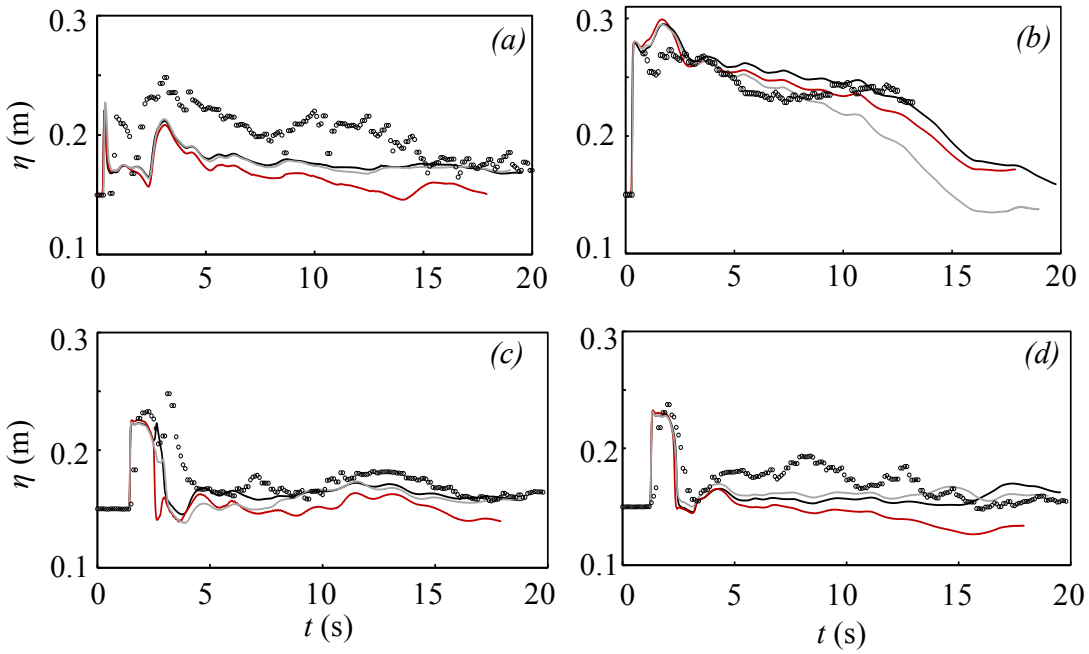

Figure 5.9: Université Catholique de Louvain partial dam breach experiment: free surface elevation profiles for; the experimental results (circles), CB1 (red solid line), CB2 (black solid line), and CB3 (grey solid line) at gauge locations: (a) US1, (b) US2, (c) US5, and (d) US6.

and CB2 with the measured results. Noting that the numerical model results are symmetric about $y = 0$ m, results at Gauges 1, 2, 5 and 6 are shown in Figure 5.9. In both cases, there is satisfactory agreement between the numerical predictions and the experimental data; in particular the celerity and amplitude of the bore front are well captured at all gauges, although there are some discrepancies at US1, located at the corner of the dam wall. A similar finding was reported by Swartenbroekx *et al.* (2013), who noted that the 2D depth-averaged model is unable to account for the turbulent shear stresses due to the vertical wall at the corner, which would act to slow down the flow, as observed in the laboratory experiment results. Similarly to Test Case 5.2.1 (Figure 5.4b), the free surface profile is overestimated in the numerical model immediately downstream of the dam opening (location US2). Both CB1 and CB2 yield almost identical results at $t < 5$ s. This validates the assumptions described previously in Chapter 2 in using (5.2) to model scenarios which are considered to be dominated by bed-load transport; choosing the appropriate closure relationship for c_{eq} ensures that the depth-averaged concentration of suspended sediment remains small, and the hydrodynamics are not affected significantly by the change in mixture density.

However, after this time, the scour hole has evolved differently for the three cases, and this affects the free surface elevation. For $t > 5$ s, at US6 the predicted free surface profiles vary less than the measured free surface. From the contour plot of the final bed topography (Figure 5.10) it can be seen that a second scour hole has formed at US6 in the experiment which is not reproduced by either of the numerical models. The large variation in η observed at US6 in the laboratory (Figure 5.9d) can be attributed to the presence of this scour hole.

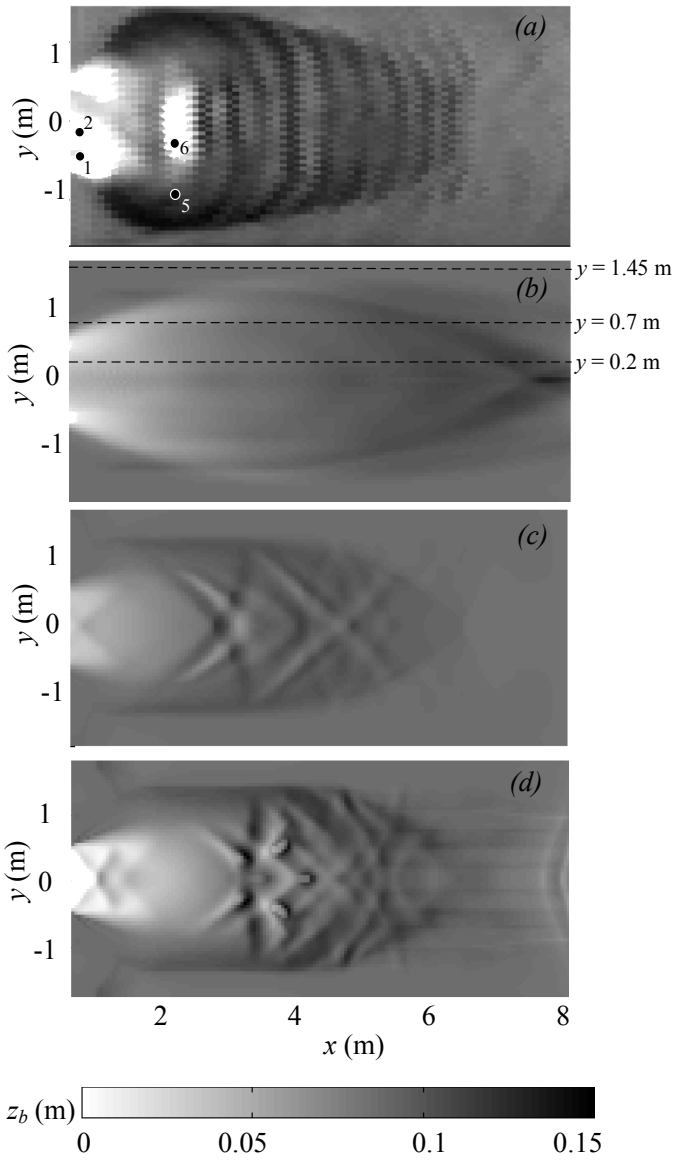

Figure 5.10: Université Catholique de Louvain partial dam breach experiment: final bed topography contours for (a) measured data, (b) CB1, (c) CB2, and (d) CB3. Black dots in (a) indicate locations of the water gauges; US1, US2, US5, and US6. Dashed lines in (b) indicate the locations of the bed profiles shown in Figure 5.11.

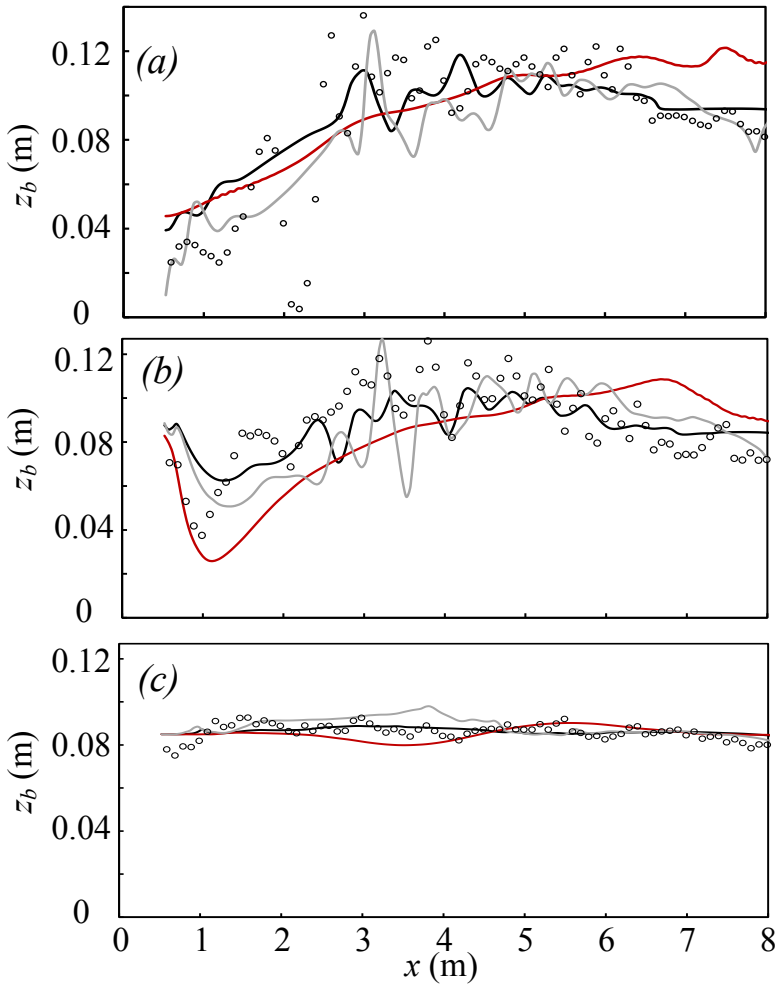

Figure 5.11: Université Catholique de Louvain partial dam breach experiment: final bed profiles from $x = 0.5$ m - 8.0 m; (a) $y = 0.2$ m, (b) $y = 0.7$ m, (c) $y = 1.45$ m; for measured data (circles), CB1 (red solid lines), CB2 (black solid line), and CB3 (grey solid line).

A prominent feature of the experimental results is the well-defined undulations in the final bed topography, seen in Figure 5.10(a). In the literature, the absence of bedforms in shallow water simulations of dam break flows which include bedload transport, is often attributed to the limitations of the depth-averaged equations which cannot account for vertical accelerations (see e.g. Capart and Young, 1998; Spinewine and Capart, 2013; Canelas *et al.*, 2013). Indeed, the vertical accelerations do impact scour formation and resulting bedforms, particularly immediately downstream of a dam break, where the vertical velocity component is a prominent feature of the flow (see for example, Capart and Young, 1998). It would be reasonable to conclude that the absence of this vertical velocity component in the shallow water model is largely responsible for the underestimation of

the first scour hole when comparing measurements and numerical results, as seen in Figures 5.10 and 5.11. There are, however, other physical mechanisms which could be responsible for the undulations seen further downstream, at $x > 2.5$ m. Notably, these bedforms appear to have very similar features to cyclic steps, formed during supercritical flow over an erodible, usually sloping, bed (see for example, Kostic *et al.*, 2010). Cyclic steps are widely observed in open channel

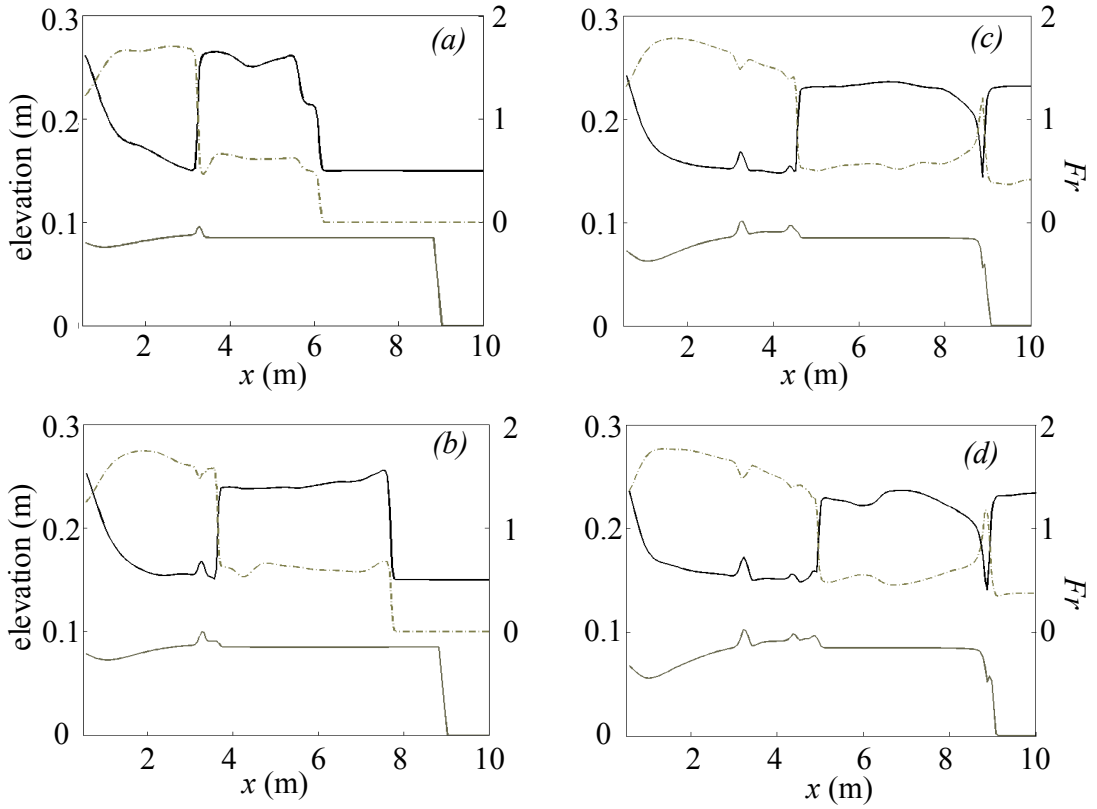

Figure 5.12: Université Catholique de Louvain partial dam breach experiment: spatial profiles of free surface elevation (solid black line), bed elevation (solid grey line), and Froude no. (dashed line), for CB2 at; (a) $t = 4$ s, (b) $t = 5$ s, (c) $t = 8$ s and (d) $t = 10$ s.

flows (Parker and Izumi, 2000). They are particular bedforms bounded by hydraulic jumps which develop because erosion dominates under fast supercritical flow and deposition occurs at the point of transition from supercritical to subcritical flow. Although no measurements were available for the bed morphology during the course of the experiment, the process of erosion and deposition which produces cyclic steps, well-described by Kostic *et al.* (2010), is clearly visible in the time history spatial profiles for CB2 in Figure 5.12. A well-defined hydraulic jump propagates downstream at the location where the rarefaction wave, associ-

ated with the primary bore front, meets the high-velocity flow emanating from the dam breach. Similar hydrodynamics were previously described in the discussion of Test Case 5.2, Figure 5.2. Sediment entrained by the fast supercritical jet emerging from the dam, seen in the deepening of the scour hole at $x < 3$ m over time, is deposited immediately downstream of this hydraulic jump, forming a hump in the bed profile. Because the hydraulic jump is pushed downstream by the high-velocity jet, the process of deposition is repeated downstream, forming a series of bed-humps. In Figure 5.12 it can be seen that the bedforms induce waves in the free surface, which sustain the bedforms allowing them to increase in size with time. Previously, cyclic steps have been reproduced successfully by several researchers using 1D shallow-water models coupled with the appropriate relations for D and E (e.g. Sun and Parker, 2005; Balmforth and Vakil, 2012). To the author's knowledge, this process has not been well documented for more complex 2D shallow-water flows but merits future investigation.

Although in CB2 use of the formulation proposed by Cao *et al.* (2010) does predict satisfactorily the undulated bed profile along the centre of the channel (see Figure 5.11a), from Figure 5.10, it is clear that the bedforms in the numerical model do not have the same planar shape as those observed in the laboratory. Rather, the final bed topography in CB2 follows a diagonal pattern (Figure 5.10c), mirroring the complex free surface behaviour which develops due to the interactions of the bore with the flume walls, as seen in more detail in Test Case 5.2.1 (Figure 5.2). It is likely that additional momentum would have been removed from the flow to create the deeper scour hole formed at $x \approx 1$ m in the physical experiment. As a result, the intensity of the reflections of the bore front and side walls would have been reduced, which could have resulted in a more unidirectional flow, allowing for the hydraulic jump to spread across the entire channel width, as opposed to taking up the diagonal form seen in the numerical simulations. Because sediment deposition is directly related to the free surface pattern, and the resulting bed morphology strongly impacts the hydrodynamics (see Figure 5.12) a small discrepancy in the initial free surface pattern could significantly affect the final bed topography. This hypothesis is supported further when analysing the final bed topography of case CB3, (see Figure 5.10d) where a larger modification

coefficient, $\phi_e = 2$ is used. It can be seen in Figure 5.10(d) that the deeper scour hole immediately downstream of the breach affects the final bed topography further downstream. Although the undulations simulated in CB3 are less planar in shape than the final laboratory measurements, the diagonal shape is reduced somewhat when compared to CB2, Figure 5.10(c).

Soares-Frazão *et al.* (2012) note that bed undulations were not captured by most of the shallow water models in the initial NSF-Pire project, although certain models which used a very fine mesh ($\Delta x = 0.02$ m) did reproduce qualitatively some of the bedforms. Interestingly, the latter models used either two-layer depth-averaged schemes with closure relationships for sediment transport based on the local bed shear stresses (for example Swartenbroekx *et al.*, 2013), or the formulation used in CB2 and CB3, which allows for local entrainment and deposition of particles (see Cao *et al.*, 2010). This is an important finding, reiterated in the present study, which encourages further research into refining the sediment transport model used in CB2 and CB3 and other such models which allow for local entrainment and deposition, even when bedload transport appears to be the dominant process. In a more recent study, Fourtakas *et al.* (2013) used a SPH model to simulate this test case. Fourtakas *et al.*'s results were in excellent agreement with the measured results, although at high computational cost.

In the absence of more detailed experimental measurements of the free surface elevation along the entire length of the erodible bed, as well as measurements of bed morphodynamics during the course of the experiments, the latter which are difficult to obtain in practice, the above explanation is not intended as an absolute description of the physical processes which occurred during the experiment. It is presented as a qualitative analysis of highly coupled water-sediment interactions and offers an alternative interpretation of the formation of bedforms under dam break flows.

One of the main conclusions of Soares-Frazão *et al.* (2012), through comparison of various numerical model results with the measured data, is that a major uncertainty in sediment transport modelling lies in the choice of empirical formulae and closure relationships. This is reiterated in the present work, where the final bed topography profiles vary significantly depending on the closure model

used, even though all other aspects of the numerical solver are identical in all cases. In addition, the present results suggest that oscillations observed in dam break flows over mobile, granular beds, cannot be attributed solely to vertical accelerations, often suggested in the literature (Capart and Young, 1998; Spinewine and Capart, 2013). Indeed, it appears that even when bedload transport dominates, under certain conditions, local erosion and deposition of particles may be responsible for the final bed morphology. In light of this, future numerical studies of bedload transport caused by dam break flows, which consider alternative approaches to the Exner-type equation, and admit local entrainment and deposition of particles, merit investigation.

This validation case highlights another advantage of this numerical model; it can be used to investigate a very wide range of sediment transport formulae, from the Exner-type equations for bedload transport, to the total load transport form of the sediment transport equations. Thus, it could be used for a large variety of engineering applications and different flow-sediment regimes, provided that care is taken when choosing the appropriate closure relationships.

5.3 Case 12: Partial Dam Breach Flow over Partly-mobile Bed

The final demonstration case of water-sediment interactions is based on experimental results presented by Xia *et al.* (2010) of a partial dam breach flow over a partly erodible bed. The experiment was carried out in the Department of Hydraulic Engineering, Tsinghua University, China. Predictions by the present model are compared against the experimental measurements at Tsinghua University and results by an alternative finite volume approximate Riemann solver, reported by Xia *et al.* (2010).

The experiment was carried out in a rectangular flume, 18.5 m long, and 1.6 m wide, with an initially horizontal bed. A thin-walled dam, located 2 m downstream of the upstream wall of the basin, held back water, 0.4 m in depth in a reservoir. The initial water depth downstream of the dam was 0.12 m. The bed included a 4.5 m long tray filled with coal ash, commencing at the downstream

face of the dam wall, at $x = 2$ m (see Figure 5.13). Everywhere else the bed was constructed from non-erodible concrete. The initial surface elevation of both the erodible and non-erodible beds is set to 0 m in the numerical simulation. In the laboratory experiment, a 20 cm breach was opened abruptly in the centre of the thin-walled dam, at $t = 20$ s. The downstream boundary comprised an open overflow. The erodible bed region was made of coal ash, containing a range of 6 particle sizes, of median diameter $d = 0.135$ mm, mean density $\rho_s = 2248$ kg m^{-3} and porosity $\varepsilon = 0.68$ (Xia *et al.*, 2010).

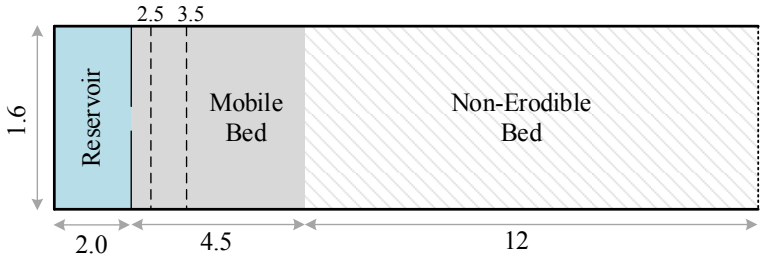

Figure 5.13: Plan view of the laboratory flume in Tsinghua University, China. All values shown in m.

The following numerical simulations concern a uniform bed, with particle diameter set to the median size. The Manning coefficient $n = 0.015$ sm$^{-1/3}$, following Xia *et al.* (2010). All boundaries are represented by a reflective, solid wall boundary condition, except for the downstream boundary which is open, transmissive. The model is discretised on a mesh with cell sizes $\Delta x = 0.01$ m and $\Delta y = 0.025$ m, and the time step, $\Delta t = 0.002$ s. The only data available from the laboratory experiment for comparison, are two final cross-section profiles of the bed level, at $x = 2.5$ m, and $x = 3.5$ m. Due to the lack of laboratory-based data, such as time histories of free surface elevation profiles, or final bed topography data along the entire plan area of the flume, this test case can be used only as a qualitative study. It poses an interesting case to investigate some of the features of fully-coupled, complicated water-sediment interactions, highlighting some of the challenges for shallow water-sediment modellers; but it cannot be used to validate the numerical model quantitatively. In this respect, two different scenarios are simulated numerically. The first case, TC1, represents the initial conditions noted above, with the reservoir water depth $h = 0.4$ m. In the second case, TC2, the upstream water depth is increased to $h = 0.6$ m. In both scenarios, D and E are

calculated using equations (2.24) and (2.28), respectively. The entrainment flux coefficient required in (2.28) $\alpha_e = 5 \times 10^{-6}$ in TC1, and $\alpha_e = 1 \times 10^{-6}$ in TC2. These values of α_e are selected to yield maximum erosion depths at $x = 2.5$ m similar to those observed in the laboratory experiment.

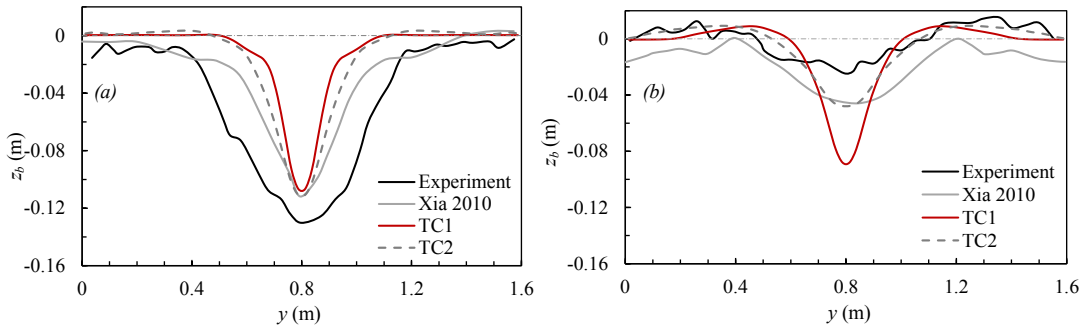

Figure 5.14: Tsinghua University dam breach experiment: final bed topography cross sections for TC1 and TC2 at; (a) $x = 2.5$ m, and (b) $x = 3.5$ m.

In Figure 5.14, the final bed-elevation cross-sections at $x = 2.5$ m and $x = 3.5$ m, are compared with the laboratory based data, and numerical results obtained by Xia *et al.* (2010), who used an alternative FV approximate Riemann solver. In the numerical simulations, lateral erosion is underestimated at $x = 2.5$ m. The underestimation of scour immediately downstream of the dam breach, especially in the lateral direction, was observed previously (Section 5.2.3). Once again, this is likely to result from the shallow water formulation, which is unable to simulate the vertical velocity component - a strong feature of dam breach flow, particularly in the initial seconds after rupture (see e.g. Cao *et al.*, 2004). Moreover, in the present test case, the ratio of the width of the dam breach to the flume width is much smaller ($\approx 12.5\%$), which would result in higher exit velocities, in both horizontal and vertical directions. Thus, the absence of vertical accelerations in the numerical simulations would provoke even larger discrepancies between observed and computed results than those observed in Section 5.2.3. When the entrainment coefficient, α_e for TC1 is selected to yield reasonable results for the maximum erosion depth at $x = 2.5$ m, it is seen in Figure 5.14(b) that further downstream, the scour hole is largely overestimated. Several values of α_e were investigated for TC1 and, regardless of the value of α_e, the ratio between the scour hole at the two locations was the same. In essence, although the magnitude of the erosion is affected by the value of α_e, it has no significant impact on the

general shape of the final bed topography. Due to the lack of laboratory data, it is not possible to determine the exact reason for the difference between observed and computed results. However, a comparison between the results of TC1 and TC2 will be used to explore the highly coupled flow-sediment interactions which could explain these results.

Figure 5.15 and Figure 5.16 present the numerical predictions of the bed elevation z_b and the streamwise flow velocity contours u, at $t = 1$ s, 5 s, 10 s, and 20 s, for TC1 and TC2, respectively. Noting that E is proportional to $|u|^3$, the contour plots of u are a good representation of the erosion rate along the flume. At $t = 1$ s, (Figure 5.15 - a, e, j), it is seen that a deep but narrow hole is eroded when the fast moving jet emerging from the breach impacts the erodible bed. In Figure 5.16 (a, e, j), the scour hole at this time is shallower, but significantly wider, than for TC1. This is because the value of α_e is 5 times smaller, in order to match with the experimental results. As the bore front moves downstream, at $t =$ 5 s, it may be observed that, in TC2, the magnitude of u remains locally elevated at $x \leq 2.5$ m but is approximately 30% lower further downstream (Figure 5.16 - j), i.e. the flow velocity reduces significantly downstream of the large scour hole at $x \approx 2.5$ m. Correspondingly, the local bed erosion is much greater at $x \approx 2.5$ m. After $t > 5$ s, u continues to reduce, with relatively elevated values observed at several locations along the centreline of the channel (Figure 5.16 - k, l), resulting in some erosion further downstream (Figure 5.16 - c, d, g, h). It is clear from Figure 5.16 that maximum erosion occurs at $x \approx 2.5$ m in the initial seconds following the dam rupture, as was seen previously in Figure 5.14 (a). Returning to Figure 5.15, the difference in magnitude between u at $x = 2.5$ m and $x = 3.5$ m is much less significant in TC1, particularly at $t = 5$ s and $t = 10$ s (Figure 5.15 - j, k); resulting in more uniform erosion along the length of the erodible section of the flume (Figure 5.15 - b, c, g, h).

One explanation for the differences observed between TC1 and TC2, and also for the better agreement between the results of TC2 and the experimental results, is that the exit velocity at the breach location is much higher for TC2, due to the larger head difference between the reservoir water level and the initial downstream basin water level. In particular, the radial component of the flow is

greater in TC2, resulting in a wider scour hole at $t = 1$ s (Figure 5.16 - a, e, i). The bed erosion removes momentum from the flow, thus reducing the flow speed. In Figure 5.16 (i), it is observed that the flow expands in the transverse direction downstream of the scour hole. This occurs because the downstream face of the hole acts as a bed step, or an 'obstacle' to the supercritical jet emerging from the breach. As the flow encounters this 'obstacle', a hydraulic jump is formed (seen by the sharp decrease in velocity at $x = 2.5$ m in Figure 5.16 - j), removing additional momentum from the flow. Simultaneously, the 'obstacle' resists flow in the streamwise direction, causing the flow to spread out in the lateral direction, further reducing the downstream velocity in the streamwise direction. In this sense, the higher velocity of the emerging jet in TC2 compensates for the absence of the vertical velocity component which would provoke significant erosion immediately downstream of the breach in the laboratory-based experiment.

The above description of the flow-mobile-bed interactions is compatible with observations from the previous test case in Section 5.2.3, where the maximum depth and the lateral erosion of the scour hole was underestimated by the present numerical model, and also by all of the shallow water models used in the initial study (see Soares-Frazão *et al.*, 2012). At the time of writing, it is the author's view that the discrepancy observed between the experimental and numerical results in Figure 5.14 primarily arises from the assumptions made in the derivation of the shallow water equations, which cannot account for the vertical velocity component, resulting in reduced scour immediately downstream of the breach. However, other secondary aspects are worth noting. Firstly, from Figure 5.14 it can be seen that the slope of the bed is greater than the angle of repose of sediment, $\varphi \approx 30°$. In the numerical model, no algorithm has been included to allow for bank failure in the transverse direction when the bed slope exceeds the submerged angle of repose of the sediment grains. The results in Figure 5.14 suggest that the addition of such an algorithm should be included in the shallow water-sediment model to improve the accuracy of the final results. Examples of such algorithms include those presented by Swartenbroekx *et al.* (2010) and Sun *et al.* (2015). Secondly, the numerical results presented here are for a uniform sediment grain size. However, even when several grain sizes were used, the re-

sults obtained were not affected significantly. This is because the shielding effect of the different grain sizes is not included explicitly in the model - a challenge to sediment transport numerical models. Lastly, much uncertainty still exists in the choice of closure relationships. As noted above, although the value of of the entrainment coefficient, α_e does affect the magnitude of bed erosion, α_e does not alter the shape of the final bed profile nor the ratio of the final bed levels at $x = 2.5$ m and $x = 3.5$ m. However, the final shape of the bed profile is sensitive to the formula selected to evaluate E. To investigate this, two alternative empirical formulae for E are investigated for TC1 ($h = 0.4$ m), both which use equation (2.29), combined with an empirical formula to estimate c_{eq} for suspended sediment.

In the first instance, TC1a, $\alpha_d = 4$ (required for (2.29)) and c_{eq} is calculated following Cao *et al.* (2012) such that:

$$c_{eq} = \frac{1}{20\rho_s} \frac{(u^3/ghw_s)^{1.5}}{1 + (u^3/45ghw_s)^{1.15}} \ , \tag{5.3}$$

where the symbols have the same meaning as given in previous chapters and in the Notation list.

In the second case, TC1b, the formula used by Xia *et al.* (2010) is selected;

$$c_{eq} = 0.452 \Big[\frac{\rho}{\rho_s - \rho} \frac{|u|^3}{ghw_s} \Big]^{0.762} \ . \tag{5.4}$$

Note that all of the above equations for E are a function of the average flow velocity $|u|^3$, the flow depth h, and the physical properties of the sediment grains. The results of the three cases, TC1, TC1a, and TC1b, are presented in Figure 5.17 and Figure 5.18. It can be seen that the final bed topography is greatly affected by the choice of closure relationship, although the lateral bed scour is always underestimated and the downstream scour hole is systematically overestimated, suggesting that the primary reason for the discrepancies given above is plausible.

It is noted that the differences between the observed and computed final bed elevation profiles do not result from errors in the discretisation technique estab-

lished in the model, which has been verified extensively in previous test cases. Instead the results highlight certain challenging aspects encountered in modelling complicated shallow water-sediment interactions. This study shows the obvious importance of using fully coupled numerical models because of the strong feedback that exists between the free surface elevation and the rapidly changing bed surface. There is a gap in the current literature of reliable test cases concerning rapidly varying, complex flows over mobile beds; particularly those beds comprising fine sediment for which the dominant mode of sediment transport is suspended sediment. In order to improve our understanding of the interaction of these processes, it is imperative to conduct more detailed experiments. In addition, many of the empirical formulae used to describe sediment transport are derived for less active sediment exchange between the water and the bed, and the present formulae may be unsuitable for rapidly-varied flow conditions.

5.4 Chapter Summary

In this chapter, numerical simulations have been presented of three laboratory-flume experiments. The results from the first test case have validated the accuracy of the numerical solver in capturing complicated 2D partial dam breach flows over fixed beds. The numerical simulation results for the propagation speed and amplitude of the bore front were in excellent agreement with the laboratory-based data. It has been demonstrated that the depth-averaged model results are sensitive to the inflow boundary conditions imposed. The subsequent test cases have considered complicated flows over a mobile bed. In the second test case, originally presented by Soares-Frazão *et al.* (2012), very satisfactory agreement was obtained for the flow hydrodynamics. The dominant mode of transport in this case was by bedload. The numerical simulations were able to predict with reasonable accuracy the final shape of the bed topography, however the fine details of the bedforms were not captured by the depth-averaged model. By comparing final bed topography results using different closure relationships for bedload transport, it was concluded that the traditional Exner-type bedload transport formula, which relates the bed morphology to the bedload discharge, may not be

appropriate for fast, transient flows. Instead, use of closure relationships which allow for local entrainment and deposition of sediment particles lead to the simulation of smaller bed forms to a greater degree of accuracy. Indeed, this merits future investigation. The final test case considered a partial dam breach flow over a partly erodible bed, consisting of fine particles, transported as suspended sediment. Only limited data were available for the comparison with numerical simulations. For this reason, it has not been possible to validate the flow hydrodynamics reproduced by the numerical model. However, this test case has highlighted the importance of using the fully-coupled water sediment equations for fast, supercritical flow over a mobile bed because of the strong feedback component between the bed morphology and the flow hydrodynamics. It has also been seen that the numerical results are quite sensitive to the choice of empirical formula used to estimate the entrainment flux. Some of the limitations of the shallow water models for simulating the erosion downstream of a dam breach have also been discussed. In particular, the depth averaged formulation of the equations has difficulty modelling the extent of scour immediately following the rupture, mainly due to the absence of vertical velocity components assumed in the derivation. Finally, with consideration for the above-stated, widely-known limitations of shallow-water models, it was shown that the numerical model presented here is well capable of modelling the global water-sediment interactions, and has proved to be an excellent tool for gaining insight into complicated shallow water-sediment interactions in highly unsteady flow conditions.

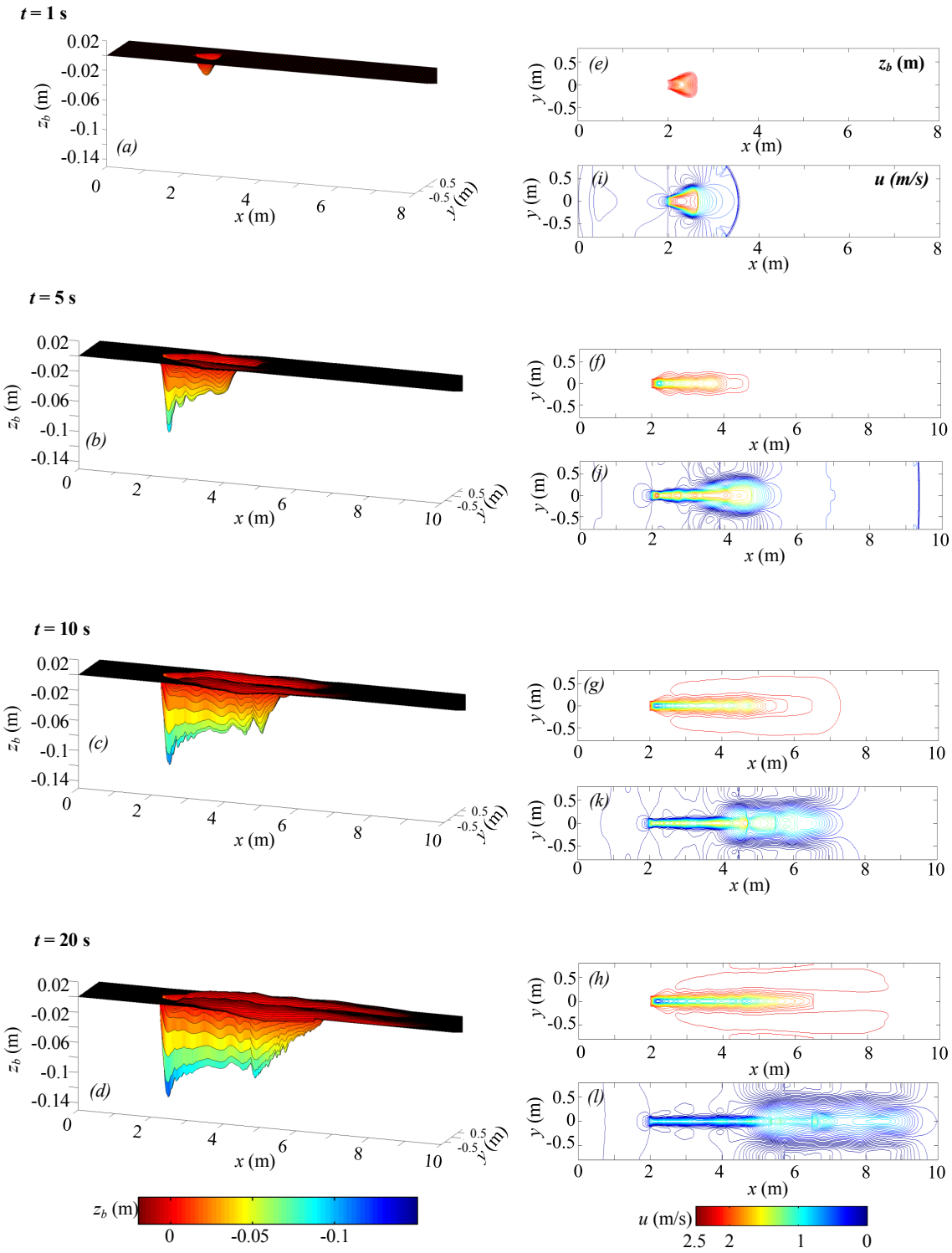

Figure 5.15: Tsinghua University dam breach experiment: bed elevation and streamwise velocity magnitude for TC1 ($\alpha_e = 5 \times 10^{-6}$; $h = 0.4$ m) at $t = 1$ s, $t = 5$ s, $t = 10$ s, and $t = 20$ s; (a) - (d) 3D visualisations; (e) - (h) contour plots of bed elevation z_b (m); (i) - (l) contour plots of the streamwise velocity magnitude u.

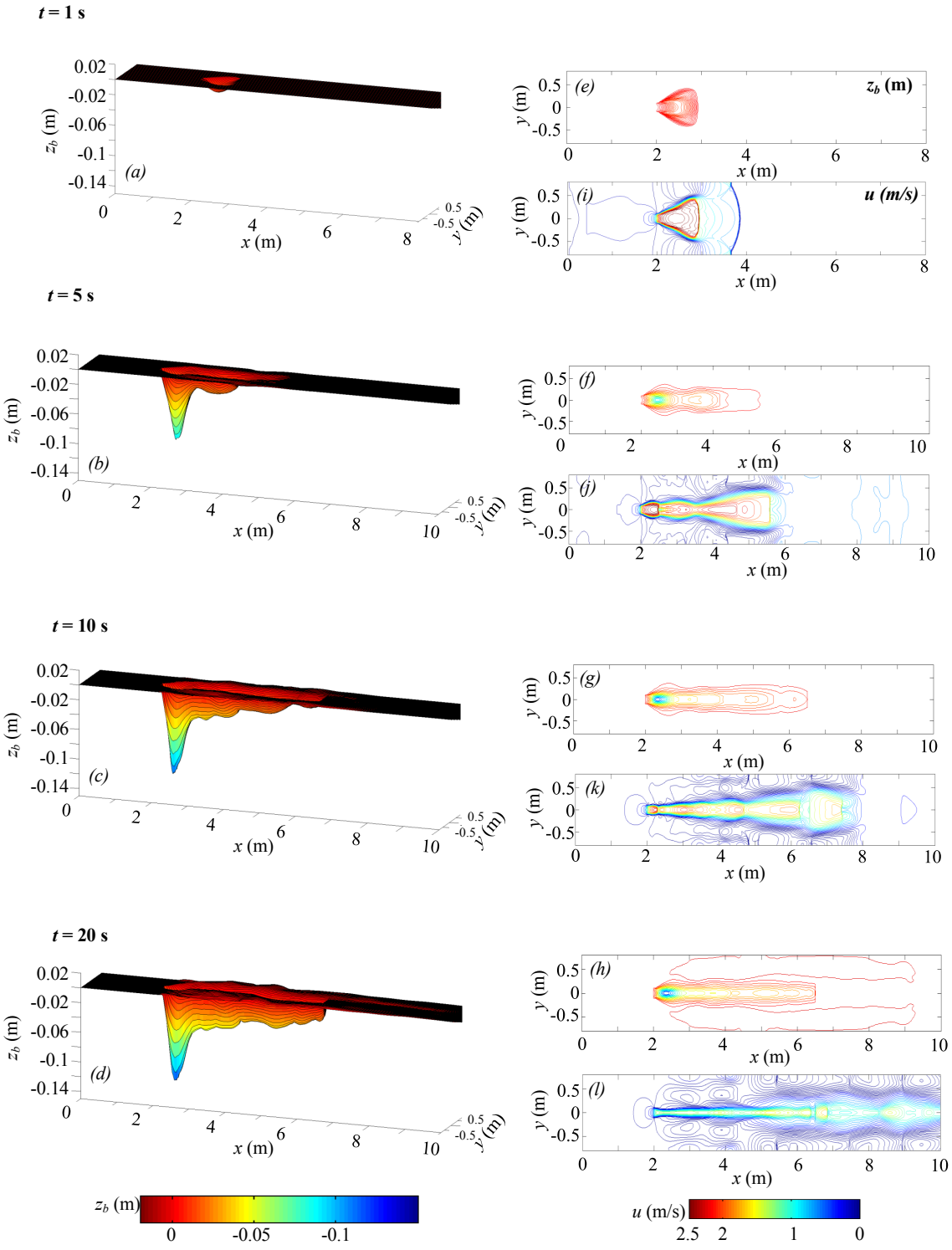

Figure 5.16: Tsinghua University dam breach experiment: bed elevation and streamwise velocity magnitude for TC2 ($\alpha_e = 1 \times 10^{-6}$; $h = 0.6$ m) at $t = 1$ s, $t = 5$ s, $t = 10$ s, and $t = 20$ s; (a) - (d) 3D visualisations; (e) - (h) contour plots of bed elevation z_b (m); (i) - (l) contour plots of the streamwise velocity magnitude u.

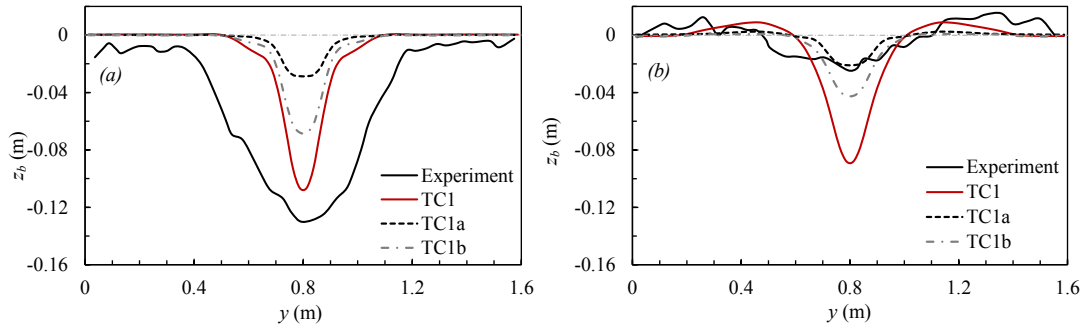

Figure 5.17: Tsinghua University dam breach experiment: final bed topography cross sections for TC1, TC1a, and TC1b at; (a) $x = 2.5$ m, and (b) $x = 3.5$ m.

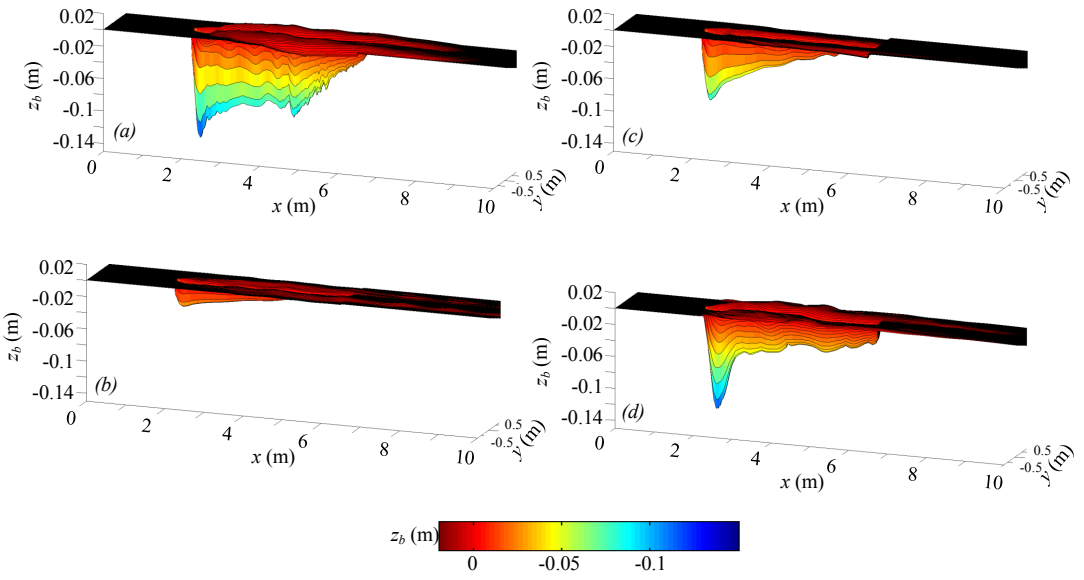

Figure 5.18: Tsinghua University dam breach experiment: 3D visualisation of final bed elevation, at $t = 20$ s, for; (a) TC1, (b) TC1a, (c) TC1b, and (d) TC2.

Chapter 6

Flow Through a Porous Obstruction in a Shallow Channel

In this chapter, the numerical model presented in Chapter 3 is used to inform a theoretical model developed to predict the flow passing through and around a uniform porous obstacle, represented as a patch of increased bed roughness, in a shallow channel, where background friction is important. This problem is relevant to a number of practical situations, including flow through aquatic vegetation, the performance of arrays of turbines in tidal channels and the hydrodynamic forces on offshore structures. To demonstrate this relevance, the theoretical model is used to (i) reinterpret the core flow velocities in existing laboratory-based data for an array of emergent cylinders in shallow water, and (ii) reassess the optimum arrangement of tidal turbines to generate power in a tidal channel.

6.1 Introduction

Consider a uniformly porous obstruction in a shallow channel. The obstacle, represented as a patch of increased bed friction, is located in the centre of the channel (Figure 6.1) and is assumed to be rectangular, with planar dimensions w and l, and compact, such that the aspect ratio $A_R = w/l \geq 1$. The channel is assumed to have uniform depth h_0, width W, and uniform flow with steady depth-averaged upstream velocity U. Natural bed resistance is introduced as a quadratic drag coefficient C_f, and the resistance of the obstruction is defined in

terms of the net drag of the individual constituent structures within the obstacle.

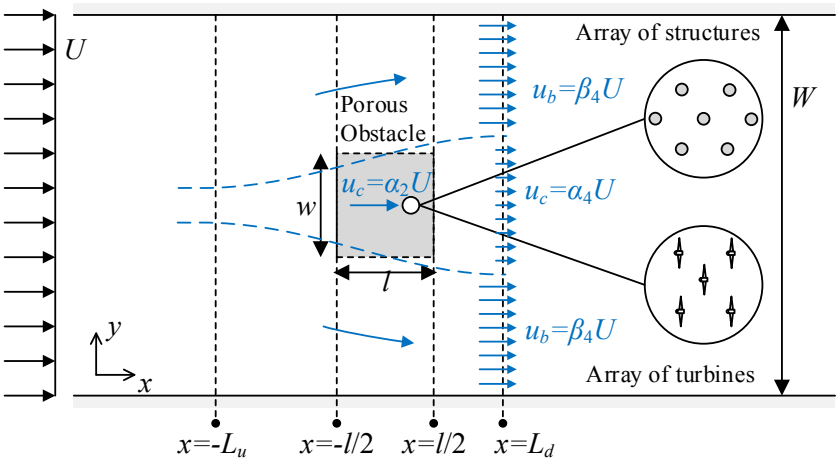

Figure 6.1: Plan view of a channel with a porous obstacle. Symbols and locations defined in Section 6.2.

Provided that h_0 is small (i.e. shallow) relative to the obstacle and channel dimensions, the usual approach is to use the shallow water equations to model this type of simplified problem. If the Froude number is small, it is then possible to show that three dimensionless parameters influence the core flow velocity, provided the obstacle is compact (i.e. $A_R >\sim 1$; see Section 6.3.2). These parameters are: (i) the porosity of the obstacle (or, equally, its dimensionless resistance k_p); (ii) $S = C_f w/h_0$, which explains the importance of natural drag and is often referred to as a stability number in the literature on shallow flow (Chen and Jirka, 1995); and (iii) the channel blockage ratio $B = w/W$. The stability number is a balance of the friction and inertia forces; as the value of S increases, vortices in the near wake are suppressed and the near wake stabilises. Collectively this set of three parameters defines a parameter space in which to explore the core flow passing through the obstacle, with the solution space having direct application to problems related to aquatic vegetation, offshore structures and tidal turbine arrays. To date however, as mentioned in Chapter 1, previous studies have only explored parts of the parameter space for this simplified problem, focusing on just one parameter (porosity) or two parameters (porosity and stability number or channel blockage ratio).

In the present chapter the solution for the depth-averaged core flow velocity passing through the porous obstacle in Figure 6.1 will be explored, accounting for the combined influence of porosity (or obstacle resistance), channel blockage and natural friction. To achieve this, an approximate theoretical model is developed, which extends conventional momentum theory for a porous obstacle in a finite channel to include background bed friction. It is shown that the inclusion of background friction introduces an additional unknown length scale. To close the theoretical model, numerical solutions based on the shallow water equations have therefore been performed, using the solver described in Chapter 3, to estimate this length scale over a practical range of S, B and k_p. To demonstrate the utility of the new theoretical model, it is then applied to two outstanding problems: firstly the prediction of the flow through a very porous patch of aquatic vegetation; and secondly the optimum arrangement of tidal turbines within a shallow tidal channel.

The theoretical model presented in this paper, and the numerical simulations performed to close the model, assume that depth-averaged shallow water equations are a satisfactory approximation to the flow field. With respect to this assumption, Stansby (2006) has described limitations to depth-averaged modelling in the near wake of a solid body in shallow water. Specifically, it has been shown that changes in velocity gradients and shear stresses near the bed, which result from horizontal and vertical mixing in the wake of the body, cannot be captured in a depth-averaged model (Stansby, 2003). This implies that a shallow water model may not capture the amplification in bed shear stress in the near wake of a solid body. Since this shear stress would act to resist flow through a porous obstacle, it also implies that a shallow water model is expected to over-predict the core flow velocity passing through the porous obstacle. In addition, Ball *et al.* (1996) found that an artificially high pile drag coefficient was required in shallow water numerical simulations to match the measured velocity profiles from experiments of flow through a group of piles. Ball *et al.* also showed that the ratio of the numerical drag coefficient (required to match the measured velocity) to the experimental drag coefficient increased as the porosity of the pile group decreased. In light of these earlier studies, the shallow water model is used

herein on the assumption that mixing and associated amplification of bed shear stress in the near wake of the obstacle is small. Comparison of the model results with experiments in 6.4.1 indicates the minimum obstacle porosities (maximum obstacle resistances) for which this assumption appears to be valid.

6.2 Theoretical Model

To develop an approximate theoretical model for the problem in Figure 6.1, a general form of the flow field is first assumed, and then arguments involving mass, energy and momentum conservation are used to relate the core flow velocity to the obstacle resistance in a similar way to that demonstrated by Garrett and Cummins (2007) for an obstacle in a frictionless channel.

Figure 6.1 illustrates the assumed flow field, which has two key features. Firstly the depth-averaged core and bypass flow, which are delineated by the dashed streamlines, are assumed to be uniform (i.e. one dimensional). Secondly, the dividing strealines are drawn as smoothly diverging lines, which implies that the depth-averaged core flow velocity $u_c(x)$ and the depth-averaged bypass velocity $u_b(x)$ vary smoothly and monotonically along the channel. Specifically, the core flow velocity reduces from the free stream velocity to $\alpha_2 U$ at the centre of the obstacle, before reducing further to a minimum velocity $\alpha_4 U$ in the near wake of the obstacle. Invoking continuity, the bypass flow velocity increases from the free stream velocity to a maximum velocity $\beta_4 U$ when the core flow is a minimum. The length scale over which these changes in core and bypass velocity take place is $L = L_u + L_d$, where L_u and L_d are the distances upstream and downstream of the obstacle where streamlines are close to parallel. Hence L_u is an upstream adjustment length using the terminology in Rominger and Nepf (2011), and L_d defines the distance from the centre of the obstacle to the near wake. The smooth variations in core and bypass flow velocities over these length scales are approximated by a cubic spline (as outlined below); it will be shown later in Section 6.3.1, that the use of a cublic spline agrees well with numerical simulations and laboratory based data.

6.2.1 Cublic Spline

To form the spline, two piecewise cubic polynomials are defined on the intervals $x \in (-L_u, 0)$ and $x \in (0, L_d)$. The first and second derivatives of these functions are set equal at $x = 0$, and the following constraints are applied:

$$u_c\left(-L_u\right) = U; \quad u_c\left(0\right) = \alpha_2 U; \quad u_c\left(L_d\right) = \alpha_4 U; \tag{6.1}$$

$$\frac{d}{dx}\left(u_c\left(-L_u\right)\right) = \frac{d}{dx}\left(u_c\left(L_d\right)\right) = 0\ . \tag{6.2}$$

This leads to the following cubic splines;

$$\frac{u_c}{U} = \begin{cases} a_1(x+L_u)^3 + b_1(x+L_u)^2 + 1; & -L_u < x < 0 \\ a_2(x-L_d)^3 + b_2(x-L_d)^2 + \alpha_4; & 0 < x < L_d \end{cases}, \tag{6.3}$$

where

$$a_1 = \frac{-3\left(\alpha_2 - \alpha_4\right)}{2(L_u L_d^2 + L_d L_u^2)} - \frac{\left(\alpha_2 - 1\right)\left(L_d + 4L_u\right)}{2L_u^2\left(L_u^2 + L_d L_u\right)}, \tag{6.4a}$$

$$a_2 = \frac{3\left(\alpha_2 - 1\right)}{2(L_d L_u^2 + L_u L_d^2)} - \frac{\left(\alpha_2 - \alpha_4\right)\left(L_u + 4L_d\right)}{2L_d^2\left(L_d^2 + L_u L_d\right)}, \tag{6.4b}$$

$$b_1 = \frac{3\left(\alpha_2 - \alpha_4\right)}{2(L_d^2 + L_d L_u)} + \frac{3\left(\alpha_2 - 1\right)\left(L_d + 2L_u\right)}{2L_u\left(L_u^2 + L_d L_u\right)}, \tag{6.4c}$$

$$b_2 = \frac{3\left(\alpha_2 - 1\right)}{2(L_u^2 + L_u L_d)} + \frac{3\left(\alpha_2 - \alpha_4\right)\left(L_u + 2L_d\right)}{2L_d\left(L_d^2 + L_u L_d\right)}. \tag{6.4d}$$

Given that $w_c u_c = w\alpha_2 U$ at $x = 0$, it follows that,

$$\frac{w_c}{w} = \frac{\alpha_2 U}{u_c} \ . \tag{6.5}$$

The width of the bypass flow is

$$w_b = W - w_c = \frac{w}{B} - w_c \ . \tag{6.6}$$

Therefore,

$$\frac{w_b}{w} = \frac{1}{B} - \frac{w_c}{w} \ . \tag{6.7}$$

Finally, from continuity, $(u_b w_b + \alpha_2 U w)h_0 = w h_0 U/B$. Hence the bypass flow velocity may be evaluated as

$$\frac{u_b}{U} = \frac{w}{w_b}\left(\frac{1}{B} - \alpha_2\right) \ . \tag{6.8}$$

6.2.2 Deriving the Theoretical Model

Based on the description of the flow field above, it is now possible to relate the velocity coefficients in the core and bypass flow to the obstacle resistance using conservation arguments. First, continuity between $x = -L_u$ and $x = L_d$ is used to write (see Houlsby *et al.*, 2008, for example)

$$\alpha_4 U w(\alpha_2/\alpha_4) + \beta_4 U w(1/B - \alpha_2/\alpha_4) = UW, \tag{6.9}$$

or, after rearranging,

$$\alpha_2 = \frac{\alpha_4(1 - \beta_4)}{B(\alpha_4 - \beta_4)}. \tag{6.10}$$

Next, the Bernoulli equation is written along any streamline passing through the obstacle, assuming unidirectional flow. Undertaking this separately upstream and downstream of the obstacle, and taking the difference, gives

$$p_{-l/2} - p_{l/2} = p_{-L_u} - p_{L_d} + \frac{1}{2}\rho U^2 \left(1 - \alpha_4^2\right) - \rho S \frac{L}{w} \int_{-L_u/L}^{L_d/L} u_c^2 \;\; d(x/L), \quad (6.11)$$

where ρ is the fluid density and the last term in (6.11) accounts for losses due to bed friction over the upstream and downstream regions of the core flow, respectively, and p_{x_i} represents the pressure at different locations x_i along the channel (noting that p is equal to ρg times the free surface elevation when the Froude number is small; see Garrett and Cummins, 2007). Strictly speaking the integral in (6.11) should omit the region within the obstacle; however it is assumed that this region is small when $A_R > 1$.

The Bernoulli equation can also be written along a streamline in the bypass flow, leading to

$$p_{-L_u} - p_{L_d} = \frac{1}{2}\rho U^2 \left(\beta_4^2 - 1\right) + \rho S \frac{L}{w} \int_{-L_u/L}^{L_d/L} u_b^2 \;\; d(x/L). \quad (6.12)$$

Combining (6.12) with (6.11) gives

$$p_{-l/2} - p_{l/2} = \frac{1}{2}\rho U^2 \left(\beta_4^2 - \alpha_4^2\right) + \rho S \frac{L}{w} \int_{-L_u/L}^{L_d/L} \left(u_b^2 - u_c^2\right) \;\; d(x/L) \; . \quad (6.13)$$

Finally, writing a streamwise momentum balance for the channel extending between $x = -L_u$ and $x = L_d$ leads to

$$\frac{wh_0}{B}(p_{-L_u} - p_{L_d}) - T - F_b - F_c \quad (6.14)$$

$$= \rho U^2 \alpha_2 w h_0 \left(\alpha_4 - 1\right) + \rho U^2 \left(\frac{1}{B} - \alpha_2\right) w h_0 \left(\beta_4 - 1\right) \; ,$$

where T is the total retarding force component due to the obstacle and F_b and F_c are force components associated with seabed friction in the bypass flow and core flow, respectively, and are given by

$$F_b = \rho C_f L \int_{-L_u/L}^{L_d/L} w_b u_b^2 \, d(x/L) \quad \text{and} \quad F_c = \rho C_f L \int_{-L_u/L}^{L_d/L} w_c u_c^2 \, d\,(x/L) \ , \quad (6.15)$$

and β_4 is obtained from (6.9), and w_b and w_c are the width of the by-pass flow and core flow, respectively, given by (6.7) and (6.5). The right hand side of (6.14) represents the difference in momentum in the core and bypass flows respectively, calculated using the values obtained for u_c, u_b, w_c and w_b in Section 6.2.1. In (6.14) it is assumed that the change in water elevation upstream and downstream of the obstacle is small so that the difference in hydrostatic pressure integrated across the channel cross section at $x = -L_u$ and $x = L_d$ is given approximately as $wh_0(p_{-L_U} - p_{L_d})/B$. The change in water elevation will be small provided that the Froude number is small (see Garrett and Cummins, 2007).

Noting that the thrust $T = (p_{-l/2} - p_{l/2})wh_0$, it therefore follows that (6.15) can be combined with (6.10) and (6.14) to give

$$\beta_4^2 \,(1 - B) - \beta_4 \,(2 - 2\alpha_4) + \left(1 - 2\alpha_4 + \alpha_4^2 B\right) + S\frac{L}{w}X = 0 \ , \quad (6.16)$$

with

$$X = 2\int_{-L_u/L}^{L_d/L} \left(\frac{u_b}{U}\right)^2 d(x/L) \quad (6.17)$$

$$- 2B \int_{-\frac{L_u}{L}}^{\frac{L_d}{L}} \left\{ \left(\frac{u_b}{U}\right)^2 - \left(\frac{u_c}{U}\right)^2 + \frac{w_b}{w}\left(\frac{u_b}{U}\right)^2 + \frac{w_c}{w}\left(\frac{u_c}{U}\right)^2 \right\} d\left(\frac{x}{L}\right) \ .$$

To complete the analysis it is also possible to write, from (6.23) and (6.13), that

$$\frac{T}{\frac{1}{2}\rho U^2 w h_0} = k_p \alpha_2^2 = \left(\beta_4^2 - \alpha_4^2\right) + 2S\frac{L}{w}\int_{-L_u/L}^{L_d/L} \frac{(u_b^2 - u_c^2)}{U^2} d(x/L) \ , \tag{6.18}$$

where k_p represents a local drag coefficient which, as noted previously, may be interpreted as the dimensionless resistance of the obstacle. Equations (6.10), (6.16) and (6.18) now provide the relationships that link the obstacle resistance to the core flow velocity. For example, by selecting values for S, B, L_u and L_d for a given scenario, it is possible to choose a wake velocity coefficient α_4 and simultaneously solve (6.16) for β_4, and either (6.10) or (6.14) for α_2 numerically. The resistance k_p corresponding to the chosen α_4 can then be determined from (6.18). Since k_p varies monotonically with $1/\alpha_4$, a numerical solution for the core flow velocity, which may be written functionally as: $\alpha_2(k_p, B, S, L_u, L_d)$, can therefore be obtained numerically by repeating this process for a range of α_4 . The solution can be obtained numerically and gives an identical result to that obtained by Garrett and Cummins (2007) in the limit $S = 0$. Alternatively, when $S > 0$ the only practical difficulty in using the model is that the length scales L_u and L_d must be quantified. Accurate evaluation of these length scales is difficult because, although scaling arguments may be useful in some scenarios (i.e. Rominger and Nepf, 2011, use scaling arguments to show that $L_u \sim O(w)$ regardless of k_p when $B \approx 0$), in general L_u and L_d may vary with blockage ratio and additional parameters such as stability number S. To explore this dependency, numerical simulations are employed in the following sections.

6.3 Numerical Simulations

6.3.1 Shallow Water Model

The depth-averaged continuity and momentum equations are used to model the flow through the channel in Figure 6.1. Sediment transport and bed morphology are neglected, the depth-averaged density of the fluid is constant, and an additional shear stress is added to account for the presence of the porous obstacle.

The governing equations (2.14a), (2.14b), and (2.14c) simplify to give

$$\frac{\partial h}{\partial t} + \nabla \cdot (h\boldsymbol{u}) = 0, \tag{6.19}$$

$$\rho \frac{\partial h\boldsymbol{u}}{\partial t} + \rho \left(\boldsymbol{u} \cdot \nabla\right) h\boldsymbol{u} = -\rho g h \nabla h - \rho \left(C_f + C_p\right) \boldsymbol{u} \left|\boldsymbol{u}\right| \ , \tag{6.20}$$

where $\boldsymbol{u} = (u, v)$ represents the depth-averaged velocity velocity in horizontal Cartesian coordinates (x, y), t is time, g is the acceleration due to gravity, ρ is the density of the fluid, h is water depth, C_f parametrises natural bed resistance throughout the channel, and C_p parametrises the (additional) equivalent shear stress τ_p due to the porous obstacle (and is non-zero only within the obstacle); so that,

$$\tau_p = \rho C_p u \left|u\right| \ . \tag{6.21}$$

Depending on the application, (6.21) may be rewritten in terms of the drag coefficients, dimensions and solid volume fraction of constituent structures within the obstacle. For an array of emergent circular cylinders, the depth-averaged force per unit plan area may be defined as (Rominger and Nepf, 2011)

$$\tau_p = \frac{N_c \left(\frac{1}{2}\rho c_D \left(d_c h_0\right) u \left|u\right|\right)}{1 - \phi} \ , \tag{6.22}$$

where c_D is the local drag coefficient of an individual cylinder, d_c is the cylinder diameter, N_c is the number of cylinders per unit plan area of the obstacle and $\phi = \pi N_c d_c^2/4$ is the solid volume fraction of cylinders within the obstacle (i.e. the geometric porosity is equal to $1 - \phi$). It should be noted that (6.22) is only an approximation of the total force if c_D is chosen based on data for isolated cylinders. A more accurate estimate would include an effective c_D accounting for interference effects between cylinders.

Alternatively, for an array of tidal stream turbines the net force per unit width perpendicular to the flow is usually expressed in terms of the resistance k_p (Draper and Nishino, 2014); *i.e.*

$$F = \tau_p l = \frac{1}{2}\rho k_p h_0 u \left|u\right| \tag{6.23}$$

Equating forces therefore gives

$$k_p = \frac{2C_p l}{h_0} = \frac{c_D a_c l}{1-\phi} = \frac{4c_D \phi l}{\pi d_c (1-\phi)} \ . \tag{6.24}$$

where $a_c = N_c d_c$ is the frontal area of cylinders per unit volume (Rominger and Nepf, 2011). Hence k_p may be used to represent the resistance of an array of turbines or an array of cylindrical structures. Herein, results are presented in terms of k_p. However, conversion between parameters is straightforward using (6.24). To simplify the problem it is useful to introduce non-dimensional variables $h' = h/h_0$, $x' = x/w$, $u' = u/U$ and $t' = tU/w$. Equations (6.19) and (6.20) then become

$$\frac{\partial h'}{\partial t'} + \nabla \cdot \left(h' \boldsymbol{u}'\right) = 0 \ , \tag{6.25}$$

$$\frac{\partial h' \boldsymbol{u}'}{\partial t'} + \left(\boldsymbol{u}' \cdot \nabla\right) h' \boldsymbol{u}' = -\frac{1}{Fr^2} h' \nabla h' - \left(S + \frac{1}{2} k_p A_R\right) \boldsymbol{u}' |\boldsymbol{u}'| \ , \tag{6.26}$$

where $Fr = U/\sqrt{g h_0}$ is the Froude number of the upstream uniform flow, and, as defined previously, $S = C_f w/h_0$ is the stability number and $A_R = w/l$ is the aspect ratio of the obstacle. Scaling the geometry in Figure 6.1 introduces an additional non-dimensional parameter: $B = w/W$. Hence, together with the obstacle resistance k_p, a total of five parameters enter the problem. This set can be reduced to three if it is assumed that (i) Fr is small, so that variations in water depth are everywhere small (i.e. $\nabla h'$ is small), and (ii) the aspect ratio

is of secondary importance for a compact obstacle (which is shown to be the case in the following section). Consequently, the dimensionless velocity field and the length scales L_u and L_d will depend only on the obstacle resistance k_p, the stability number S, and the channel blockage ratio B.

6.3.2 Numerical Solution

Equations (6.25) and (6.26) are solved numerically using the numerical model described in Chapter 3. Free slip solid wall, reflective boundary conditions are applied at the channel side walls, whilst at the upstream boundary the discharge is prescribed and the water depth is extrapolated from cells inside the domain. The water depth is fixed at the downstream boundary and the discharge is free to vary by extrapolation. Domain boundaries are located $6w$ upstream and $25w$ downstream of the obstacle to ensure that upstream flow divergence and downstream wake formation are not influenced by the boundaries. The obstacle is inserted into the channel at $t = 0$ and the numerical model is run until the local flow field close to the obstacle is approximately steady. For low values of stability number this local flow field is not exactly steady, due to the development of vortices in the far downstream wake flow field. The formation of these vortices is qualitatively similar to that for a bluff body with base bleed (Wood, 1964), but only results in small fluctuations (approximately 1-2%) affecting the velocity of the core flow passing through the obstacle.

A uniform grid of square elements is used in the simulations. The time step is chosen to give a maximum Courant-Friedrichs-Lewy number of 0.9. Grid convergence tests indicate that with this time step changes in bulk flow velocity are generally less than 1% when the number of grid cells is doubled from 32 to 64 across the width of the obstacle. A mesh with 32 cells/w is therefore used throughout. Numerical simulations are conducted over the finite parameter space $S \times B = (0, 0.09, 0.5, 1.0, 1.5) \times (0.05, 0.1, 0.25, 0.32, 0.5)$, which is a representative range for aquatic vegetation, offshore structures, and tidal turbine arrays. For each combination of S and B within this space, a minimum of 4 to 6 different k_p values are investigated, ranging from $k_p = 1$ to $k_p = 12 - 60$, depending on stability number and blockage ratio. This range is adequate to identify the maximum

	$A_R = 1$	$A_R = 2$	$A_R = 4$	$A_R = 8$	$A_R = 16$	$A_R = 32$
$S = 0$	0.538	0.532	0.526	0.525	0.523	0.522
$S = 0.2$	0.553	0.546	0.537	0.531	0.530	0.528
$S = 0.5$	0.618	0.599	0.585	0.577	0.573	0.573
$S = 1.2$	0.730	0.694	0.671	0.659	0.652	0.649

Table 6.1: Core flow velocity parameter α_2 (defined in (6.27)) for $B = 0.5$, $k_p = 12$.

power dissipated by the obstacle for tidal turbine applications. It also provides a range in obstacle resistance values typical of aquatic vegetation such as kelp forests or mangrove forests, the latter which can be very dense and have large associated k values (see for example Jackson, 1997; Mazda *et al.*, 1997). In all simulations $Fr = 0.05$, a sufficiently small value that the flow was insensitive to any further reduction in Fr.

Preliminary simulations have also considered different obstacle aspect ratios (Table 6.1). However, when k_p is fixed, the influence of this ratio on the core flow velocity is found to be negligible at low stability number, whilst at larger stability number ($S > 0.5$) the core flow velocity is only sensitive to aspect ratio if the aspect ratio is small ($A_R < 2$). This lack of sensitivity to aspect ratio, for sufficiently compact obstacles, implies that the flow does not 'feel 'the length of a compact obstacle, and so cannot differentiate between the different aspect ratios modelled. Instead, the flow is resisted only by the net force applied by the obstacle, which is described entirely by k_p irrespective of obstacle length. This result verifies the assumption made in Section 6.2, equation (6.11), that the region within the obstacle can be included in the integral without affecting the overall result, provided that $A_R > 1$. For convenience, a value of $A_R = 4$ is adopted throughout the remaining numerical simulations in this chapter so that the results are representative of a compact obstacle (i.e. with $A_R > 1$) over the range of k_p, S and B values investigated.

6.3.3 Numerical Results

Figure 6.2 presents the computed depth-averaged velocity field for two example blockage ratios ($B = 0.05$ and 0.5) and three example stability numbers ($S = 0, 0.5$ and 1.5) when the obstacle has a fixed resistance of $k_p = 12$. For comparison, the figures also show the two streamlines which bound the fluid passing through the centre of the obstacle. It can be seen that these streamlines diverge upstream of the obstacle, as the core flow velocity reduces. Downstream of the obstacle the streamlines then continue to diverge. For $S > 0$, the quadratic background friction preferentially slows the faster bypassing flow so that both the bypass and wake flow speeds recover to those of the upstream flow, and the streamlines begin to converge.

Across the different scenarios in Figure 6.2 it can be seen that the streamlines which bound the flow through the obstacle diverge by a greater amount as they pass through the obstacle when both the blockage ratio and stability number are small; indicating that the flow more easily diverts around the obstacle for the low stability number and blockage ratio leading to a larger reduction in core flow velocity. This result is also evident in Figure 6.3, which presents normalised core flow velocity along $y/w = 0$. It can be seen in these figures that the core flow velocity begins to reduce over some adjustment length upstream of the obstacle, and then reduces monotonically through the obstacle (with a reduction that is well approximated by the simple cubic spline functions used in Section 6.2.1). For sufficiently large stability number the core flow begins to increase at some distance beyond the near wake of the obstacle. Interestingly, Figure 6.4 indicates that the profile of normalised core flow velocity along the channel is mostly affected by the stability number and blockage ratio. In contrast only very minor differences are evident across the range in resistance k_p that have been investigated.

When developing the theoretical model in Section 6.2, two important assumptions were made regarding the flow field. Firstly, it was assumed that the core and bypass flows are uniform. Secondly it was assumed that the core and bypass flow velocities vary smoothly and monotonically along the channel. From Figure 6.2, it can be seen that at the higher blockage ratio (i.e. $B = 0.5$) and low stability number (i.e. $S < 0.5$), the velocity contours show that the increase in velocity

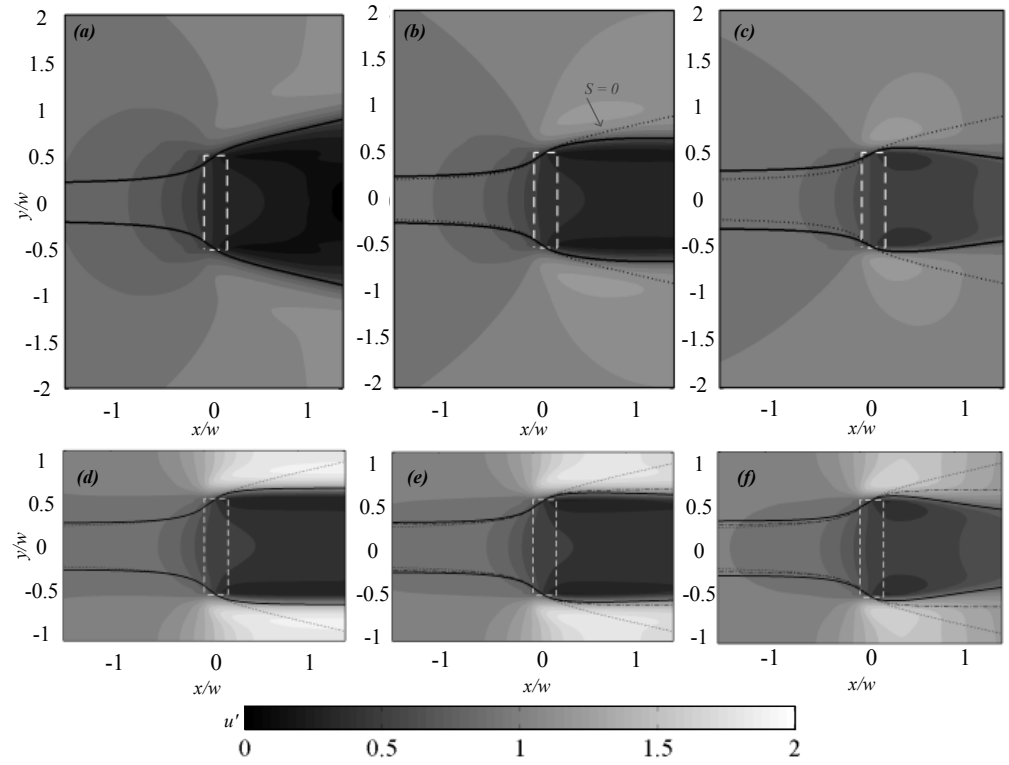

Figure 6.2: Contours of $u^{'}$ for (a) $S = 0, B = 0.05$; (b) $S = 0.09, B = 0.05$; (c) $S = 0.5, B = 0.05$; (d) $S = 0, B = 0.5$; (e) $S = 0.09, B = 0.5$ and (f) $S = 0.5, B = 0.5$. Solid lines indicate streamlines bounding flow through the centre of the obstacle, dash-dot lines indicate the corresponding streamlines for $S = 0$ and the same blockage ratio, and dotted lines indicate the streamlines for $S = 0, B = 0.05$. Dashed line represents the obstacle outline. $A_R = 4, k_p = 12$.

is close to uniform across the bypass flow, which is in good agreement with the model. However, for the lower blockage ratio (and especially for larger stability number) the increase in bypass velocity becomes more confined to a region close to the obstacle; hence the bypass flow becomes increasingly two-dimensional as the blockage ratio reduces and the stability number increases. Consequently the theoretical model assumptions become more approximate in the limits of large blockage ratio and small stability number. Secondly, it can be observed that the core velocity reduces gradually upstream and continues to decrease within, and immediately downstream of, the obstacle, validating the second assumption.

To compare the theoretical model with the numerical simulations more directly, and to enable estimates of the length scales L_u and L_d, it is useful to

quantify the core flow velocity passing through the obstacle in the simulations as

$$u_l = \alpha_2 U = \frac{1}{w}\int_{-w/2}^{w/2} u(0,y)\mathrm{d}y \tag{6.27}$$

where the centre of the obstacle is assumed to be at $(x, y) = (0, 0)$. Having evaluated the core flow velocity coefficient α_2 for the numerical simulations in this way, it is possible for each simulation (with a given k_p, B and S) to tune the length scales in the theoretical model to match the velocity coefficient. To simplify this tuning process it has been assumed that $L_u = L_d$; this represents a pragmatic assumption (and ultimately leads via equation (6.28) to an empirical result for these length scales that may be used to provide robust estimates of the core flow velocity for different input values of k_p, S and B).

Figure 6.4 presents some example fits to the numerical simulations for various combinations of blockage ratio, stability and resistance. Each line in this figure represents the theoretical model result with one fitted length scale $L = 2L_u = 2L_d$. From these results it can be seen that a single length scale is sufficient across a range of obstacle resistance for a given blockage ratio and stability number; *i.e.* $L = f(B, S)$. This is a convenient result which, in physical terms, indicates that the length over which the flow field diverges around the obstacle is less sensitive to k_p than to S or B, as might be anticipated (at least for low blockage ratio) from scale analysis presented by Rominger and Nepf (2011) for the upstream adjustment length.

To explore the functional form of L, the fitted length scales for all combinations of blockage ratio and stability number simulated numerically are presented in Figure 6.5. Several comments can be made concerning the trends in these results. Firstly, for small values of S it can be seen that the fitted length scale increases as the blockage ratio reduces. This trend is consistent with the expectation that increased blockage tends to inhibit the divergence of streamlines, and therefore reduces the length over which flow divergence occurs. Furthermore for small blockage and small S the length scale is on the order of the obstacle width (i.e. $L \sim O(1)$) which is not inconsistent with the scale analysis of Rominger

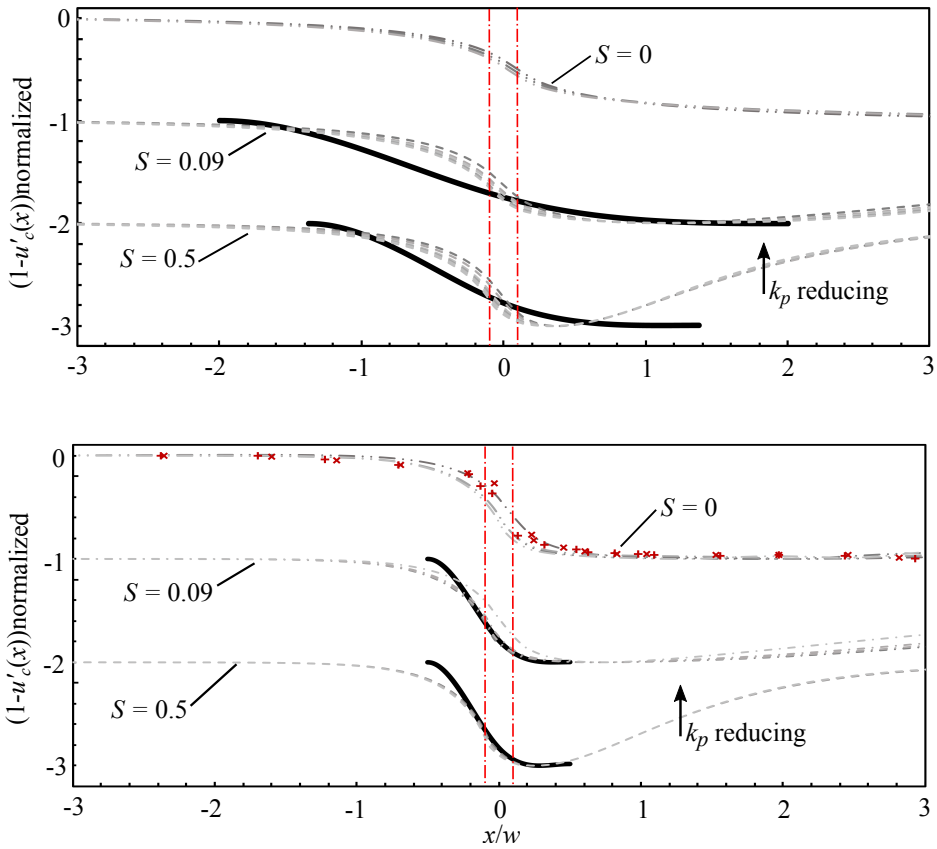

Figure 6.3: Normalised core flow velocity, $(1 - u_c^{'}(x))/(\min(u_c^{'}(x)) - 1)$, profiles from the numerical simulations (dashed, dashed-dot lines) for a range of k_p values at $S = 0, 0.09$ and 0.5; (a) $B = 0.05, k_p = 1 - 35$ and (b) $B = 0.5, k_p = 2 - 32$. Also included in *(b)* are normalised core flow profiles for $S \approx 0, B = 0.35, k_p \approx 4$, digitised from the laboratory-based data of Zong and Nepf (2011, red +) and Chen et al. (2011, red x). The velocity is normalised against the minimum wake velocity for each scenario. Solid black lines are obtained using the theoretical model presented in Section 6.2 combined with (6.28). Red dashed-dot lines indicate upstream and downstream faces of the obstacle. For each increasing S value, the profiles have been displaced vertically by -1.

and Nepf (2011). Secondly, for larger values of S it can be seen that the fitted length scale still increases as the blockage ratio reduces, but for a given blockage the length scale reduces as S increases. This implies that increased background friction reduces the length over which the flow diverges around the obstacle by an amount similar to the reduction in fitted length scale. However, it should be noted that as the stability number increases the bypass flow becomes more two-dimensional in this limit (see figure 6.3). Additionally, the theoretical model fails to account for that fact that the background friction acts to mix the bypass and core flow in the wake of the obstacle, altering the pressure in the wake. Because of these effects, when S is large the fitted length scales are no longer expected to

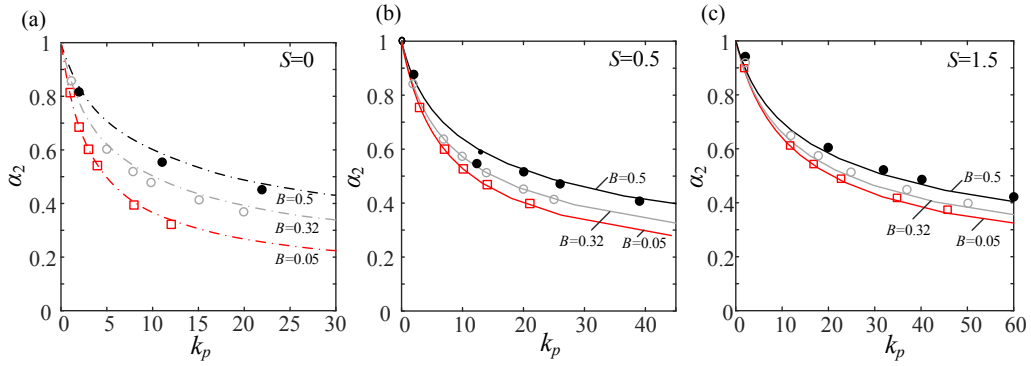

Figure 6.4: Variation in core flow velocity as a function of obstacle resistance k_p. (a) $S = 0$; (b) $S = 0.5$; (c) $S = 1.5$. Numerical results for $B = 0.05$ (squares); $B = 0.32$ (open circles) and $B = 0.5$ (solid circles). Solid lines are predictions using the theoretical model introduced in Section 6.2. Dashed lines are predictions that are equivalent to those obtained using the model of Garrett and Cummins (2007).

be directly related to the physical length over which flow divergence occurs.

To quantify the trends in figure 6.5 the following empirical relationship has been fitted for the length scale:

$$L^{'} = 2L_u^{'} = 2L_d^{'} = f_1 e^{f_2 B}, \tag{6.28}$$

$$\left.\begin{aligned} \text{where,} \quad & f_1(S) = 1.4S^2 - 3.9S + 4.9 \\ \text{and,} \quad & f_2(S) = -0.46S^2 + 1.8S - 3.2\ . \end{aligned}\right\} \tag{6.29}$$

Equation (6.28) may be used directly with the theoretical model developed in Section 6.2 to predict the core flow velocity for any value of stability number and blockage ratio within the parameter space covered in this paper (i.e. for $0.05 \leq B \leq 0.5,\ 0.09 \leq S \leq 1.5$). We also remark that whilst the result in (6.28) is empirical it has the important property that for small stability number the length scale remains finite for all blockage ratios. This is physically meaningful since the main assumptions of the theoretical model (i.e. uniform, smoothly-varying core and bypass flow) are consistent with the numerical solution for small stability number, and so the fitted length scale is expected to resemble the actual

(finite) length over which flow diversion occurs upstream and downstream of the obstacle.

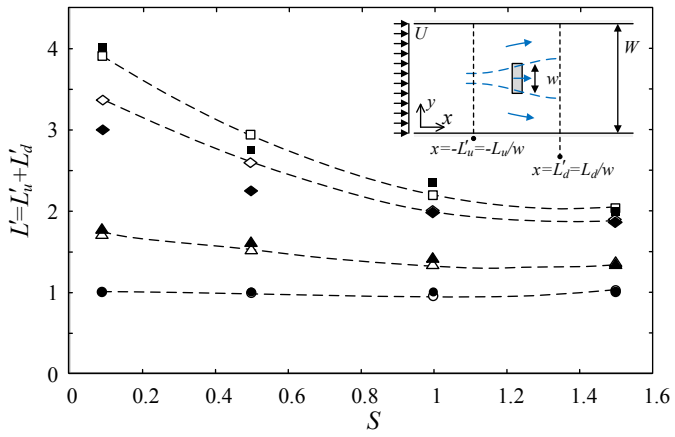

Figure 6.5: Variation in fitted length scale as a function of stability number and channel blockage ratio; $B = 0.5$ (circles), $B = 0.32$ (triangles), $B = 0.1$ (diamonds) and $B = 0.05$ (squares). Lengths calculated using (4.10) for $B = 0.5$ (open circles), $B = 0.32$ (open triangles), $B = 0.1$ (open diamonds) and $B = 0.05$ (open squares).

In the following section the numerical model is used to provide new insight into two example problems that may be modelled according to the simplified problem geometry in Figure 6.1.

6.4 Example Applications

6.4.1 Prediction of Core Flow Velocity through an Array of Emergent Cylinders

Ball *et al.* (1996), Zong and Nepf (2011) and Chen *et al.* (2012) carried out laboratory experiments to analyse the bulk flow characteristics and wake structure associated with a compact porous obstacle represented as an array of emergent circular rigid cylinders. Apart from the work of Ball *et al.*, the motivation of this work was to better understand shallow water flows through aquatic vegetation, and the influence of flow diversion and wake dynamics on sediment and nutrient transport, bed morphology and water quality. Collectively, these studies explored a range of obstacle porosities (achieved by changing the number and spacing of cylinders), as well as a range of obstacle widths (so as to give blockage ratios

spanning between 0.05 and 0.35) and different obstacle shapes (circle, square or rectangle). There were also slight variations in the stability parameter between the experiments but S was generally below 0.04.

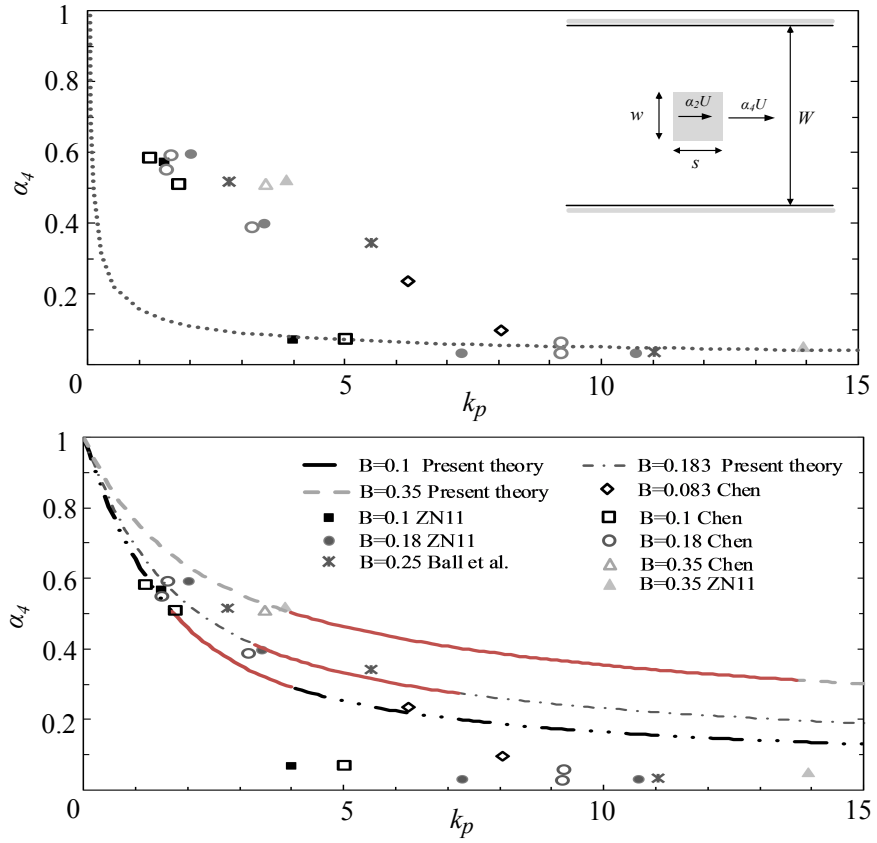

Figure 6.6: Variation of α_4 with k_p for the experiments of Zong and Nepf (2011): $B = 0.1$ solid squares, $B = 0.18$ solid circles, $B = 0.35$ solid triangles, Chen *et al.* (2012): $B = 0.083$ open diamonds, $B = 0.1$ open squares, $B \approx 0.18$ open circles, $B = 0.35$ open triangles, and Ball *et al.* (1996): $B = 0.25$, black stars, with; (a) theoretical model adopted by Zong and Nepf (2011): dotted line, $S = 0.019$, $A_R = 1$; and (b) present theoretical model ($S = 0.015$; $B = 0.1$ dashed double dot, $B = 0.18$ dashed dot, $B = 0.35$ dashed). Solid red lines indicate the range in which the experimental results begin to deviate from the theoretical model.

Figure 6.6 presents experimental measurements reported by Zong and Nepf (2011), Chen *et al.* (2012), and Ball *et al.* (1996) for the normalised velocity in the near wake of the obstacle (defined herein as α_4) as a function of obstacle resistance. In this figure, the obstacle resistance k_p has been computed using (6.24), which requires an estimate for the pile drag coefficient c_D. Zong and Nepf (2011) and Ball *et al.* (1996) assumed $c_D = 1$ for simplicity, whilst Chen *et al.* (2012) estimated c_D for each pile arrangement by assuming that the local drag is proportional to the solid volume fraction ϕ of the array (Tanino and Nepf, 2008).

All of the experimental results plotted in Figure 6.6 are for configurations where $\phi < 0.15$. Within this range, Chen *et al.* calculated $1 < c_D <\sim 2$. For simplicity, the average value, $c_D = 1.5$ has been chosen herein to estimate k_p for all of the experimental values shown in Figure 6.6. For example, in one experiment of Zong and Nepf (2011), $l = D = 22$ cm, $\phi = 0.1, d_c = 0.64$ cm. Letting $c_D = 1.5$, (6.24) yields $k_p = 7.29$.

Figure 6.6 (a) shows the predictive formula adopted by Zong and Nepf (2011). This predictive formula, which is based on scaling arguments given in Rominger and Nepf (2011), assumes that the flow is able to adjust to the obstacle over its length, in which case the velocity is set by a momentum balance between the pressure gradient and the obstacle resistance at the downstream end of the obstacle. To contrast with the predictive formula of Rominger and Nepf (2011), Figure 6.6 (b) shows the same laboratory data as Figure 6.6 but includes predictions based on the theoretical model presented in Section 6.2 (with $S = 0.015$; the mean value of the laboratory-based studies). Focusing initially on the experimental measurements, it can be seen in Figure 6.6 (a) that there is a general reduction in magnitude of the near wake velocity as the obstacle resistance increases. At large resistance (i.e. $k_p >\sim 4 - 14$, depending on channel blockage), this reduction appears to be captured properly by the predictive formula used by Zong and Nepf (2011). However, for low porosity it should be noted that it is difficult to determine a representative near wake velocity (see Figure 4b in Zong and Nepf, 2011, for example), and this introduces some uncertainty into the comparison between Zong and Nepfs prediction and the experimental results in Figure 6.6 for $k_p > 4$. In contrast, for lower resistance (i.e. more porous obstacles $k_p < 4 - 14$) the Zong and Nepf (2011) model gives a poorer prediction with the measurements, whilst the present theoretical model provides good agreement with the measurements, seen in Figure 6.6 (b). In particular, much of the scatter in the laboratory data at lower resistance appears to be explained, according to the present theoretical model, by the blockage ratio used in the experiments. Moreover, the normalised core flow velocity profiles from numerical simulations are in excellent agreement with the experimental results for very porous obstacles, seen in Figure 6.3b. In terms of predicting the flow through porous obstacles, the

present theoretical model therefore appears to complement the model adopted by Zong and Nepf (2011), with the present model providing better predictions for very porous obstacles. The maximum resistance (or minimum porosity) at which the obstacle transitions from being very porous (such that wake velocity no longer agrees with the present theoretical model) appears to be a function of blockage ratio. For instance, as indicated in Figure 6.6 (b), the maximum resistance is between $k_p = 2 - 4$ for $B = 0.1$, $k_p = 3.5 - 8$ for $B = 0.18$ and $k_p = 4 - 14$ for $B = 0.35$. This suggests that the channel blockage ratio may be an important parameter both in controlling the core flow velocity through a very porous obstacle and in determining the limiting resistance at which the obstacle starts to behave as a low porosity obstacle.

The exact reason why the present theoretical model begins to over predict the near wake velocity as the resistance of the obstacle becomes larger cannot be directly explained from the experimental results given in Figure 6.6. However, it is relevant to note from Figure 6.4 that the present model gives predictions in agreement with numerical simulations of the shallow water equations up to resistance values exceeding the threshold k_p values indicated above. Consequently, the maximum obstacle resistance at which the theoretical model starts to over-predict the measurements in Figure 6.6(b) coincides with the maximum resistance for which the depth-averaged shallow water simulations over-predict the measurements. In this sense, the results in Figure 6.6 therefore highlight a limitation in the shallow water equations for modelling the wake behind an obstacle with low porosity. This is consistent with previously identified limitations of the shallow water equations to reproduce the wake behind a porous obstacle and the velocity profile through the obstacle in shallow water (Ball *et al.*, 1996). In their study, Ball *et al.* modified the drag coefficient of the obstacle in order to obtain agreement with the experimental results. As the spacing between the cylinders reduced, i.e. as k_p increased, the ratio between the experimental and numerical drag coefficients increased. For example, for an experimental $k_p = 2.76$, the numerical model requires $c_D = 1.9$, but for $k_p = 11$, $c_D = 5.6$ is required. Ball *et al.* attributed this to the lack of horizontal diffusion in the shallow water model. The results presented in Figure 6.6 confirm that a simple shallow water model

and the theoretical model derived herein can be used to simulate accurately the hydrodynamics through and around a porous obstacle, provided it is sufficiently porous.

6.4.2 Optimum Arrangements of Turbines in a Channel

It is also possible to use the new theoretical model to explore quantitatively how natural seabed resistance may affect the optimum local spacing of tidal stream turbines in a channel. To do this one can follow the approach mapped out by Nishino and Willden (2012), who introduced an idea of scale separation to model a fence of turbines partially blocking a wide channel (see Figure 6.7). Nishino and Willden's approach was to model individual turbines within the fence as individual compact obstacles using the same theory as in Section 6.2 (but with $S = 0$) so as to compute the flow through each turbine as a function of a local geometric blockage B_l and resistance k_l (i.e. to obtain the local velocity coefficients $\alpha_{2,l}(B_l, k_l)$). At this turbine scale the local blockage B_l was set equal to $A_t/(s_t + d_c)h_0$, in which A_t is the swept area of the turbine, d_c is the turbine diameter, and s_t is the spacing between adjacent turbines. The power extracted by each turbine was then computed as

$$P_l = \alpha_{2,l} U_l T = \frac{1}{2} \rho k_l \alpha_{2,l}^3 A_t U_l^3 \ . \tag{6.30}$$

where U_l is the local upstream velocity.

To account for the fact that the collection of turbines also acts like a porous obstacle, Nishino and Willden (2012) also modelled the fence of turbines as an obstacle. At this array scale the array blockage B_a was calculated as the ratio of fence area $A_f = N_t(s_t + d_c)h_0$ where N_t is the total number of turbines, to the cross-sectional area of the tidal channel. The array scale resistance was chosen to ensure the total force at array scale was equal to N_t times the force at local scale (i.e. the array and turbine scales were coupled by matching the force). This was achieved by setting the local resistance equal to $k_a = \alpha_{2,l}^2 k_l B_l$. The solution for the bulk flow velocity at this array scale was then used to calculate the local

velocity, which is equal to $U_l = \alpha_{2,a}U$. Consequently, the total power removed from the channel was calculated according to

$$P = N_t \left(\alpha_{2,l} U_l T\right) = \frac{1}{2}\rho N_t k_l \alpha_{2,l}^3 A_t (\alpha_{2,a}U)^3 \ . \tag{6.31}$$

Using this approach Nishino and Willden (2012) found that for a given array blockage, there was always an optimum local blockage B_L (i.e. an optimum arrangement of turbines) to maximise power. Furthermore, they showed that this optimum result agreed reasonably well with 3D numerical simulations of long fences of porous obstacles emulating turbines (Nishino and Willden, 2013). Despite obtaining reasonable agreement with 3D numerical simulations, a limi-

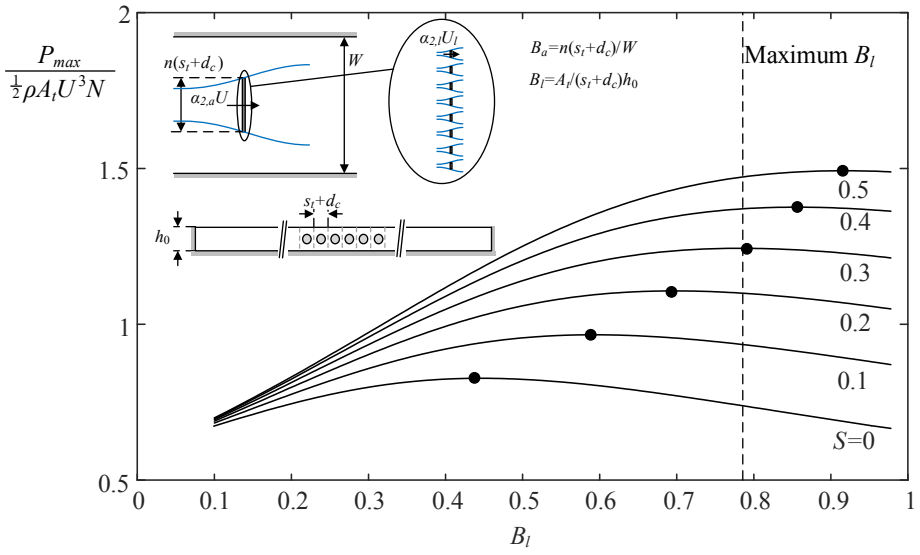

Figure 6.7: Maximum power as a function of local blockage for a fence of turbines having a total length equal to 5 % of the channel width (i.e. $B_a = 0.05$). Vertical dashed line indicates the maximum local blockage ratio for circular turbines. Dots indicate the optimum local blockage ratio; i.e. the optimum local spacing/arrangement of turbines within the fence for a given stability number.

tation of the Nishino and Willden (2012) analysis was that the tidal channel was assumed to be frictionless. In reality, however, a fence of turbines could span over a width $w \sim O(10^3)$ m. Thus, taking $C_f \sim O(10^{-3})$ and $h_0 \sim O(10^1)$ m, it follows that at the array scale $S \sim O(10^{-1})$ and so frictional effects may not be negligible. Motivated by this result, the theoretical model developed in Section 6.2

is used in this section to update the model presented by Nishino and Willden (2012). This is achieved by using the theoretical model presented in Section 6.2 to model the fence at array scale, whilst maintaining the frictionless solution at local scale (where frictional forces are likely to be less important relative to the force provided by the turbines, i.e. the local length scale is expected to be a small fraction of the array length scale). To provide an example solution, $B_a = 0.05$ is assumed. This represents a very wide channel, in which the net resistance of the tidal turbines is unlikely to have a back effect on the net flow through the channel (Vennell, 2010).

Results are presented in Figure 6.7 for maximum power, as a function of B_l, for different values of stability number. It can be seen that there is a substantial increase in power generation as S increases. For example, regardless of local blockage ratio, there is an increase in maximum extractable power compared to the frictionless result. This increase occurs simply because background friction acts to resist the faster moving bypass flow and force more flow through the fence. Consequently turbines can provide greater resistance and remove more power before a significant fraction of the flow starts to bypass the fence. Figure 6.7 also shows that the optimum local blockage increases with stability number; indicating that it is advantageous to place turbines closer together in frictional tidal channels. This increase is such that for $S >\sim 0.3$ the optimum blockage exceeds $\pi/4 \sim 0.78$, which is the largest local blockage for circular turbines in a rectangular channel. In such instances, the model indicates that the turbines should be placed as close as practically possible to generate more power. In terms of the validity of these estimates it should be noted that for optimum power extraction and optimum turbine arrangement (indicated by the dots in Figure 6.7) the resistance of the array is $k_a = 1.0$ and $k_l = 4.9$ when $S = 0$. Given that $B_a = 0.05$ and $B_l = 0.44$, these resistances appear to be within the very porous range identified in Section 6.4.1 for similar blockage ratios; thus validating the use of the underlying theoretical models. For larger values of S the results in Section 6.4.1 cannot be used to infer whether the turbines still represent very porous obstacles. It would be insightful to investigate if this is the case in future work.

6.5 Chapter Summary

A theoretical model has been developed to predict the core flow velocity passing through a compact porous obstacle in a shallow channel which extends the model of Garrett and Cummins (2007) to include natural bed resistance. The model has application for predicting flow through emergent aquatic vegetation, the performance of arrays of stream turbines in tidal channels and the net forces on offshore structures. The new model is particularly relevant when combined effects of stability number S, channel blockage B and obstacle resistance k_p are important.

Direct application of the theoretical model to arrays of emergent cylinders emulating a patch of aquatic vegetation has indicated that the model provides satisfactory predictions of core flow velocity over the range for which the shallow water equations are valid. Within this range (i.e. for very porous obstacles) the present model indicates that channel blockage ratio has a noticeable effect on the core flow velocity, even at small values of blockage ratio.

The theoretical model proposed herein has also been used to confirm that, for a given flow velocity, the existence of natural bed resistance (i.e. $S > 0$) enables greater power extraction from turbines arranged in a partial fence within a very wide channel. Natural bed resistance has been shown to influence the optimum arrangement of turbines in the fence in this case. For $S >\sim 0.3$, the model indicates that turbines placed in a fence should be spaced as close together as is practically possible for maximum power extraction. For $S \leq\sim 0.3$, there is an optimum spacing between turbines to remove maximum power.

Through comparison of the proposed theoretical model with experimental data it was found that there exists a minimum porosity, which is a function of B, below which the present theoretical model and the shallow water approximation of flow through a porous obstacle become invalid.

References

M.B. Abbott. *Computational Hydraulics*. Ashgate Publishing Co., Brookfield, 1979.

M.B. Abbott and D.R. Basco. *Computational fluid dynamics*. Longman Scientific & Technical Harlow, Essex, 1989.

F. Alcrudo and P. García-Navarro. A high-resolution Godunov-type scheme in finite volumes for the 2D shallow-water equations. *International Journal for Numerical Methods in Fluids*, 16(6):489–505, 1993.

I.G. Apostolidou. *Variable density shallow flow model for flood simulaton*. PhD thesis, University of Oxford, 2011.

T. Asano. Sediment transport under sheet-flow conditions. *Journal of Waterway, Port, Coastal, and Ocean Engineering*, 121(5):239–246, 1995.

R.A. Bagnold. The flow of cohesionless grains in fluids. *Philosophical Transactions of the Royal Society of London A: Mathematical, Physical and Engineering Sciences*, 249(964):235–297, 1956.

D.J. Ball, N. Alliston, and P.K. Stansby. Modelling shallow water flow around pile groups. *Proceedings of the ICE - Water Maritime and Energy*, 118(4): 226–236, 1996.

N.J. Balmforth and A. Vakil. Cyclic steps and roll waves in shallow water flow over an erodible bed. *Journal of Fluid Mechanics*, 695:35–62, 2012.

F. Benkhaldoun, I. Elmahi, and M. Seaïd. Well-balanced finite volume schemes for pollutant transport by shallow water equations on unstructured meshes. *Journal of Computational Physics*, 226(1):180–203, 2007.

F. Benkhaldoun, I. Elmahi, S. Sari, and M. Seaïd. An unstructured finite-volume method for coupled models of suspended sediment and bed load transport in shallow-water flows. *International Journal for Numerical Methods in Fluids*, 72(9):967–993, 2013.

A. Bermúdez and M.E. Vázquez. Upwind methods for hyperbolic conservation laws with source terms. *Computers and Fluids*, 23(8):1049–1071, 1994.

G. Berz. Climatic change: Effects on and possible responses by the insurance industry. *Climate of the 21st Century: Changes and Risks. Wissenschaftliche Auswertungen, Hamburg*, pages 392–399, 2001.

G. Boole. *A treatise on the calculus of finite differences*. MacMillan, London, 1860. Fourth Edition, Chelsea Publishing Company, New York, 1958.

R. Briganti, N. Dodd, D. Kelly, and D. Pokrajac. An efficient and flexible solver for the simulation of the morphodynamics of fast evolving flows on coarse sediment beaches. *International Journal for Numerical Methods in Fluids*, 69 (4):859–877, 2012.

P. Brufau, M.E. Vázquez-Cendón, and P. García-Navarro. A numerical model for the flooding and drying of irregular domains. *International Journal for Numerical Methods in Fluids*, 39(3):247–275, 2002.

R. Canelas, J. Murillo, and R.M.L. Ferreira. Two-dimensional depth-averaged modelling of dam-break flows over mobile beds. *Journal of Hydraulic Research*, 51(4):392–407, 2013.

Z. Cao. Equilibrium near-bed concentration of suspended sediment. *Journal of Hydraulic Engineering*, 125(12):1270–1278, 1999.

Z. Cao and P.A. Carling. Mathematical modelling of alluvial rivers: reality and myth. Part 1: General review. *Proceedings of the ICE - Water and Maritime Engineering*, 154(3):207–219, 2002a.

Z. Cao and P.A. Carling. Mathematical modelling of alluvial rivers: reality and myth. Part 2: Special issues. *Proceedings of the ICE - Water and Maritime Engineering*, 154(4):297–307, 2002b.

Z. Cao, G. Pender, S. Wallis, and P. Carling. Computational dam-break hydraulics over erodible sediment bed. *Journal of Hydraulic Engineering*, 130(7): 689–703, 2004.

Z. Cao, G. Pender, and P. Carling. Shallow water hydrodynamic models for hyperconcentrated sediment-laden floods over erodible bed. *Advances in Water Resources*, 29(4):546–557, 2006.

Z. Cao, P. Hu, and G. Pender. Reconciled bedload sediment transport rates in ephemeral and perennial rivers. *Earth Surface Processes and Landforms*, 35 (14):1655–1665, 2010.

Z. Cao, P. Hu, and G. Pender. Multiple time scales of fluvial processes with bed load sediment and implications for mathematical modeling. *Journal of Hydraulic Engineering*, 137(3):267–276, 2011.

Z. Cao, Z. Li, G. Pender, and P. Hu. Non-capacity or capacity model for fluvial sediment transport. *Proceedings of the ICE-Water Management*, 165(4):193–211, 2012.

H. Capart and D.L. Young. Formation of a jump by the dam-break wave over a granular bed. *Journal of Fluid Mechanics*, 372:165–187, 1998.

M.J. Castro Díaz, E.D. Fernández-Nieto, and A.M. Ferreiro. Sediment transport models in shallow water equations and numerical approach by high order finite volume methods. *Computers and Fluids*, 37(3):299–316, 2008.

M.J. Castro Díaz, E.D. Fernández-Nieto, A.M. Ferreiro, and C. Parés. Two-dimensional sediment transport models in shallow water equations. A second order finite volume approach on unstructured meshes. *Computer Methods in Applied Mechanics and Engineering*, 198(33):2520–2538, 2009.

J.G. Charney, R. Fjörtoft, and J. von Neumann. Numerical Integration of the Barotropic Vorticity Equation. *Tellus A*, 2(4):238–254, 1950.

D. Chen and G.H. Jirka. Experimental study of plane turbulent wakes in a shallow water layer. *Fluid Dynamics Research*, 16(1):11–41, 1995.

Z. Chen, A. Ortiz, L. Zong, and H. Nepf. The wake structure behind a porous obstruction and its implications for deposition near a finite patch of emergent vegetation. *Water Resources Research*, 48(9), 2012.

M.J. Creed, S. Draper, T. Nishino, and A.G.L. Borthwick. Flow through a very porous obstacle in a shallow channel. *Proceedings of the Royal Society of London A: Mathematical, Physical and Engineering Sciences*, 473(2200), 2017a.

M. Creed, I.G. Apostolidou, P. Taylor, and A. Borthwick. A finite volume shock-capturing solver of the fully coupled shallow water-sediment equations. *International Journal for Numerical Methods in Fluids*, 2017b.

H. Cui, J.D. Pietrzak, and G.S. Stelling. A finite volume analogue of the finite element: With accurate flooding and drying. *Ocean Modelling*, 35(1-2):16–30, 2010.

H.J. de Vriend. 2DH mathematical modelling of morphological evolutions in shallow water. *Coastal Engineering*, 11(1):1–27, 1987.

M. De Vries. River-bed variations - aggradation and degradation. *I.H.A.R. International Seminar on Hydraulics of Alluvial Streams, New Dehli*, 1973.

S. Draper and T. Nishino. Centred and staggered arrangements of tidal turbines. *Journal of Fluid Mechanics*, 739:72–93, 2014.

A. Dundes. *The flood myth*. University of California Press, 1988.

H.A. Einstein. *The bed-load function for sediment transportation in open channel flows*. Number 1026. US Department of Agriculture, 1950.

R. Falconer. An introduction to nearly horizontal flows. In *Coastal Estuarial and Harbour Engineers*, pages 27–36. E and FN Spon Ltd, London, 1993.

R.J. Fennema and M.H. Chaudhry. Explicit methods for 2-D transient free surface flows. *Journal of Hydraulic Engineering*, 116(8):1013–1034, 1990.

G. Fourtakas, B.D. Rogers, and D.R. Laurence. Modelling sediment resuspension in industrial tanks using SPH. *La Houille Blanche*, (2):39–45, 2013.

L. Fraccarollo, H. Capart, and Y. Zech. A Godunov method for the computation of erosional shallow water transients. *International Journal for Numerical Methods in Fluids*, 41(9):951–976, 2003.

L. Fraccarollo and H. Capart. Riemann wave description of erosional dam-break flows. *Journal of Fluid Mechanics*, 461:183–228, 2002.

L. Fraccarollo and E.F. Toro. Experimental and numerical assessment of the shallow water model for two-dimensional dam-break type problems. *Journal of Hydraulic Research*, 33(6):843–864, 1995.

P. Frey and M. Church. Bedload: a granular phenomenon. *Earth Surface Processes and Landforms*, 36(1):58–69, 2011.

M. Fujihara and A.G.L. Borthwick. Godunov-type solution of curvilinear shallow-water equations. *Journal of Hydraulic Engineering*, 126(11):827–836, 2000.

M. Garcia and G. Parker. Entrainment of bed sediment into suspension. *Journal of Hydraulic Engineering*, 117(4):414–435, 1991.

P. García-Navarro, F. Alcrudo, and J. Savirón. 1-D open-channel flow simulation using TVD-McCormack scheme. *Journal of Hydraulic Engineering*, 118(10): 1359–1372, 1992.

C. Garrett and P. Cummins. The efficiency of a turbine in a tidal channel. *Journal of Fluid Mechanics*, 588:243–251, 2007.

C. Garrett and P.F. Cummins. Maximum power from a turbine farm in shallow water. *Journal of Fluid Mechanics*, 714:634–643, 2013.

S.K. Godunov. A difference method for numerical calculation of discontinuous solutions of the equations of hydrodynamics. *Matematicheskii Sbornik*, 89(3): 271–306, 1959.

N. Goutal and F. Maurel. *Proceedings of the 2nd workshop on dam-break wave simulation*. Electricité de France. Direction des études et recherches, 1997.

W.L. Graf. Geomorphology and American dams: The scientific, social, and economic context. *Geomorphology*, 71(1-2):3–26, 2005.

W.L. Graf. Downstream hydrologic and geomorphic effects of large dams on American rivers. *Geomorphology*, 79(3):336–360, 2006.

A.J. Grass. *Sediment transport by waves and currents*. University College London, Dept. of Civil Engineering, 1981.

A. Harten, P.D. Lax, and B. van Leer. On upstream differencing and Godunov-type schemes for hyperbolic conservation laws. *SIAM review*, 25(1):35–61, 1983.

M.J.T. Heywood and D.E. Walling. The sedimentation of salmonid spawning gravels in the Hampshire Avon catchment, UK: implications for the dissolved oxygen content of intragravel water and embryo survival. *Hydrological Processes*, 21(6):770–788, 2007.

G.T. Houlsby, S. Draper, and M.L.G. Oldfield. Application of Linear Momentum Actuator Disc Theory to Open Channel Flow by. pages 1–23, 2008.

J. Huang, A.G.L. Borthwick, and R.L. Soulsby. Adaptive quadtree simulation of sediment transport. *Proceedings of the ICE - Engineering and Computational Mechanics*, 163(2):101–110, 2010.

J. Huang, A.G.L. Borthwick, and R.L. Soulsby. One-dimensional modelling of fluvial bed morphodynamics. *Journal of Hydraulic Research*, 46(5):636–647, 2008.

J. Hudson and P.K. Sweby. Formulations for Numerically Approximating Hyperbolic Systems Governing Sediment Transport. *Journal of Scientific Computing*, 19(1-3):225–252, 2003.

J. Hudson and P.K. Sweby. A high-resolution scheme for the equations governing 2D bed-load sediment transport. *International Journal for Numerical Methods in Fluids*, 47(10-11):1085–1091, 2005.

G.A. Jackson. Currents in the high drag environment of a coastal kelp stand off California. *Continental Shelf Research*, 17(15):1913–1928, 1997.

T. Jacobsen and R.M. Adams. Salt and silt in ancient Mesopotamian agriculture. *Science*, 128(3334):1251–1258, 1958.

L. Jiang, A.G.L. Borthwick, T. Krámer, and J. Józsa. Variable density bore interaction with block obstacles. *International Journal of Computational Fluid Dynamics*, 25(4):223–237, 2011.

H.K. Johnson and J.A. Zyserman. Controlling spatial oscillations in bed level update schemes. *Coastal Engineering*, 46(2):109–126, 2002.

C. Juez, J. Murillo, and P. García-Navarro. A 2D weakly-coupled and efficient numerical model for transient shallow flow and movable bed. *Advances in Water Resources*, 71:93–109, 2014.

C. Juez, J. Murillo, and P. García-Navarro. One-dimensional riemann solver involving variable horizontal density to compute unsteady sediment transport. *Journal of Hydraulic Engineering*, 142(3):4015056, 2015.

P.Y. Julien. *Erosion and sedimentation*. Cambridge University Press, 2010.

G.M. Kondolf, Y. Gao, G.W. Annandale, G.L. Morris, E. Jiang, J. Zhang, Y. Cao, P. Carling, K. Fu, Q. Guo, *et al.* Sustainable sediment management in reservoirs and regulated rivers: experiences from five continents. *Earth's Future*, 2(5): 256–280, 2014.

S. Kostic, O. Sequeiros, B. Spinewine, and G. Parker. Cyclic steps: A phenomenon of supercritical shallow flow from the high mountains to the bottom of the ocean. *Journal of Hydro-environment Research*, 3(4):167–172, 2010.

W. Lai and A.A. Khan. A discontinuous Galerkin method for two-dimensional shallow water flows. *International Journal for Numerical Methods in Fluids*, 70(8):939–960, 2012.

F.Z. Leighton, A.G.L. Borthwick, and P.H. Taylor. 1-D numerical modelling of shallow flows with variable horizontal density. *International Journal for Numerical Methods in Fluids*, 62(11):1209–1231, 2010.

G.R. Lesser, J.A. Roelvink, J.A.T.M. van Kester, and G.S. Stelling. Development and validation of a three-dimensional morphological model. *Coastal Engineering*, 51(8-9):883–915, 2004.

J. Li, Z. Cao, G. Pender, and Q. Liu. A double layer-averaged model for dam-break flows over mobile bed. *Journal of Hydraulic Research*, 51(5):518–534, 2013a.

W. Li, H.J. Vriend, Z. Wang, and D.S. Maren. Morphological modeling using a fully coupled, total variation diminishing upwind-biased centered scheme. *Water Resources Research*, 49(6):3547–3565, 2013b.

D. Liang, R.A. Falconer, and B. Lin. Comparison between TVD-MacCormack and ADI-type solvers of the shallow water equations. *Advances in Water Resources*, 29(12):1833–1845, 2006.

Q. Liang and A.G.L. Borthwick. Adaptive quadtree simulation of shallow flows with wet-dry fronts over complex topography. *Computers and Fluids*, 38(2): 221–234, 2009.

Q. Liang, A.G.L. Borthwick, and G. Stelling. Simulation of dam- and dyke-break hydrodynamics on dynamically adaptive quadtree grids. *International Journal for Numerical Methods in Fluids*, 46(2):127–162, 2004.

T.E. Lisle. Sediment transport and resulting deposition in spawning gravels, north coastal california. *Water Resources Research*, 25(6):1303–1319, 1989.

Y. Liu, J. Zhou, L. Song, Q. Zou, L. Liao, and Y. Wang. Numerical modelling of free-surface shallow flows over irregular topography with complex geometry. *Applied Mathematical Modelling*, 37(23):9482–9498, 2013.

T.J. Logan. Diffuse (non-point) source loading of chemicals to Lake Erie. *Journal of Great Lakes Research*, 13(4):649–658, 1987.

S. Maldonado-Villanueva. *Quasi-2-Layer morphodynamic model and lagrangian study of bedload.* PhD thesis, The University of Edinburgh, Edinburgh, U.K., 2015.

M. Marta-Almeida, R. Mendes, F.N. Amorim, M. Cirano, and J.M. Dias. Fundão Dam collapse: Oceanic dispersion of River Doce after the greatest Brazilian environmental accident. *Marine Pollution Bulletin*, 2016.

W.M. Mayes, A.P. Jarvis, I.T. Burke, M. Walton, V. Feigl, O. Klebercz, and K. Gruiz. Dispersal and attenuation of trace contaminants downstream of the Ajka bauxite residue (red mud) depository failure, Hungary. *Environmental Science and Technology*, 45(12):5147–5155, 2011.

Y. Mazda, E. Wolanski, B. King, A. Sase, D. Ohtsuka, and M. Magi. Drag force due to vegetation in mangrove swamps. *Mangroves and Salt Marshes*, 1: 193–199, 1997.

E. McCurdy *et al. The notebooks of Leonardo da Vinci*. Garden City Publishing Co., inc., 1941.

D.M. McDowell and B.A. O'Connor. *Hydraulic behavior of estuaries*. Wiley, 1977.

E. Meyer-Peter and R. Müller. Formulas for bed-load transport. IAHR, 1948.

C. Miao, J. Ni, and A.G.L. Borthwick. Recent changes of water discharge and sediment load in the Yellow River basin, China. *Progress in Physical Geography*, 34(4):541–561, 2010.

C. Miao, J. Ni, A.G.L. Borthwick, and L. Yang. A preliminary estimate of human and natural contributions to the changes in water discharge and sediment load in the Yellow River. *Global and Planetary Change*, 76(3):196–205, 2011.

J.D. Milliman and R.H. Meade. World-wide delivery of river sediment to the oceans. *The Journal of Geology*, pages 1–21, 1983.

C.G. Mingham and D.M. Causon. High-resolution finite-volume method for shallow water flows. *Journal of Hydraulic Engineering*, 124(6):605–614, 1998.

J. Murillo and P. García-Navarro. Energy balance numerical schemes for shallow water equations with discontinuous topography. *Journal of Computational Physics*, 236:119–142, 2013.

J. Murillo, B. Latorre, and P. García-Navarro. A Riemann solver for unsteady computation of 2D shallow flows with variable density. *Journal of Computational Physics*, 231(14):4775–4807, 2012.

J. Murillo and P. García-Navarro. An Exner-based coupled model for two-dimensional transient flow over erodible bed. *Journal of Computational Physics*, 229(23):8704–8732, 2010.

J. Ni, Y. Yue, A.G.L. Borthwick, T. Li, C. Miao, and X. He. Erosion-induced CO2 flux of small watersheds. *Global and Planetary Change*, 94:101–110, 2012.

J. Ni, G. Wang, and A. Borthwick. Kinetic theory for particles in dilute and dense solid-liquid flows. *Journal of Hydraulic Engineering*, 126(12):893–903, 2000.

A. Nicolle and I. Eames. Numerical study of flow through and around a circular array of cylinders. *Journal of Fluid Mechanics*, 679:1–31, 2011.

Y. Niño and M. García. Using Lagrangian particle saltation observations for bed-load sediment transport modelling. *Hydrological Processes*, 12(8):1197–1218, 1998.

T. Nishino and R.H.J. Willden. The efficiency of an array of tidal turbines partially blocking a wide channel. *Journal of Fluid Mechanics*, 708:596–606, 2012.

T. Nishino and R.H.J. Willden. Two-scale dynamics of flow past a partial cross-stream array of tidal turbines. *Journal of Fluid Mechanics*, 730:220–244, 2013.

S. Osher and F. Solomon. Upwind difference schemes for hyperbolic systems of conservation laws. *Mathematics of Computation*, 38(158):339–374, 1982.

I.K. Othman, T.E. Baldock, and D.P. Callaghan. Measurement and modelling of the influence of grain size and pressure gradient on swash uprush sediment transport. *Coastal Engineering*, 83:1–14, 2014.

P.N. Owens. Sediment behaviour, functions and management in river basins. *Sustainable Management of Sediment Resources*, 4:1–29, 2008.

G. Parker and N. Izumi. Purely erosional cyclic and solitary steps created by flow over a cohesive bed. *Journal of Fluid Mechanics*, 419:203–238, 2000.

A.J. Raudkivi. *Loose boundary hydraulics*. CRC Press, 1998.

J.F. Richardson and W.N. Zaki. The sedimentation of a suspension of uniform spheres under conditions of viscous flow. *Chemical Engineering Science*, 3(2): 65–73, 1954.

L.F. Richardson. On the approximate arithmetical solution by finite differences of physical problems involving differential equations, with an application to the stresses in a masonry dam. *Proceedings of the Royal Society of London A: Mathematical, Physical and Engineering Sciences*, 83(563):335–336, 1910.

P.L. Roe. Approximate riemann solvers, parameter vectors, and difference schemes. *Journal of Computational Physics*, 43(2):357–372, 1981.

B.D. Rogers, M. Fujihara, and A.G.L. Borthwick. Adaptive Q-tree Godunov-type scheme for shallow water equations. *International Journal for Numerical Methods in Fluids*, 35(3):247–280, 2001.

B.D. Rogers, A.G.L. Borthwick, and P.H. Taylor. Mathematical balancing of flux gradient and source terms prior to using Roe's approximate Riemann solver. *Journal of Computational Physics*, 192(2):422–451, 2003.

J.T. Rominger and H.M. Nepf. Flow adjustment and interior flow associated with a rectangular porous obstruction. *Journal of Fluid Mechanics*, 680:636–659, 2011.

W. Silva, J.P. Dijkman, and D.P. Loucks. Flood management options for the netherlands. *International Journal of River Basin Management*, 2(2):101–112, 2004.

H. Sinclair, S. Mudd, T. LeDivellec, K. Dallas, and H. Andy. Geomorphic flux from Himalayan flashflood fquates to 1000 yrs average erosion rate. In *EGU General Assembly Conference Abstracts*, April 2016.

S. Soares-Frazão, J. Lhomme, V. Guinot, and Y. Zech. Two-dimensional shallow-water model with porosity for urban flood modelling. *Journal of Hydraulic Research*, 46:45–64, 2008.

S. Soares-Frazão, R. Canelas, Z. Cao, L. Cea, H.M. Chaudhry, A. Die Moran, K. El Kadi, R. Ferreira, I.F. Cadórniga, N. Gonzalez-Ramirez, *et al.* Dam-break flows over mobile beds: experiments and benchmark tests for numerical models. *Journal of Hydraulic Research*, 50(4):364–375, 2012.

R. Soulsby. *Dynamics of marine sands: a manual for practical applications*. Thomas Telford, 1997.

B. Spinewine and H. Capart. Intense bed-load due to a sudden dam-break. *Journal of Fluid Mechanics*, 731:579–614, 2013.

P.K. Stansby. Limitations of depth-averaged modeling for shallow wakes. *Journal of Hydraulic Engineering*, 132(7):737–740, 2006.

P.K. Stansby. A mixing-length model for shallow turbulent wakes. *Journal of Fluid Mechanics*, 495:369–384, 2003.

G.S. Stelling and S.P.A. Duinmeijer. A staggered conservative scheme for every Froude number in rapidly varied shallow water flows. *International Journal for Numerical Methods in Fluids*, 43(12):1329–1354, 2003.

J. Sun, B. Lin, and H. Yang. Development and application of a braided river model with non-uniform sediment transport. *Advances in Water Resources*, 81:62–74, 2015.

T. Sun and G. Parker. Transportational cyclic steps created by flow over an erodible bed. Part 2. Theory and numerical simulation. *Journal of Hydraulic Research*, 43(5):502–514, 2005.

C. Swartenbroekx, S. Soares-Frazão, R. Staquet, and Y. Zech. Two-dimensional operator for bank failures induced by water-level rise in dam-break flows. *Journal of Hydraulic Research*, 48(3):302–314, 2010.

C. Swartenbroekx, Y. Zech, and S. Soares-Frazão. Two-dimensional two-layer shallow water model for dam break flows with significant bed load transport. *International Journal for Numerical Methods in Fluids*, 73(5):477–508, 2013.

P.K. Sweby. High resolution schemes using flux limiters for hyperbolic conservation laws. *SIAM journal on numerical analysis*, 21(5):995–1011, 1984.

J.P. Syvitski, C.J. Vörösmarty, A.J. Kettner, and P. Green. Impact of humans on the flux of terrestrial sediment to the global coastal ocean. *Science*, 308(5720): 376–380, 2005.

T. Takemura and N. Tanaka. Flow structures and drag characteristics of a colony-type emergent roughness model mounted on a flat plate in uniform flow. *Fluid Dynamics Research*, 39(9-10):694–710, 2007.

Y. Tanino and H.M. Nepf. Laboratory investigation of mean drag in a random array of rigid, emergent cylinders. *Journal of Hydraulic Engineering*, 134(1): 34–41, 2008.

E.F. Toro. Riemann problems and the WAF method for the two-dimensional shallow water equations. *Philosophical Transactions of the Royal Society A: Mathematical, Physical and Engineering Sciences*, 338(1):43–68, 1992.

E.F. Toro, M. Spruce, and W. Speares. Restoration of the contact surface in the HLL Riemann solver. *Shock Waves*, 4:25–34, 1994a.

E.F. Toro, M. Spruce, and W. Speares. Restoration of the contact surface in the Harten-Lax-van Leer Riemann solver. *Shock Waves*, 4:25–34, 1994b.

E.F. Toro. *Riemann solvers and numerical methods for fluid dynamics*. Springer-Verlag, 1999.

E.F. Toro. *Shock-capturing methods for free-surface shallow flows*. Wiley, 2001.

B. van Leer. On the relation between the upwind-differencing schemes of Godunov, Engquist-Osher and Roe. *SIAM Journal on Scientific and Statistical Computing*, 5(1):1–20, 1985.

F.F. van Ogtrop, A.Y. Hoekstra, and F. van der Meulen. Flood management in the Lower Incomati river basin, Mozambique: two alternatives. *Journal of the American Water Resources Association*, 41:607–619, 2005.

L.C. Van Rijn. Sediment transport, part I: bed load transport. *Journal of Hydraulic Engineering*, 110(10):1431–1456, 1984a.

L.C. Van Rijn. Sediment transport, part II: suspended load transport. *Journal of Hydraulic Engineering*, 110(11):1613–1641, 1984b.

R. Vennell. Tuning turbines in a tidal channel. *Journal of Fluid Mechanics*, 663: 253–267, 2010.

J. Viers, B. Dupré, and J. Gaillardet. Chemical composition of suspended sediments in World Rivers: New insights from a new database. *Science of the Total Environment*, 407(2):853–868, 2009.

G. Wang, B. Wu, and Z.Y. Wang, Wang. Sedimentation problems and management strategies of Sanmenxia Reservoir, Yellow River, China. *Water Resources Research*, 41(9):1–17, 2005a.

Z.Y. Wang and C. Hu. Strategies for managing reservoir sedimentation. *International Journal of Sediment Research*, 24(4):369 – 384, 2009.

Z.Y. Wang, J.H. Lee, and D. Cheng. Impacts of the TGP project on the Yangtze River ecology and management strategies. *International Journal of River Basin Management*, 3(4):237–246, 2005b.

A. Wesselink, J. Warner, M.A. Syed, F. Chan, D.D. Tran, H. Huq, F. Huthoff, N. Le Thuy, N. Pinter, M. Van Staveren, *et al.* Trends in flood risk management in deltas around the world: Are we going 'soft '? *International Journal of Water Governance*, 3(4):25–46, 2015.

M. Wong and G. Parker. Reanalysis and correction of bed-load relation of meyer-peter and müller using their own database. *Journal of Hydraulic Engineering*, 132(11):1159–1168, 2006.

Q. Wu, Z. Zhao, L. Liu, D.E. Granger, H. Wang, D.J. Cohen, X. Wu, M. Ye, O. Bar-Yosef, B. Lu, *et al.* Outburst flood at 1920 BCE supports historicity of China's Great Flood and the Xia dynasty. *Science*, 353(6299):579–582, 2016.

J. Xia, B. Lin, R.A. Falconer, and G. Wang. Modelling dam-break flows over mobile beds using a 2D coupled approach. *Advances in Water Resources*, 33 (2):171–183, 2010.

K. Xu and J.D. Milliman. Seasonal variations of sediment discharge from the Yangtze River before and after impoundment of the Three Gorges Dam. *Geomorphology*, 104(3):276–283, 2009.

K. Yan. *Coastal flood inundation and morphodynamic change*. PhD thesis, University of Oxford, 2010.

Z. Yang, H. Wang, Y. Saito, J.D. Milliman, K. Xu, S. Qiao, and G. Shi. Dam impacts on the Changjiang (Yangtze) River sediment discharge to the sea: The past 55 years and after the Three Gorges Dam. *Water Resources Research*, 42 (4), 2006.

Y. Yi, Z.Y. Wang, and Z. Yang. Impact of the Gezhouba and Three Gorges Dams on habitat suitability of carps in the Yangtze River. *Journal of Hydrology*, 387 (3):283–291, 2010.

X. Ying and S.S. Wang. Improved implementation of the HLL approximate Riemann solver for one-dimensional open channel flows. *Journal of Hydraulic Research*, 46(1):21–34, 2008.

Y. Yue, J. Ni, A.G.L. Borthwick, and C. Miao. Diagnosis of river basins as CO2 sources or sinks subject to sediment movement. *Earth Surface Processes and Landforms*, 37(13):1398–1406, 2012.

R. Zhang and J. Xie. *Sedimentation research in China: Systematic selections*. China and Power Press, 1993.

J.G. Zhou, D.M. Causon, C.G. Mingham, and D.M. Ingram. The surface gradient method for the treatment of source terms in the shallow-water equations. *Journal of Computational Physics*, 168:1–25, 2001.

J.G. Zhou, D.M. Causon, D.M. Ingram, and C.G. Mingham. Numerical solutions of the shallow water equations with discontinuous bed topography. *International Journal for Numerical Methods in Fluids*, 38(8):769–788, 2002.

J.G. Zhou. Lattice Boltzmann morphodynamic model. *Journal of Computational Physics*, 270:255–264, 2014.

L. Zong and H. Nepf. Vortex development behind a finite porous obstruction in a channel. *Journal of Fluid Mechanics*, 691:368–391, 2011.

Zurich Insurance. Risk Nexus: Urgent case for recovery: what we can learn from the August 2014 Karnali River floods in Nepal. 2015.